Solid oxide membrane reactors: catalyst development and testing for solid oxide fuel cells and oxidative coupling of methane

by

Brittany Lancaster Farrell

A dissertation submitted in partial fulfillment
of the requirements for the degree of
Doctor of Philosophy
(Chemical Engineering)
in the University of Michigan
2016

Doctoral Committee:

Professor Suljo Linic, Chair
Professor Mark A. Barteau
Adjunct Professor Galen B. Fisher
Professor John W. Halloran

2016

This dissertation is dedicated to my family, for all of their love and support throughout the entire process

Acknowledgements

I would like to begin this dissertation by acknowledging many people without whom this work would not have been possible. First I would like to thank my thesis advisor, Professor Suljo Linic, who encouraged me to pursue a research topic that was new to both me and to the lab, and who gave me a lot of freedom to choose the direction of my experimental research. Over the five years of my PhD, his mentorship helped me develop my skills, particularly in areas of scientific writing and oral presentations. I would also like to thank my committee members, Professor Mark Barteau, Adjunct Professor Galen Fisher, and Professor John Halloran for their advice throughout my studies, and for their careful reading and notes on this dissertation.

I would also like to thank the Department of Chemical Engineering and the wonderful members of the staff that keep everything running smoothly. In particular I would like to thank Harold Eberhart, Shelley Fellers, Kelly Raickovich, Barbara Perry, Susan Hamlin, Connie Bacus, Dana Jackson, and Pam Bogdanski for all of their help throughout the years. I would also like to thank all of the ChEGS officers, past and present for keeping a sense of community alive amongst the graduate students, and Professor Mark Burns for encouraging and funding our endeavors.

I have been very fortunate to work with many amazing students within the Linic group, whose friendship and assistance has been invaluable over the years. Throughout my PhD I worked with the following students who each contributed to our lab family (in no particular order): Paul Hernley, Tim Van Cleve, Adam Holewinski, Michelle Przybylek, Hongliang Xin, Thomas Yeh, Matthew Morabito, Mari Addiappan, Phil Christopher, David Ingram, Thomas Noel, Anh Ta, Calvin Boerigter, Robert Campana, Umar Aslam, Valentina Igenegbai, Saman Moniri, Joe Quinn, and Steven Chavez. I would also like to thank Professor Eranda Nikolla who graduated before I was a part of the group, but has nonetheless provided me with a large amount of assistance and advice during my PhD.

Outside of the department, I would like to thank my wonderful group of friends who really made Ann Arbor seem like home. I am definitely going to miss the football games, holiday parties, and nights out with all of the following people: Allison Franck, Ryan Franck, Youngri Kim, Paul Hernley, Tim Van Cleve, Laura Helmkamp, Laura Chang, George Zhao, Luke Griffith, Jessica Griffith, and Julia Faeth. It's both fun and sad to watch everyone graduate and move on to bigger and better things.

I also owe a huge debt of gratitude to my family, who have always supported me in everything that I have done. In particular I would like to thank my grandparents, Stanley and Evelyn Lancaster for their love and support, and my sister Courtney for setting the bar high, and always challenging me to do better. I also need to thank my parents, Terri and Brent Lancaster, for teaching me all of the important things in life-including how to build and make things, and encouraging my "do it myself" attitude from the very beginning.

Finally, I want to thank my husband Nathan Farrell for all of his love and support throughout our relationship and the PhD process. He uprooted his entire life to move to Ann Arbor with me so that I could go to graduate school, and in that time he has acted as best friend, confidante, shoulder to cry on, sounding board, technical support, practice audience, proof reader, wedding date, and pretty much anything else that I needed. For all of these things, and for believing in me, I will always be grateful.

Table of Contents

Dedication ..... **ii**

Acknowledgements ..... **iii**

List of Figures ..... **x**

List of Tables ..... **xiv**

List of Schemes ..... **xv**

Abstract ..... **xvi**

Chapter 1: Introduction and background **1**

1.1 Summary 1

1.2 Changing energy landscape 2

1.3 Chemical reactions and catalysis 4

1.4 Solid oxide membrane reactors 7

1.5 Solid oxide fuel cells 12

1.6 Oxidative coupling of methane 15

1.7 Scope of the thesis 18

1.8 References 20

Chapter 2: Experimental techniques **24**

2.1 Summary 24

2.2 Catalyst preparation and membrane reactor fabrication 25

2.2.1 Solid oxide fuel cells 25

2.2.2 Oxidative coupling of methane packed bed reactor catalysts 28

2.2.3 Oxidative coupling of methane membrane reactors 29
2.3 Experimental setups 30
2.3.1 Solid oxide fuel cell (SOFC) experiments 30
2.3.2 Oxidative coupling of methane packed bed reactor experiments 32
2.3.3 Oxidative coupling of methane membrane reactor experiments 32
2.4 Electrochemical techniques 32
2.4.1 Current-voltage curves 36
2.4.2 Impedance spectroscopy 38
2.5 Gas chromatography 42
2.6 Reactor models 43
2.7 Ex-situ sample characterization 44
2.7.1 Scanning electron microscopy 44
2.7.2 Energy dispersive spectroscopy 45
2.7.3 X-ray photoelectron spectroscopy 45
2.7.1 X-ray diffraction 46
2.8 References 49

Chapter 3: Direct electrochemical oxidation of ethanol on SOFCs: improved carbon tolerance of Ni anode by alloying 51
3.1 Summary 51
3.2 Introduction 52
3.3 Experimental 55
3.3.1 Electrochemical measurements 55
3.3.2 Catalyst characterization 55
3.3.2.1 Scanning electron microscopy 55
3.3.2.2 X-ray photoelectron spectroscopy 56
3.3.3 Synthesis 56

3.4 Results 59
3.4.1 Electrochemical testing 59
3.4.2 Ex-situ anode characterization 67
3.5 Discussion 71
3.6 Conclusions 75
3.7 References 77

Chapter 4: Oxidative coupling of methane to ethane and ethylene: assessment of membrane reactors for potential increases in yield and selectivity of C_2 products ..81
4.1 Summary 81
4.2 Introduction 82
4.3 Reactor models 89
4.4 Sensitivity analysis 90
4.5 Solid oxide membrane reactors 95
4.6 Conclusions 99
4.7 References 101

Chapter 5: Oxidative coupling of methane over mixed oxide catalysts designed for solid oxide membrane reactors 107
5.1 Summary 107
5.2 Introduction 108
5.3 Experimental methods, results, and discussion 114
5.4 Conclusions 128
5.5 References 130

Chapter 6: Oxidative coupling of methane using oxygen permeable solid oxide membrane reactors with Li-LSGM catalyst 135
6.1 Summary 135
6.2 Introduction 136
6.3 Experimental methods 138
6.3.1 Membrane reactor fabrication 138

6.3.2 Reactor testing 139
6.3.3 X-ray diffraction 140
6.3.4 Scanning electron microscopy 140
6.4 Experimental results and discussion 141
6.4.1 Reactor characterization 141
6.4.1.1 Membranes 141
6.4.1.2 Reactor structure 141
6.4.1.3 Catalyst/Membrane interfaces 142
6.4.2 Reactor testing 146
6.4.3 Activity degradation 150
6.5 Conclusions 154
6.6 References 155

Chapter 7: Conclusions and future outlook 158
7.1 Conclusions 158
7.1.1 Solid oxide fuel cells 158
7.1.2 Oxidative coupling of methane 158
7.2 Future directions 161
7.1.1 Solid oxide fuel cells 161
7.1.2 Oxidative coupling of methane 161
7.3 References 164

List of Figures

Figure

1.1 US energy consumption by sector and primary energy source. Data from the US Energy Information Administration.....**3**

1.2 a) Diagram of a reaction occurring on a catalyst surface b) Reaction coordinate showing activation energy required for reaction with and without a catalyst **6**

1.3 Membrane reactor diagrams: a) Reactor with a membrane that is ionically conductive with an external circuit for electron transport b) Reactor with a membrane with both ionic and electronic conductivity and no external circuit.....**9**

1.4 a) Fluorite structure where A represents metal atoms (e.g. Zr) and X represents oxygen atoms b) Perovskite structure where A and B represent metal atoms (e.g. La and Ga) and X represents oxygen atoms **10**

1.5 Solid oxide fuel cell diagram showing reactions with hydrogen gas to form water **14**

1.6 a) Basic steps of OCM on a metal oxide catalyst surface b) Gibbs Free Energy change for OCM reactions.....**17**

2.1 Solid oxide fuel cell experimental setup.....**33**

2.2 OCM packed bed reactor experimental setup.....**34**

2.3 OCM membrane reactor experimental setup.....**35**

2.4 Current-Polarization curves showing the voltage excitation (red, top axis), the current response (black, bottom axis), and the three polarization regions **37**

2.5 Nyquist Plot **40**

2.6 Equivalent circuit model commonly used for SOFCs with a table of common circuit elements and their calculated impedance **41**

2.7 Diagram of EDS X-Ray generation and collection. 1) An incoming electron strikes an atom. 2) The incoming electron and a core electron from an inner orbital are scattered. 3) An outer orbital electron relaxes to fill the hole. 4) An X-Ray is released and collected by the detector **48**

2.8 Diagram of XPS photoelectron generation and collection **48**

3.1 a) SEM image of the cross-section of the electrolyte of a fuel cell used in this study b) Energy dispersive spectroscopy of the anode structure showing areas of nickel and zirconia b) Diagram of the electrochemical testing setup **58**

3.2 I-V (solid markers) and power density (open markers) curves for fuel cells operated on 30 sccm Ar bubbled through ethanol at 296 K at 1013 K (a) monometallic Ni anode cell: circles are data collected after 10 min of operation on ethanol, triangles are data collected after 18 hr operation on ethanol at 0.6 V (b) 1%Sn/Ni anode cell: circles are data collected after 10 min of operation on ethanol, triangles are data collected after 20 hr operation on ethanol at 0.6 V..... **63**

3.3 I-V (solid markers) and power density (open markers) curves for fuel cells operated on 120 sccm hydrogen at 1013 K (a) Ni cell operated only on hydrogen: circles are data collected after 8 hr at 0.6 V on hydrogen, triangles are data collected after 28 hr at 0.6 V on hydrogen. (b) Ni cell operated on hydrogen: circles are data collected after 6 hr at 0.6 V on hydrogen, triangles are data collected after 18 hr at 0.6 V on ethanol. (c) 1%Sn/Ni cell operated on hydrogen: circles are data collected after 4 hr at 0.6 V on hydrogen, triangles are data collected after 20 hr at 0.6 V on ethanol **64**

3.4 Impedance spectroscopy taken at OCV and 1013 K. (a) Ni cell operated on only hydrogen: circles are data collected after 4 hr at 0.6 V, triangles are data collected after 28 hr at 0.6 V (b) Ni cell operated on ethanol: circles are data collected after 10 min at 0.6 V, triangles are data collected after 18 hr at 0.6 V. (c) 1%Sn/Ni cell operated on ethanol: circles are data collected after 10 min at 0.6 V, triangles are data collected after 20 hr at 0.6 V **65**

3.5 XPS data and curve fitting for a) the Ni 2p edge and b) the Sn 3d edge **68**

3.6 SEM images (top) with EDS maps (bottom) taken 100 μm from the outside of the anode showing Ni (green), Zr (yellow) and C (red) for (a, b) Ni anode fuel cell operated on only H_2 for 28 hr(c, d) Ni anode fuel cell operated on ethanol at 0.6 V for 18 hr (e, f) 1%Sn/Ni anode fuel cell operated on ethanol at 0.6 V for 20 hr ... **72**

3.7 EDS C/Ni peak ratios for fuel cells as a function of distance from the electrolyte. The final measurement for each cell is taken 50 μm from the outer edge of the anode **73**

4.1 Published methane conversion and C_2 selectivity data for metal oxide catalysts (all catalysts are oxides, however oxygen has been omitted in the formulas). Circles indicate that the reaction was performed in a packed bed reactor and diamonds indicate that the reaction was performed in a membrane reactor **86**

4.2 a) The change in Gibbs free energy for the reactions that can occur in an OCM reactor at 1073 K and 1 atm, where C_s is solid graphitic carbon b) Thermodynamic carbon product selectivity for a reactor at 1073 K with minimized Gibbs free energy as a function of the O_2/CH_4 ratio in the feed **87**

4.3 Molar flow rate of each reactant and product within a packed bed plug flow reactor (top) and a membrane plug flow reactor (bottom) **91**

4.4 Sensitivity coefficients for the yield and selectivity of C_2 products for packed bed and membrane plug flow reactors **94**

4.5 Schematic of solid oxide membrane reactors with: a) electronic and ionically conductive membrane and b) ionically conductive membrane with electronically conductive catalysts and external circuit **100**

5.1 Selectivity and yield of C_{2+} products for each catalyst tested at 1023 K with a total inlet flow rate of 100 sccm. Lines are included to guide the eye..... **120**

5.2 Selectivity of CO (diamonds), CO_2 (squares), Ethylene (triangles), Ethane (circles), and C_3 products (x) as a function of methane conversion and CH_4/O_2 ratio for LSGM, 1% Li-LSGM, LSCF, and LSM catalysts. Lines are included to guide the eye **121**

5.3 Effect of temperature on the overall yield of C_{2+} products and on the yields of ethane and ethylene for LSGM and 1% Li-LSGM catalyst operating at O_2:CH_4:Inert (He+N_2) ratio of 1:3:4 and total flow rate of 100 sccm: a) LSGM b) 1% Li-LSGM **122**

5.4 Stability of 1% Li-LSGM catalyst at 1073 K and O_2:CH_4:Inert molar ratio of 1:3:4 at a total of 100 sccm **126**

5.5 X-ray diffraction patterns for LSGM catalysts: a) LSGM as received, b) LSGM after heating to 1073 K in Ar c) LSGM after reaction at 1073 K for 48 hours, d) 1% Li-LSGM after heating to 1073 K in Ar, e) 1% Li-LSGM after reaction at 1073 K for 48 hours **127**

6.1 X-ray diffraction patterns for the sintered membrane disks **143**

6.2 Scanning electron microscopy images for cross-sections of the membrane reactors. a) Ni-LSGM membrane reactor b) LSCF membrane reactor **144**

6.3 Scanning electron microscopy images and energy dispersive spectroscopy maps for membrane/catalyst interfaces. a) LSCF catalyst and LSGM membrane, b) LSCF membrane and 1% Li-LSGM catalyst and c) Ni-LSGM membrane and 1% Li-LSGM catalyst **145**

6.4 Membrane reactor methane conversion and C_{2+} yield and selectivity over time for a) Ni-LSGM membrane reactor, b) LSCF membrane reactor **148**

6.5 Steady state reactor results for LSCF and Ni-LSGM membrane reactors: a) oxygen flux, b) selectivity to C_{2+} products, c) methane conversion, d) C_{2+} yield **149**

6.6 Selectivity of carbon products formed at steady state reaction conditions a) Ni-LSGM membrane reactor, b) LSCF membrane reactor.....**152**

6.7 X-ray diffraction of catalysts supported on membrane disks. a) 1% Li-LSGM catalyst heated in Ar, b) 1% Li-LSGM catalyst after reaction **153**

7.1 C_2 selectivity and methane conversion diagram for results presented in this dissertation (red data points) as well as from several other publications (black data points) References for data points in black are included in Chapter 4. .....**160**

List of Tables

Table

1.1 Factors that affect the oxygen flux in a solid oxide membrane reactor **11**

2.1 Solid oxide fuel cell materials..... **26**

2.2 Oxidative coupling of methane packed bed reactor materials **29**

2.3 Oxidative coupling of methane membrane reactor materials **31**

4.1 OCM Reactor model inputs **89**

4.2 Properties required for an optimal membrane reactor catalyst **98**

5.1 BET surface area and particle size for the catalysts used in this study..... **115**

List of Schemes

Scheme

4.1 OCM reaction network **88**

5.1 OCM reaction network **109**

Abstract

In this dissertation, solid oxide membrane reactors were fabricated and tested as 1) fuel cells operating directly on ethanol and 2) for the production of ethane and ethylene directly from methane. The first part of this dissertation discusses results from a study where solid oxide fuel cells were fabricated with Ni based anodes and operated directly on ethanol fuel. In this study, small amounts of Sn (1wt% on a metals basis) added to the surface of the Ni anode improved the carbon tolerance of the fuel cells. Improved carbon tolerance of the Sn/Ni alloy electrocatalysts led to enhanced electrochemical stability as well as less carbon deposition within the anode as compared to the monometallic Ni samples. The second part of this dissertation presents an analysis of membrane and packed bed plug flow reactors for the process of oxidative coupling of methane (OCM) using kinetic data from the literature. This analysis demonstrated that the use of membrane reactors for OCM can theoretically result in higher yields of ethane and ethylene products compared to packed bed reactors. The final part of the dissertation presents experimental work directed towards the development of membrane reactors for OCM. This work included a catalyst screening which identified lanthanum gallate doped with strontium and magnesium ($La_{0.8}Sr_{0.2}Ga_{0.8}Mg_{0.2}O_{3-x}$, LSGM) as a promising catalyst for use in membrane reactors for OCM. Integration of this catalyst into a membrane reactor showed high selectivity to ethane and ethylene, however, due to low membrane

surface area, the methane conversion was very small and decreased over time, possibly due to carbon poisoning of the catalyst surface.

Chapter 1

Introduction and Background

1.1 Summary

This chapter serves as an introduction to solid oxide membrane reactors, providing information on their basic function and how they can be used to generate power and produce chemical feedstocks. The chapter begins with a brief discussion on the energy landscape within the United States, which serves as the motivation for this study, followed by basic principles of chemical reactions and catalysis and the basic function of membrane reactors. The discussion then focuses on two technologies: solid oxide fuel cells and oxidative coupling of methane. Each technology is described, along with the challenges that limit the overall usefulness of the technology and will be addressed in detail in later chapters. The conclusion of this chapter provides a scope of this thesis with short descriptions of each chapter.

1.2 Changing energy landscape

Over the last several decades energy consumption in the United States has risen from 68 quadrillion BTU in 1970 to 98 quadrillion BTU in 2014 [1]. Energy consumption can be broken down into four main categories which include transportation, industrial, residential and commercial, and electric power. Within each sector there are one or more preferred energy sources, which are mainly fossil fuels (petroleum, natural gas, and coal). Figure 1.1 shows data from 2012 for US energy consumption by energy source and sector.

As illustrated in Figure 1.1, in the transportation sector the largest energy source is petroleum. Over the last few decades there has been a large increase in the available resources in the United States due to advancements in the recovery of shale and tight oil [2]. The availability of large reservoirs of petroleum domestically has resulted in the United States becoming the largest producer of petroleum in the world [2]. Prior to the increased production of petroleum, the recovery of shale gas increased the production of methane rich natural gas (~90% CH_4) which can be extracted on its own or along with petroleum liquids. Although much of the natural gas produced in the United States is burned as fuel or used in chemical synthesis, portions that are not economically recoverable are flared to the atmosphere, releasing CO_2, water, and criteria air pollutants including NO_x [3].

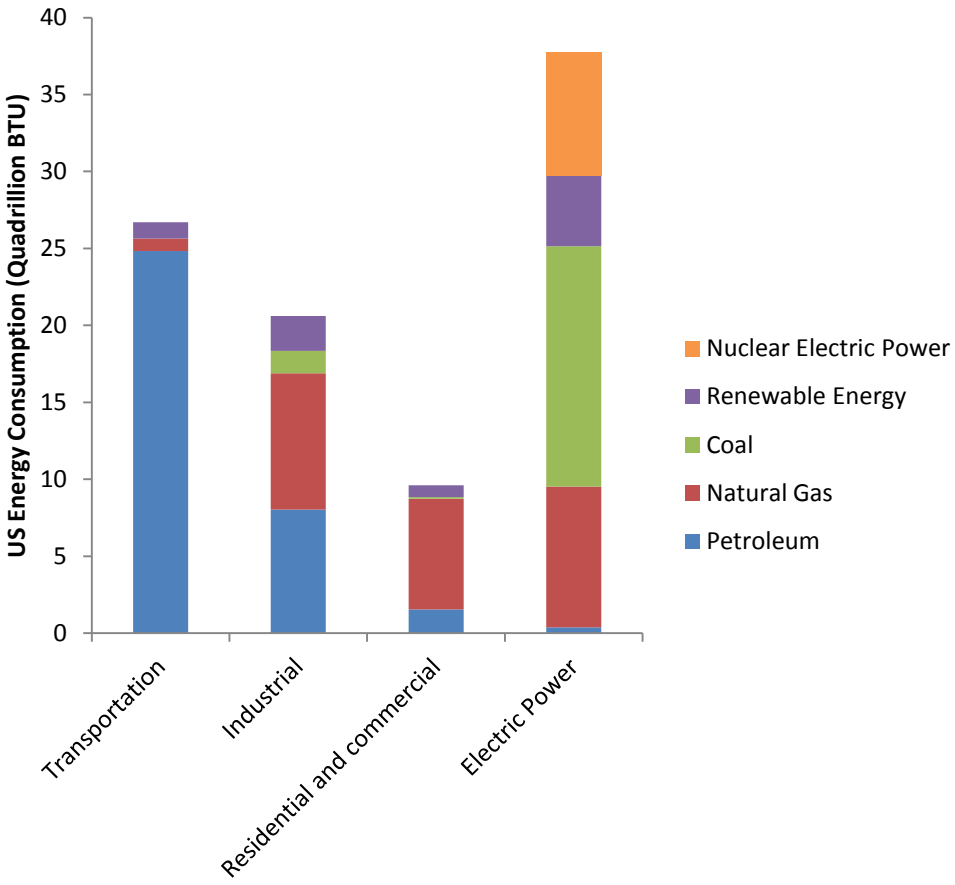

Figure 1.1: US energy consumption by sector and primary energy source. Data from the Energy Information Administration.

Although the fossil fuel resources within the United States are vast, there are concerns that the continued combustion of fossil fuels at the current rate of consumption is leading to changes in the environment [4]. Such concerns have led to research that aims to increase the efficiency of energy conversion, create fuels from carbon sources that are renewable (such as biomass), and better utilize natural gas that is currently flared. In all of these aims, catalysis has, and will continue to play a large role.

1.3 Chemical reactions and catalysis

In a chemical reaction the bonds of one or more chemical species are broken and/or new bonds are formed resulting in one or more new chemical species [5]. For combustion of a fuel this process can be represented by the following reaction:

$$aA + bO_2 \rightarrow cCO_2 + dCO + eH_2O \qquad (1.1)$$

In this reaction, A represents a carbon based fuel source that reacts with oxygen to form carbon dioxide, carbon monoxide, and water. The lower case letters represent numbers that correspond to the stoichiometric coefficients of the reaction and will vary depending on the fuel source and reaction conditions.

In order for a chemical reaction to occur, the molecules in the reaction must overcome an energy barrier known as the activation energy (Ea) [5]. Consider a reaction chamber containing methane and oxygen. At typical room conditions (1 atm, 298 K) the methane and oxygen will not react in significant amounts to form products because the activation energy has not been reached. However, if the temperature is raised many hundreds of degrees, the methane and oxygen will begin reacting to form the products in reaction 1.1. As the temperature continues to increase, more and more of the methane and oxygen will overcome the activation barrier and react to form products.

For chemical reactions, the conversion of reactants and the selectivity and yield of products are often discussed. The conversion of a reaction is the measure of the fraction of a reactant that is converted to a product at the reaction conditions. The selectivity is a measure that relates how much one product is favored over another. For instance, in the combustion reaction, either CO_2 or CO can be formed from each carbon atom in the fuel. Whether the reaction is more selective to CO_2 or CO is dependent on the reaction pathway that is most favored by the reaction conditions. In this case the selectivity to CO would be CO / (CO + CO_2). The yield of a reaction is a measure of the total amount of a specific product generated by the reaction. It is often calculated by multiplying the selectivity and conversion. Conversion, selectivity, and yield are important to consider because processes with low conversion, selectivity, or yield are often not economically favorable.

In many chemical reactions a catalyst is used to increase either the conversion or the selectivity to certain products [6]. Figure 1.2a shows a diagram of a reaction occurring on a catalyst. In Figure 1.2a, the reactant adsorbs to the catalyst surface where it interacts with another reactant on the surface to form products. The catalyst increases the conversion of a reactant by providing a surface or site that lowers the activation energy of a particular step or steps in the reaction [6]. The effect of a catalyst on the activation energy is shown in Figure 1.2b. Although the total energies of the products and reactants are the same, the energy needed to overcome the activation energy is lowered by the catalyst, increasing the reaction rate at a given reaction condition.

a)

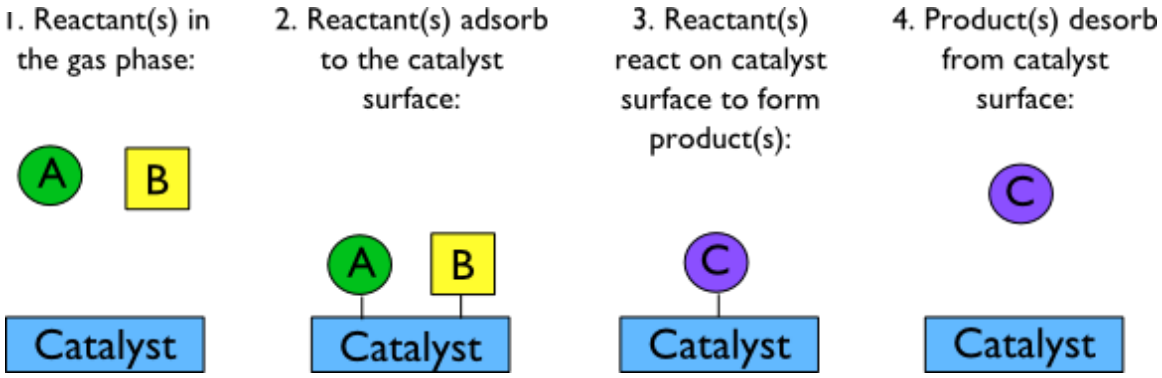

b)

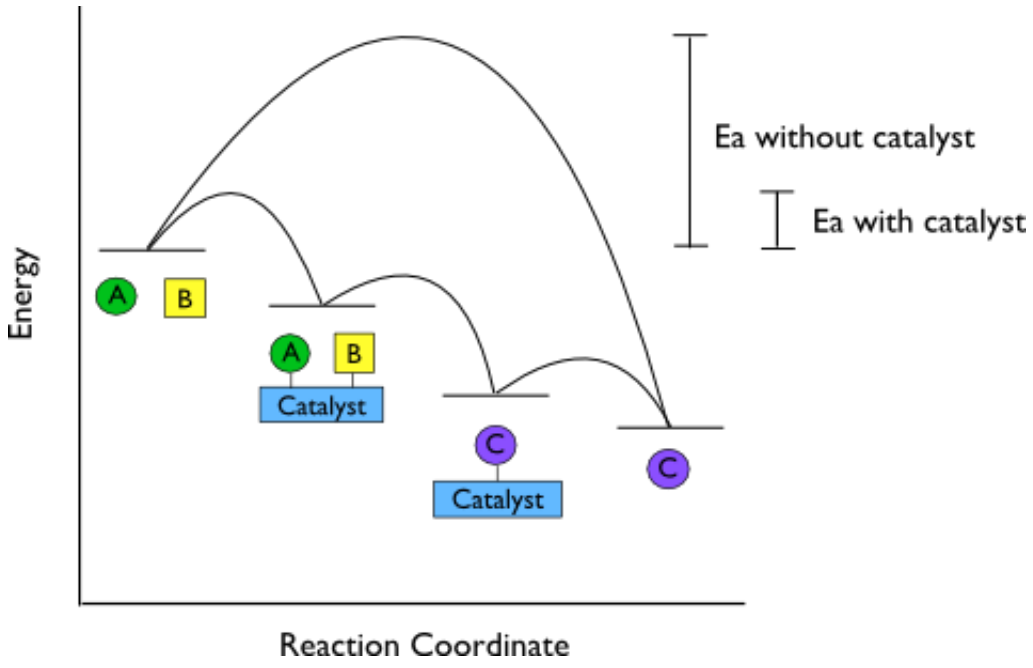

Figure 1.2. a) Diagram of a reaction occurring on a catalyst surface.
b) Reaction coordinate showing activation energy required for a reaction with and without a catalyst.

Additionally, a catalyst can increase selectivity to a product by offering sites that create a reaction pathway that is more favorable to one product than the other [6]. Because the activation energy for the reaction and the selectivity of the products (and therefore the economics of the process) are dependent on the catalyst surface sites, catalysts are a large area of both theoretical and experimental research.

1.4 Solid oxide membrane reactors

One type of chemical reactor where catalysts play a large role is solid oxide membrane reactors. A diagram of a solid oxide membrane reactor is shown in Figure 1.3. The reactor has two chambers that are separated by a gas-tight membrane made from a solid oxide material that is capable of transporting O^{2-} at high temperature (typically 873-1273 K) [7]. A gas containing oxygen (typically O_2 or air) flows into the top chamber, where a catalyst dissociates the oxygen in the stream and provides two electrons reducing each O atom to O^{2-}. The O^{2-} is then transported through the catalyst layer and the membrane layer to the opposite chamber. Here, the O^{2-} can be re-oxidized to reform O_2, or react with gases in the lower chamber. The electrons are returned to the top chamber catalyst to balance the charge. The return of the electrons occurs either via an external circuit (Figure 1.3a), or through the membrane (Figure 1.3b) depending on the whether or not the membrane is electrically conductive [8].

The transfer of O^{2-} in the solid oxide membrane is essential for the function of solid oxide membrane reactors and in this thesis it will be referred to generally as "ionic conductivity". Ionic conductivity mainly occurs in metal oxides that have either a fluorite or perovskite structure, which are depicted in Figure 1.4 [7]. The ionic conductivity of these materials is caused by oxygen vacancies in the lattice structure,

which allows oxygen anions to hop from vacancy to vacancy [7]. When coupled to a concentration or potential gradient, the movement of oxygen through the vacancies creates a flux of oxygen anions through the solid material. In order to create vacancies, the material can be "doped" with another metal cation that has a similar radius, but a different oxidation state [7]. For instance, in Figure 1.4b, if some of the gallium atoms from the B sites, which have an oxidation state of +3, are replaced with magnesium, which have an oxidation state of +2, there will be a charge imbalance. In order to preserve electrical neutrality, the amount of oxygen is decreased, leaving vacancies in the lattice. Substitutions of multivalent metals can also induce electronic conductivity into the metal oxide [7]. If gallium atoms are instead replaced with Ni, which can have an oxidation state of +2 or +3, the metal oxide will have both electronic and ionic conductivity (mixed conductivity) [9].

The ionic conductivity of a solid oxide membrane reactor is also controlled by several external factors. The factors that control the conductivity are shown in Table 1.1 along with the trend that is observed for each factor. Using a combination of these factors, it is possible to control the flux of O^{2-} through the membrane [7].

Solid oxide membrane reactors have been employed for several different purposes including: 1) Generation of very pure oxygen streams from air. 2) Partial oxidation of methane to form carbon monoxide and hydrogen 3) Generation of power via combustion across the membrane in solid oxide fuel cells. 4) Oxidative coupling of methane (OCM) to form ethane and ethylene. The use of solid oxide membrane reactors for generation of power in solid oxide fuel cells and in oxidative coupling of methane will be discussed further.

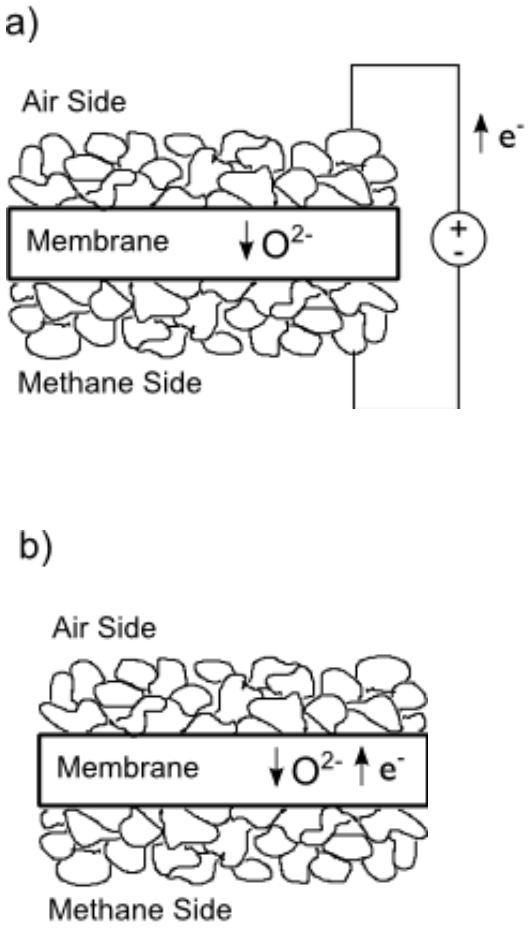

Figure 1.3. Membrane reactor diagrams: a) reactor with a membrane that is ionically conductive with an external circuit for electron transport b) reactor with a membrane with both ionic and electronic conductivity and no external circuit.

a)

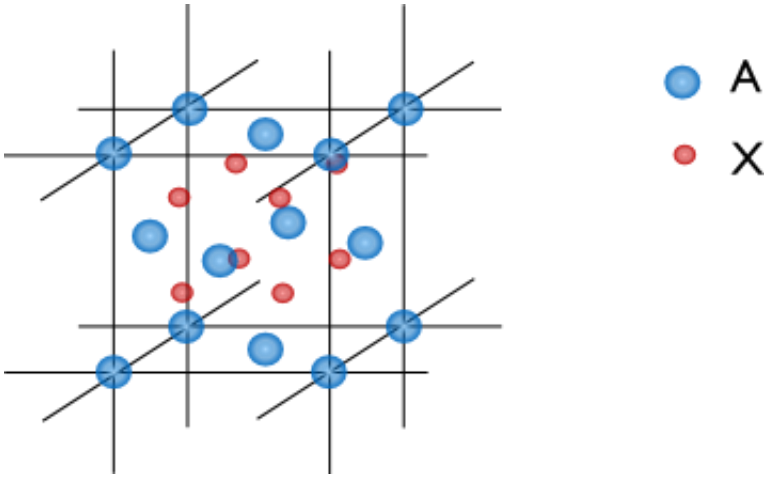

b)

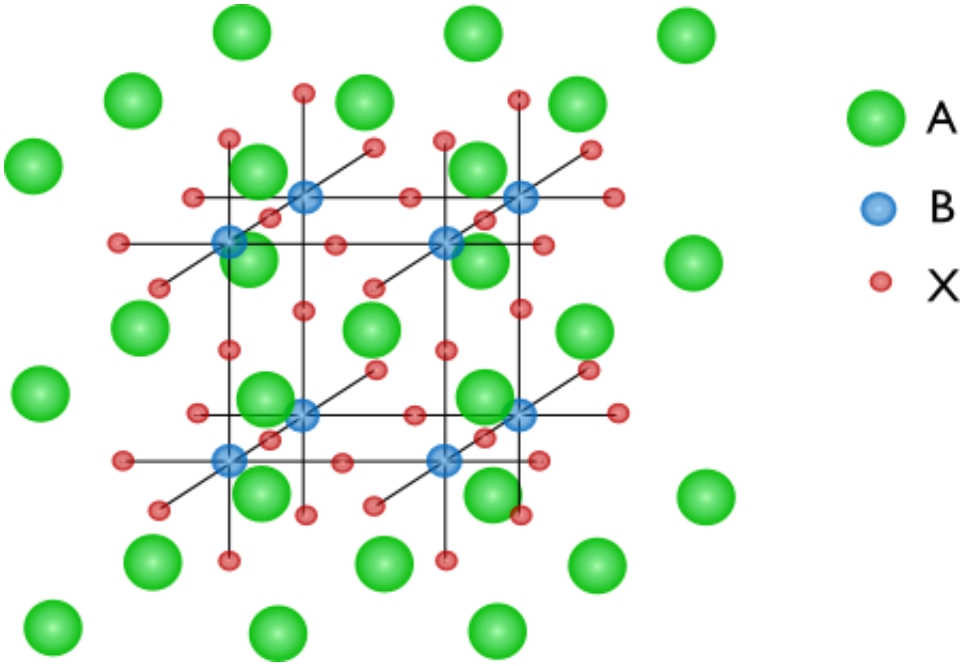

Figure 1.4. a) Fluorite structure where A represents metal atoms (e.g. Zr) and X represents oxygen atoms b) Perovskite structure where A and B represent metal atoms (e.g. La and Ga) and X represents oxygen atoms.

Table 1.1. Factors that affect the oxygen flux in a solid oxide membrane reactor

Factor	Trend
Temperature	Increasing the temperature increases the rate of surface reactions and the rate of oxygen hopping from vacancy to vacancy, thus increasing the flux
Oxygen concentration difference across the membrane	A larger difference in the oxygen concentration across the membrane increases the flux
Membrane thickness	Decreasing the thickness of the membrane decreases the resistance across the membrane, increasing the flux
Voltage difference across the membrane (non-electronically conductive membranes)	The reactions occurring on either side of the membrane determine the potential difference across the membrane. When there is no electrical contact between the sides, the voltage difference across the membrane is called the open circuit voltage. As the voltage difference is decreased, current starts to flow and is proportional to the oxygen flux. Therefore, lowering the voltage difference increases the flux. Running at negative voltages is also possible and is referred to as an "oxygen pump".
Surface catalysts	If the surface reactions are the limiting factor, the addition of a catalyst to the surface of the membrane can increase the rate of the surface reactions, increasing the flux.

1.5 Solid oxide fuel cells

One specific type of solid oxide membrane reactor is a solid oxide fuel cell (SOFC), which generates power electrochemically by converting the chemical energy in fuels to electrical energy. SOFCs have many benefits over conventional combustion technologies including noise and vibration free operation, little to no emission of criteria air pollutants NO_x and SO_x [10], and efficiencies up to 80% when waste heat is recovered [11]. SOFCs work by separating a combustion reaction into two half reactions. The half reactions are separated by the membrane, also called an electrolyte, which has good ionic conductivity but in this case does not have electronic conductivity [11]. The two half reactions determine the voltage across the cell, which can be determined theoretically using the Nernst equation (1.2), where E_{cell} is the total voltage difference across the cell, E^0_{rxn} is the difference between the reduction potentials of the half reactions at standard conditions, R is the universal gas constant, T is the absolute temperature, z is the number of moles of electrons transferred, F is Faraday's constant, and Q is the reaction quotient. Because each cell is limited to this theoretical voltage, cells are connected in series to increase the total voltage of the power source.

$$E_{cell} = E^0{}_{rxn} - \frac{RT}{zF}\ln(Q) \qquad (1.2)$$

As with all solid oxide membrane reactors, SOFCs typically operate at temperatures between 823-1273 K. High temperature operation offers several benefits including activating hydrocarbon fuels, improved tolerance of impurities, and using waste heat for combined heat and power. Figure 1.5 shows a diagram of a SOFC and the corresponding half reactions for a fuel cell operating on hydrogen (H_2). For this fuel cell,

using the Nernst equation, the theoretical voltage across the cell is found to be ~1.1V at 700°C.

In a SOFC, the reduction and oxidation catalysts are mixed with solid oxide materials in order to form electrodes that are both ionically and electronically conductive. The electrode containing the reduction catalyst, the membrane, and the electrode containing the oxidation catalyst are called the cathode, electrolyte, and anode, respectively. Although many combinations of materials can be used to create SOFCs, the most common materials are nickel/yttria-stabilized-zirconia (Ni/YSZ), YSZ, and lanthanum-strontium-manganite/YSZ (LSM/YSZ) for the anode, electrolyte, and cathode, respectively [12].

SOFCs with Ni based anodes are a particularly attractive technology because the Ni based anode can have several functions within the cell. The Ni not only conducts electricity and catalyzes the oxidation reactions, but can also reform carbonaceous fuels (with the addition of steam) to form CO and H_2 at SOFC operating conditions (600-1000°C) [12]. In theory, carbonaceous fuels can be reformed and oxidized internally in the fuel cell anode (internal reforming SOFCs), increasing the efficiency of the overall system and eliminating expensive equipment such as a pre-reformer and water-gas shift reactors; leading to systems that are portable and cost efficient. Carbonaceous fuels can also be fed directly to fuel cells (without the addition of steam), using only the oxygen coming through the electrolyte as an oxidant.

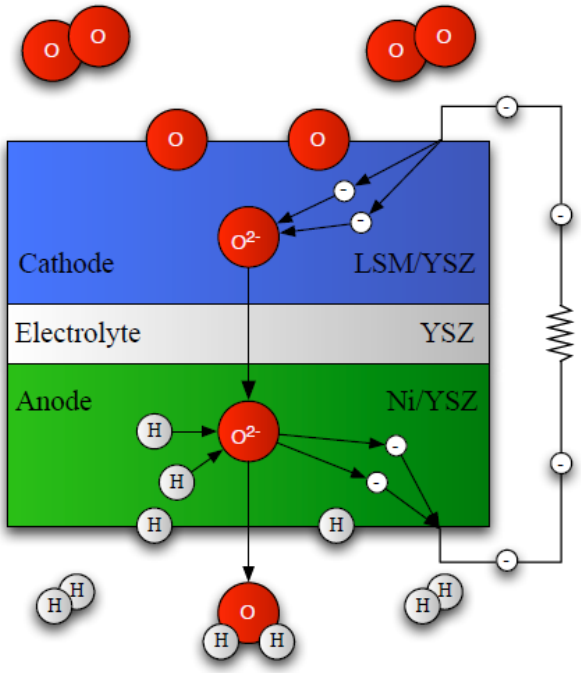

$$O_2 + 4e^- \rightarrow 2O^{2-}$$

$$2O^{2-}_{cathode} \rightarrow 2O^{2-}_{anode}$$

$$2H_2 + 2O^{2-} \rightarrow 2H_2O + 4e^-$$

$$O_2 + 2H_2 \rightarrow 2H_2O$$

Figure 1.5. Solid oxide fuel cell diagram showing reactions with hydrogen gas to form water

Direct oxidation of carbon-based fuels is beneficial to the cost and portability of SOFC power sources; however, it also leads to reliability problems [11]. A SOFC anode operating directly on a carbonaceous fuel source not only performs the reactions shown in Figure1.5, but also reforms the carbonaceous fuel [11]. In the process of reforming carbon fuels, dissociative adsorption of hydrocarbons results in carbon adsorbed on the surface of the Ni particles. The carbon can then react with oxygen to form CO or CO_2, or react with other carbon atoms to form chains of carbon called carbon nanofibers [13]. Unfortunately, Ni catalysts are known to catalyze the growth of graphitic carbon nanofibers at SOFC conditions and the growing filaments can poison the catalytic sites of the anode, and eventually cause expansion of the anode leading to cracking and failure [14]. Carbon filaments can be seen on fuel cell anodes using ex-situ techniques including scanning electron microscopy (SEM) and transmission electron microscopy (TEM) [15,16], and graphitic carbon was shown to be present on fuel cell anodes using in-situ Raman spectroscopy [17–19]. Conductivity measurements have shown that the carbon filaments also cause changes in the electrical resistance of the anode [14]. Failure by carbon deposition is a critical bottleneck for the development of SOFCs with internal reforming capabilities [10,13,20,21]. Chapter 3 discusses advancements in reducing carbon filament growth and utilizing ethanol fuel directly on Ni based SOFC anodes.

1.6 Oxidative coupling of methane

Another use for solid oxide membrane reactors is for oxidative coupling of methane (OCM) to form ethane and ethylene (C_2). Oxidative coupling of methane is a reaction where methane is directly converted to C_2 species on a metal oxide catalyst through the proposed mechanism shown in Figure 1.6a [22]. In the first step, the

methane molecule interacts with an oxygen atom at the surface of the catalyst and gives up one of its four hydrogen atoms. The remaining $*CH_3$ returns to the gas phase as a methyl radical. Subsequently, another methane molecule interacts with the OH group on the surface, gives up a hydrogen atom, and also returns to the gas phase as a methyl radical. The methyl radicals in the gas phase then couple to form ethane, and water is released from the surface of the catalyst [23]. Further oxidation of ethane leads to ethylene and can also lead to formation of CO or CO_2.

Although this process has been studied over the last several decades, it is yet to be fully commercialized because it is very difficult to obtain high yields of C_2 products. In most studies, the maximum single pass yield of C_2 products in a traditional packed bed reactor does not exceed 25% because of the formation of the undesired products CO and CO_2 (CO_x) [24]. CO_x products can be formed in two different ways [25]. First, methane can interact with the catalyst and fully dissociate (lose all H atoms), directly forming CO_x. Additionally, the methyl radicals, ethane, and ethylene that are formed can interact with oxygen on the catalyst or in the gas phase to form CO_x. Figure 1.6b shows a reaction coordinate along with the change in Gibbs Free Energy (ΔG) of each reaction at 1000 K. Although the ΔG of all of the reactions are negative, indicating that they are all thermodynamically favorable at these conditions, the very large ΔG for the CO_2 reaction indicates that CO_2 is the most favorable product. Because of these challenges, OCM reactors can be run at high C_2 selectivity and low methane conversion, or vice versa. Then, because C_2 yield is the product of C_2 selectivity and methane conversion, the yield is low at any condition. Chapters 4, 5, and 6 discuss strategies for using membrane reactors to increase the overall yield of C_2 products in OCM reactors.

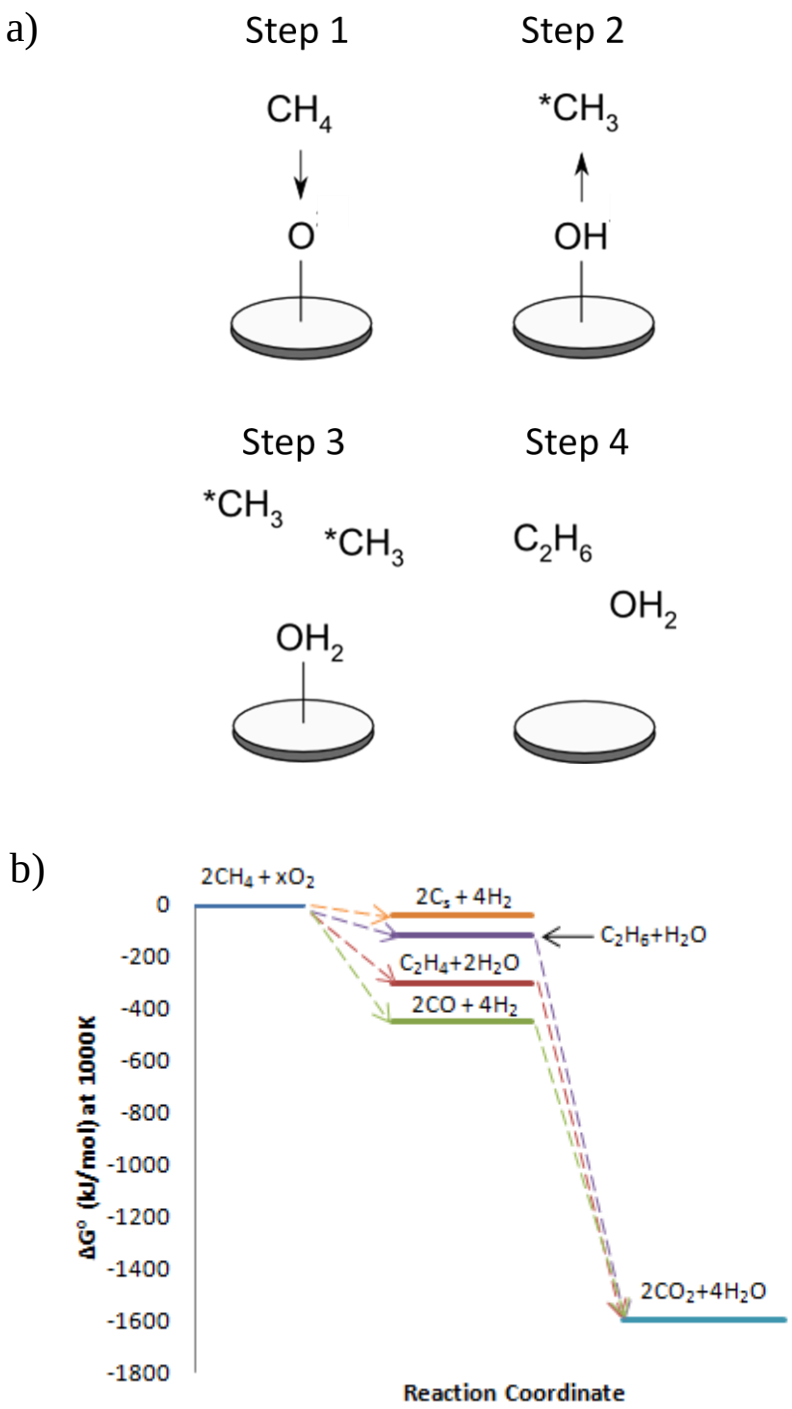

Figure 1.6. a) Basic steps of OCM on a metal oxide catalyst surface b) Gibbs Free Energy change for OCM reactions

1.7 Scope of the dissertation

The objective of this dissertation is to improve the understanding of membrane reactors and increase their usefulness in practical applications. Chapter 2 is a general overview of the fabrication methods and experimental techniques that were used to generate the data herein. Using the information in Chapter 2, other researchers should be able to reasonably duplicate the catalysts, membrane reactors, and experimental conditions that were used in this study.

Chapter 3 is focused on testing Ni and Ni alloy solid oxide fuel cell catalysts for carbon tolerance while operating on ethanol fuel. This chapter includes electrochemical and microscopy data that illuminates the electrochemical and physical changes of the anode catalysts due to carbon while operating on ethanol fuel.

In Chapter 4, the topic is switched to oxidative coupling of methane. This chapter further discusses the challenges of commercializing OCM processes and compares the theoretical yield of C_2 products in membrane and packed bed reactors using published kinetic data. This chapter also identifies key areas where research and development should be focused in order to maximize the C_2 yield of membrane reactors.

In Chapter 5, a catalyst screening is presented to determine if the materials commonly used in solid oxide fuel cell technology have activity and selectivity for OCM. The materials chosen to be tested have the required properties for use in membrane reactors, and contain elements that have shown high selectivity to C_2 products in previous studies. Chapter 5 contains methane conversion and C_{2+} selectivity data for lanthanum gallate doped with strontium and magnesium (LSGM) with and without 1% Li, lanthanum strontium cobalt ferrite (LSCF), and lanthanum strontium manganite (LSM)

collected in a packed bed reactor. Through this screening, it was found that the LSGM materials show promising catalytic activity and selectivity, and the results of further testing for trends with reaction temperature and stability over time are presented in Chapter 5 for these materials.

In Chapter 6, results are presented for membrane reactors fabricated using the 1% Li-LSGM material from the catalyst screening in Chapter 5 as a methane side catalyst. This chapter includes details on the fabrication and characterization of small planar disk membrane reactors with mixed conducting membranes, as well as results from testing the reactors using high partial pressures of methane. Two membrane materials were tested: LSCF and LSGM that has been doped with Ni. The membrane reactors were tested at temperatures between 1023 and 1173 K and the data presented include O^{2-} flux through the membranes, CH_4 conversion, and C_2 product selectivity and yield. Chapter 6 also shows the stability of the reactors over time.

Chapter 7 is the final chapter of the dissertation. This chapter states the general conclusions of the studies presented in this dissertation and ends with suggested future work that would build on the study presented here.

1.8 References

[1] Energy Information Administration, Annual Energy Review, (2012). http://www.eia.gov/totalenergy/data/annual/index.cfm (accessed January 1, 2015).

[2] A. Sieminski, Energy Markets and Projections, (2014). Energy Information Administration. http://www.nga.org/files/live/sites/NGA/files/pdf/SieminskiNGA072414Final.pdf

[3] Energy Information Administration, North Dakota aims to reduce natual gas flaring, (2014). http://www.eia.gov/todayinenergy/detail.cfm?id=18451.

[4] Core Writing Team, R.K. Pachauri, L.A. Meyer, Climate Change 2014: Synthesis Report. Contribution of Working Groups I, II and III to the Fifth Assessment Report of the Intergovernmental Panel on Climate Change, Geneva, Switzerland, n.d.

[5] H.S. Fogler, Elements of Chemical Reaction Engineering, 4th ed., Pearson Education, Inc, Upper Saddle River, 2006.

[6] I. Chorkendorff, J.W. Niemantsverdriet, Concepts of Modern Catalysis and Kinetics, WILEY-VCH Verlag GmbH & Co. KGaA, Weinheim, 2003.

[7] J. Sunarso, S. Baumann, J.M. Serra, W. a. Meulenberg, S. Liu, Y.S. Lin, et al., Mixed ionic-electronic conducting (MIEC) ceramic-based membranes for oxygen separation, J. Memb. Sci. 320 (2008) 13–41. doi:10.1016/j.memsci.2008.03.074.

[8] D. Eng, M. Stoukides, Catalytic and Electrocatalytic Methane Oxidation with Solid Oxide Membranes, Catal. Rev. 33 (1991) 375–412. doi:10.1080/01614949108020304.

[9] T. Ishihara, T. Yamada, H. Arikawa, H. Nishiguchi, Y. Takita, Mixed electronic – oxide ionic conductivity and oxygen permeating property of Fe- , Co- or Ni-doped LaGaO 3 perovskite oxide, Solid State Ionics. 135 (2000) 631–636. doi:10.1246/cl.1999.1257.

[10] A. Atkinson, S. Barnett, R.J. Gorte, J.T.S. Irvine, a J. McEvoy, M. Mogensen, et al., Advanced anodes for high-temperature fuel cells., Nat. Mater. 3 (2004) 17–27. doi:10.1038/nmat1040.

[11] R.M. Ormerod, Solid oxide fuel cells, Chem. Soc. Rev. 32 (2003) 17–28. doi:10.1039/b105764m.

[12] S.C. Singhal, K. Kendall, High-temperature Solid Oxide Fuel Cells: Fundamentals, Design and Applications, Elsevier, 2003.

[13] E. Nikolla, A. Holewinski, J. Schwank, S. Linic, Controlling carbon surface chemistry by alloying: carbon tolerant reforming catalyst., J. Am. Chem. Soc. 128 (2006) 11354–5. doi:10.1021/ja0638298.

[14] Y. Kim, J.H. Kim, J. Bae, C.W. Yoon, S.W. Nam, In Situ Analyses of Carbon Dissolution into Ni-YSZ Anode Materials, J. Phys. Chem. C. 116 (2012) 13281–13288. doi:10.1021/jp3035693.

[15] S. Helveg, C. Lopez-Cartes, J. Sehested, P. Hansen, B. Clausen, J. Rostrup-Nielsen, et al., Atomic-scale imaging of carbon nanofibre growth, Nature. 427 (2004) 426–429. doi:10.1038/nature02308.1.

[16] F. Abild-Pedersen, J. Nørskov, J. Rostrup-Nielsen, J. Sehested, S. Helveg, Mechanisms for catalytic carbon nanofiber growth studied by ab initio density

functional theory calculations, Phys. Rev. B. 73 (2006) 1–13. doi:10.1103/PhysRevB.73.115419.

[17] M.B. Pomfret, J.C. Owrutsky, R. a Walker, High-temperature Raman spectroscopy of solid oxide fuel cell materials and processes., J. Phys. Chem. B. 110 (2006) 17305–8. doi:10.1021/jp063952l.

[18] M.B. Pomfret, J.C. Owrutsky, R. a Walker, In situ studies of fuel oxidation in solid oxide fuel cells., Anal. Chem. 79 (2007) 2367–72. doi:10.1021/ac062189o.

[19] M.B. Pomfret, J. Marda, G.S. Jackson, B.W. Eichhorn, a. M. Dean, R. a. Walker, Hydrocarbon Fuels in Solid Oxide Fuel Cells: In Situ Raman Studies of Graphite Formation and Oxidation, J. Phys. Chem. C. 112 (2008) 5232–5240. doi:10.1021/jp711312p.

[20] S. Park, J. Vohs, R. Gorte, Direct oxidation of hydrocarbons in a solid-oxide fuel cell, Nature. 404 (2000) 265–7. doi:10.1038/35005040.

[21] E. Nikolla, J. Schwank, S. Linic, Direct Electrochemical Oxidation of Hydrocarbon Fuels on SOFCs: Improved Carbon Tolerance of Ni Alloy Anodes, J. Electrochem. Soc. 156 (2009) B1312–B1316. doi:10.1149/1.3208060.

[22] J.H. Lunsford, Catalytic conversion of methane to more useful chemicals and fuels: A challenge for the 21st century, Catal. Today. 63 (2000) 165–174. doi:10.1016/S0920-5861(00)00456-9.

[23] L. Luo, X. Tang, W. Wang, Y. Wang, S. Sun, F. Qi, et al., Methyl Radicals in Oxidative Coupling of Methane Directly Confirmed by Synchrotron VUV Photoionization Mass Spectroscopy., Sci. Rep. 3 (2013) 1625. doi:10.1038/srep01625.

[24] U. Zavyalova, M. Holena, R. Schlögl, M. Baerns, Statistical analysis of past catalytic data on oxidative methane coupling for new insights into the composition of high-performance catalysts, ChemCatChem. 3 (2011) 1935–1947. doi:10.1002/cctc.201100186.

[25] Z. Stansch, L. Mleczko, M. Baerns, Comprehensive Kinetics of Oxidative Coupling of Methane over the La_2O_3 /CaO Catalyst, Ind. Eng. Chem. Res. 36 (1997) 2568–2579. doi:10.1021/ie960562k.

Chapter 2

Experimental Techniques

2.1 Summary

This chapter describes the theoretical and experimental techniques used to generate the data presented in this thesis. Using the information in this chapter, other researchers should be able to reasonably duplicate the catalysts, membrane reactors, and experimental conditions that were used in this study. The chapter begins with the experimental procedures that were followed to synthesize and fabricate the catalysts and reactors, then goes on to explain the experimental setups and procedures that were used for testing. In the last part of the chapter, a brief description is given on the theory and background for each technique used to collect experimental and characterization data.

2.2 Catalyst Preparation and Membrane Reactor Fabrication

2.2.1 Solid oxide fuel cells

The solid oxide fuel cells used in this study were anode-supported button cells similar to those fabricated by Nikolla et al. [1]. To fabricate the fuel cells, first powders of NiO, yttria stabilized zirconia (YSZ), and graphite were mixed in a mass ratio of 1:1:0.6. The powders were made into a slurry with de-ionized water and a dispersant. Details for each of the chemicals used to make the fuel cells and the quantities used in a typical batch are provided in Table 2.1. The slurry was placed in a ball mill with zirconia media and ground for ~24 hours. The water was then evaporated from the slurry under constant stirring, and the resultant powder was forced through a 200 mesh sieve. Portions of the powder weighing 0.2 g each were then pressed into disks 15 mm in diameter using 750 kg of pressure in a pellet press. The disks were transferred to a furnace and heated to 1273 K for 4 hours in air using heating and cooling rates of 2 K/min. At this point, Sn was added to some of the fuel cell anodes. $SnCl_2*2H_2O$ was dissolved in ethanol and added to the anode catalyst pellets using the incipient wetness technique. Enough solution was added to the pellets to result in 1% Sn on a metals basis (Sn/(Ni + Sn)). In order to not over saturate the pellets, the solution was added in three additions, allowing the pellet to dry between additions.

The electrolyte layer was added to each of the anode pellets using a drop coating technique. To make the electrolyte solution, 0.2 g of YSZ was mixed with 20 mL ethanol and 24 drops of Ethocel-300 solution (0.1g Ethocel-300 in 10 mL ethanol). The mixture was placed in a sonicator until a uniform suspension formed (at least 10 min). Immediately following sonication, the suspension was then added in a total of 12, 65 μL

additions to the surface of the pellets using a micropipette, allowing the pellets to dry completely between additions. The pellets were then transferred to zirconia plates and sintered in air at 1723 K for 4 hours using heating and cooling rates of 1 K/min.

Table 2.1: Solid oxide fuel cell materials

Chemical	Manufacturer	Purity	Particle Size	Typical amount used
Anode Powder				0.2 g/cell
Nickel Oxide (NiO)	Alfa Aesar	99%	325 mesh	10 g
Yttria stabilized zirconia (YSZ, 8%)	Tosoh			10 g
Graphite	Alfa Aesar	99%	300 mesh	6 g
Dispersant (Duramax^{TM} D-3005)	Dow Chemical			6 drops
Tin Solution				114 μL
Tin Chloride ($SnCl_2$*$2H_2O$)	Alfa Aesar	Reagent Grade		0.2 g
Ethanol	Fisher	92.7%		20 mL
Electrolyte Solution				0.78 mL
Yttria stabilized zirconia (YSZ, 8%)	Tosoh			0.2 g
Ethanol	Fisher	92.7%		20 mL
Ethocel Solution				24 drops
Ethocel-300	Dow Chemical			0.1 g
Ethanol				10 mL
Cathode Powders				
Lanthanum strontium manganite $La_{0.8}Sr_{0.2}Mn_{0.98}O_{3-\delta}$	Praxair	99.9%	1.1μm (d50)	
Yttria stabilized zirconia (YSZ, 8%)	Tosoh			
Graphite	Alfa Aesar	99%	300 mesh	
Ceramabond-552	Aremco			

A dual layer cathode was then painted onto the surface of the electrolyte side of the fuel cell disks. The first layer was a 1:1 weight ratio mixture of lanthanum strontium manganite (LaSrMnO3, LSM) and yttria stabilized zirconia. The powders were placed in a ball mill with zirconia media and water for 24 hours before being dried and re-suspended in ethanol. A thin layer was painted on the surface of the electrolyte, dried, and heated to 673 K for 2 hours using heating and cooling rates of 2 K/min. The second layer was a 4:1 weight ratio mixture of LSM and graphite, which were also placed in a ball mill with zirconia media and water for 24 hours, dried, and re-suspended in ethanol to make a paint. This second suspension was painted on top of the first cathode layer, and heated to 1423 K for 2 hours using heating and cooling rates of 2 K/min.

Electrical connections to the anode and cathode were made with gold wires and silver paste. On the anode side, two gold wires were secured around the perimeter of the fuel cell with silver paste. On the cathode side two gold wires and gold mesh were secured on the outer edges of the cathode area, leaving an effective cathode area of ~0.15 cm^2. The fuel cell was then secured to an alumina tube using a ceramic sealant, and placed in a tube furnace.

The furnace containing the alumina tube and fuel cell was heated at 1 K/min to 373 K and held at that temperature for 2 hours, then heated at 1 K/min to 573 K and held for another 2 hours to fully cure the ceramic sealant. Then the temperature was increased at 0.8 K/min to 973 K. At this time, the anode side of the fuel cell was purged with Ar gas, and then switched to hydrogen gas flowing at 120 sccm. The fuel cells were held under hydrogen flow for 16 hours at 973 K to fully reduce the NiO in the anode to Ni.

2.2.2 Oxidative coupling of methane packed bed reactor catalysts

The catalysts used for oxidative coupling of methane in the packed bed reactor were formed into porous pellets. The details for all of the materials used in this procedure are included in Table 2.2. First, each catalyst was mixed with graphite in a 1:0.56 weight ratio in a mortar and pestle. The powder was pressed into cylindrical pellets that were 6 mm in diameter and about 3.5 mm in length using 750 kg of pressure in a pellet press. The pellets were placed in a furnace and heated to 1273 K for 4 hours in air using heating and cooling rates of 2 K/min to remove the graphite pore former. Li was added to some of the pellets using the following incipient wetness technique procedure: Li_2CO_3 was dissolved in water and enough of the solution was added to each pellet to obtain 1% Li on a mass basis. In order to not over-saturate the pellets, the Li_2CO_3 solution was added in several additions (~10) and dried at 348 K between additions.

For each of the catalyst tests, 1 catalyst pellet weighing 0.11 g was placed in the center of an alumina tube with an inner diameter of ¼". Silica wool was added to both sides of the catalyst pellet to prevent catalyst movement in the tube. The alumina tube was then placed in a tube furnace and heated to the reaction temperature under 40 sccm flow of Ar. The catalysts were held at the reaction temperature under Ar flow for ~8 hours before catalytic tests began.

Table 2.2: Oxidative coupling of methane packed bed reactor materials

Chemical	Manufacturer	Purity	Particle Size	Surface Area m^2/g
Catalysts				
$La_{0.8}Sr_{0.2}Ga_{0.8}Mg_{0.2}O_{3-\delta}$	Sigma Aldrich	99%	0.8 d50 (μm)	4
$La_{0.6}Sr_{0.4}Co_{0.2}Fe_{0.8}O_{3-\delta}$	Sigma Aldrich		0.4 d50 (μm)	5.5
$La_{0.8}Sr_{0.2}Mn_{0.98}O_{3-\delta}$	Praxair	99.9%	1.1 d50 (μm)	4.77
Pore Former				
Graphite	Alfa Aesar	99%	300 mesh	
Lithium Solution				
Lithium Carbonate (Li_2CO_3)	Fisher	99+%		
Ethanol	Fisher	92.7%		

2.2.3 Oxidative coupling of methane membrane reactors

The membrane reactors for oxidative coupling of methane were disk shaped membrane supported reactors. The details for all of the materials used in this procedure can be found in Table 2.3. The membrane materials used in the study were LSGM, LSCF, and 15% Ni-LSGM. The LSGM and LSCF materials were used as received from the manufacturer. The 15% Ni-LSGM material was synthesized using the following procedure: NiO and LSGM powders were ground together in a mortar and pestle in a weight ratio of 0.28:5. The resultant powder was heated in air to 1273 K in air using heating and cooling rates of 2 K/min. Membrane disks were fabricated by loading 0.18 g of the membrane material into a 15 mm diameter cylindrical pellet die and pressing in a pellet press using 750 kg of pressure. The disks were then sintered at 1723 K in air for 4

hours using heating and cooling rates of 1 K/min. The resulting disks were 12 mm in diameter and ~200 μm thick as measured by scanning electron microscopy.

Catalysts were added to each side of the membrane before testing. For the methane side catalyst, LSGM and graphite were mixed using a mortar and pestle in a 3:1 weight ratio. To add the catalyst to the surface of the membrane, 0.05 grams of the catalyst powder was suspended in 150 μL of ethanol. 25 μL of the suspension was added to each of the membrane pellets and dried in air. The air side catalyst was then added to the opposite side of the membrane. The air side catalyst was prepared by mixing LSCF and graphite in a 1:0.56 weight ratio in a mortar and pestle. Ethanol was added to the powder to make a suspension which was then painted onto the surface of the membrane (on the opposite side from the methane catalyst). The membrane reactors were then heated in air to 1423 K for 2 hours at heating and cooling rates of 2 K/min. Li was added to the methane side catalyst using the same incipient wetness technique as described in Section 2.2.2.

2.3 Experimental Setups

2.3.1 Solid Oxide Fuel Cell (SOFC) Experiments

The solid oxide fuel cell experiments were performed using the experimental setup shown in Figure 2.1. On the anode side of the fuel cell, hydrogen and argon gases were connected to a mass flow controller, and could be sent through the ethanol bubbler or through the bypass before flowing up a quartz tube that ends just before the surface of the anode. The anode gas then reacted on the surface of the anode and flowed back down the outside of the quartz tube. On the cathode side of the fuel cell the air flow was controlled

Table 2.3: Oxidative coupling of methane membrane reactor materials

Chemical	Manufacturer	Purity	Particle Size	Typical amount used
LSCF Membrane				0.18 g/membrane
$La_{0.6}Sr_{0.4}Co_{0.2}Fe_{0.8}O_{3-\delta}$	Sigma Aldrich		0.4 d50 (μm)	
Ni-LSGM Membrane				0.18 g/membrane
$La_{0.8}Sr_{0.2}Ga_{0.8}Mg_{0.2}O_{3-\delta}$	Sigma Aldrich	99%	0.8 d50 (μm)	5 g
Nickel Oxide (NiO)	Alfa Aesar	99%	325 mesh	0.28 g
Methane Catalyst				8.3 mg/reactor
$La_{0.8}Sr_{0.2}Ga_{0.8}Mg_{0.2}O_{3-\delta}$	Sigma Aldrich	99%	0.8 d50 (μm)	0.75 g
Graphite	Alfa Aesar	99%	300 mesh	0.25 g
Lithium Solution				40 μL/ reactor
Lithium Carbonate (Li_2CO_3)	Fisher	99+%		0.25 g
Ethanol	Fisher	92.7%		20 mL
Air Catalyst				
$La_{0.6}Sr_{0.4}Co_{0.2}Fe_{0.8}O_{3-\delta}$	Sigma Aldrich		0.4 d50 (μm)	1 g
Graphite	Alfa Aesar	99%	300 mesh	0.56 g

by a rotometer, and flowed through a quartz tube ending just above the cathode surface. There were two K type thermocouples in the system, one in the furnace wall and one a few millimeters above the surface of the cathode (not shown). The thermocouple just above the cathode was used to determine the stated temperature of the system.

The gold fuel cell wires were connected to a PARSTAT 2273 (Princeton Applied Research) potentiostat to control the working potential and monitor the current through the system. In this two electrode system, the anode was used as both the working and sensing electrode, and the cathode was used as the counter and reference electrode.

2.3.2 Oxidative Coupling of Methane Packed Bed Reactor Experiments

The packed bed reactor experiments were performed using the experimental setup shown in Figure 2.2. Argon, air and a methane mixture of 95% methane and 5% He were controlled by mass flow controllers and fed into an alumina tube within a horizontal furnace. The effluent gas was analyzed by a Varian CP-3800 GC with two thermal conductivity detectors and a flame ionization detector. Details about the GC method and apparatus are given in Section 2.5.

2.3.3 Oxidative Coupling of Methane Membrane Reactor Experiments

The membrane reactor experiments for oxidative coupling of methane were performed using the experimental setup shown in Figure 2.3. In each experiment, a membrane reactor was fused using a sealant containing glass powder (Bullseye Glass) onto the end of an alumina tube with the methane side catalyst facing the inside of the tube. On the methane side, a methane mixture (95% methane, 5% He) and argon gas were controlled by mass flow controllers. The gases flowed up an inner quartz tube, reacted at the methane side catalyst surface, and flowed back down an alumina tube where they were analyzed by gas chromatography. On the air side, air flowed down a quartz tube that ended just above the surface of the air side catalyst. The temperature of the system was monitored by a thermocouple that was also located just above the surface of the membrane disk.

2.4 Electrochemical Techniques

In the SOFC experiments, several electrochemical techniques were used to monitor the changes in the fuel cells over time. All of the following techniques were performed using a PARSTAT 2273 (Princeton Applied Research) potentiostat.

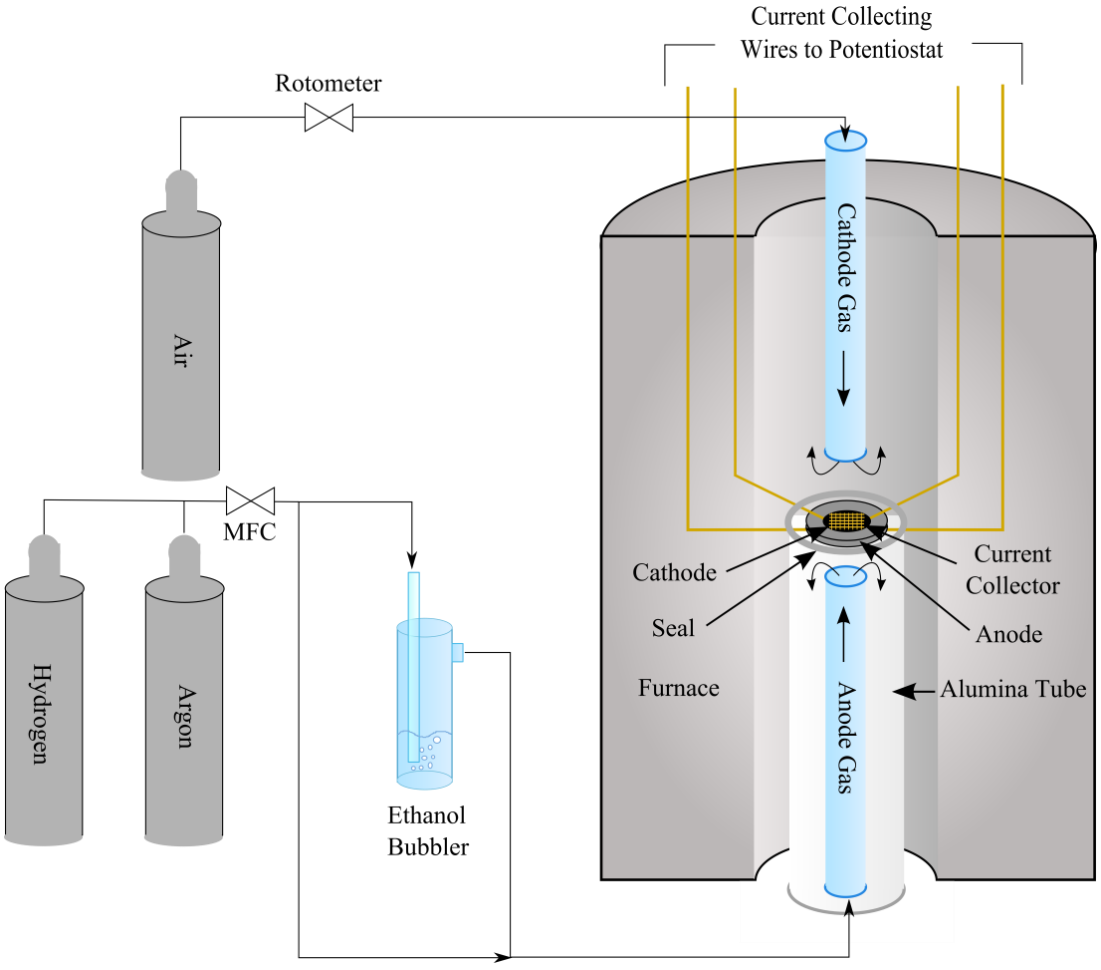

Figure 2.1: Solid oxide fuel cell experimental setup

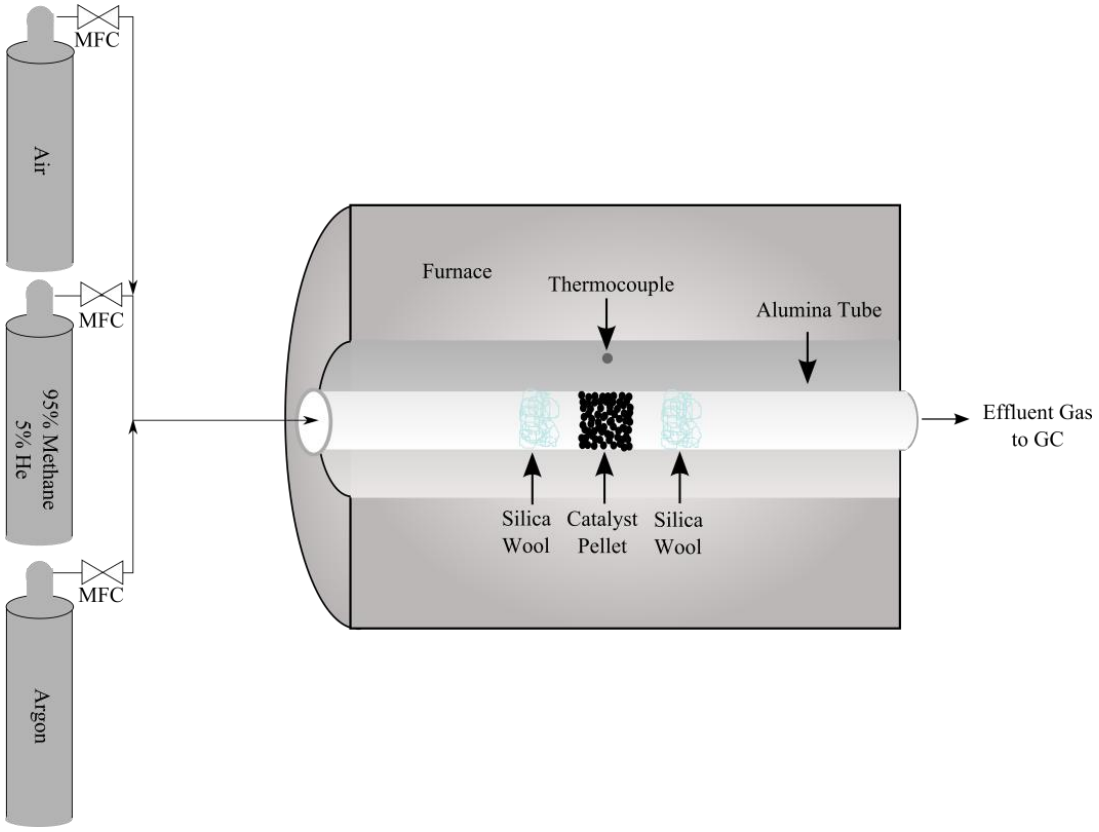

Figure 2.2: OCM packed bed reactor experimental setup

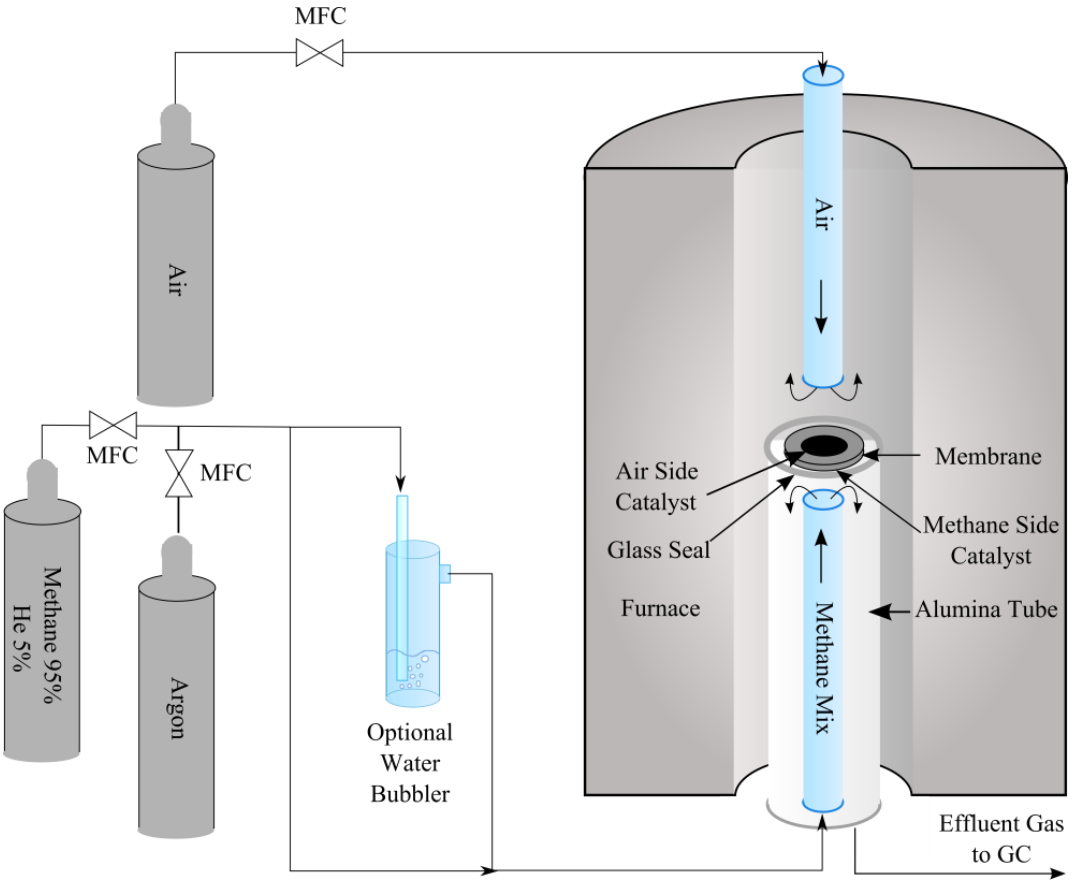

Figure 2.3: OCM membrane reactor experimental setup

2.4.1 Current-Voltage Curves

Current-Voltage curves (or I-V curves) are used to determine the current in an electrochemical system over a range of potentials. In a two electrode system such as the one described in Section 2.3.1, the potential difference between the electrodes is considered the potential (or voltage) of the system. To make an I-V curve, the potentiostat sets potential of the system at a certain value then increases or decreases the potential at a specified rate while recording the response in terms of current [2]. The potential can either be changed continuously, or it can be changed in step-wise, holding each potential for a specified amount of time. In this study, all I-V curves were started at the open circuit potential of the system (~1.1 V) and the potential was decreased in steps by 0.02 V every 10 seconds ending at a potential of 0.1 V.

Figure 2.4 is a diagram of an I-V curve showing a representative excitation voltage, along with a typical current response. There are three distinct regions of the polarization curve as the ΔV of the system decreases; activation polarization at high ΔV, ohmic polarization at intermediate ΔV, and concentration polarization at low ΔV [3]. At high ΔV, the rate of the reactions at the surface of the electrodes controls the overall rate of electron transfer in the system, which is also known as the current. At intermediate ΔV, the ohmic resistance across the fuel cell controls the current. In this region, the current increases nearly linearly as the ΔV decreases. Finally, at low ΔV the current is controlled by the transfer of reactants from the gas phase to the surface of the electrodes. Using this information, the changes in the I-V curves over time can be used to understand physical changes that are occurring within the fuel cell.

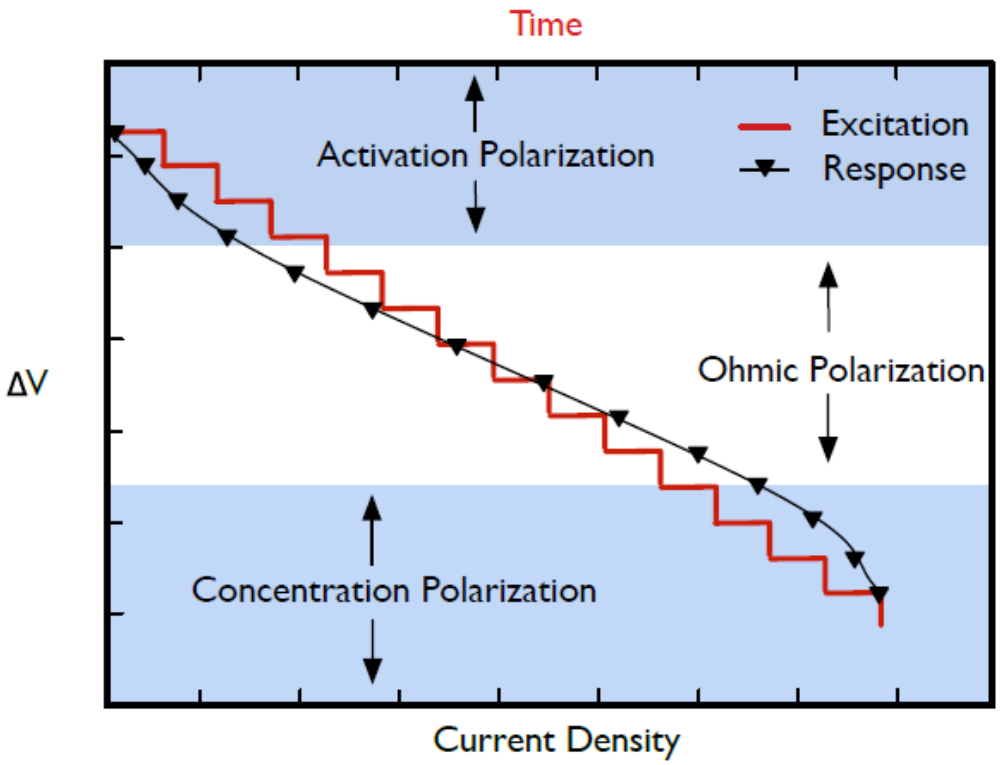

Figure 2.4: Current-Polarization curves showing the voltage excitation (red, top axis), the current response (black, bottom axis), and the three polarization regions

2.4.2 Impedance Spectroscopy

Impedance spectroscopy is an electrochemical technique that can be used to understand the resistance of a fuel cell to the flow of electrons. In this technique, a small sinusoidal potential excitation is applied to the fuel cell at varied frequencies while monitoring the current response [4]. The excitation signal can be described mathematically by equation 2.1, where E_t is the potential at time t, E_0 is the amplitude of the signal, and ω is the radial frequency. The radial frequency is related to the frequency (*f*) using equation 2.2. When the potential frequency is applied to the system, the response in the current can be described by equation 2.3, where I_t is the current at time t, I_0 is the amplitude of the current response, and ∅ is the shift in phase. The impedance of the system (Z) can then be described using equation 2.4 and by using Euler's relationship Z can be expressed as the complex function shown in equation 2.5.

$$E_t = E_0 sin(\omega t) \quad (2.1)$$

$$\omega = 2\pi f \quad (2.2)$$

$$I_t = I_0 sin(\omega t + \emptyset) \quad (2.3)$$

$$Z = \frac{E_t}{I_t} = \frac{E_0 sin(\omega t)}{I_0 sin(\omega t + \emptyset)} = Z_0 \frac{sin(\omega t)}{sin(\omega t + \emptyset)} \quad (2.4)$$

$$Z = \frac{E}{I} = Z_0 \exp(j\emptyset) = Z_0(cos\emptyset + jsin\emptyset) \quad (2.5)$$

When the real and imaginary components of Z are plotted on the x and y axis, respectively, the result is a Nyquist plot like the one shown in Figure 2.5. In these plots, each frequency tested is represented by a single data point. Although the excitation frequency is not shown in this type of plot, the excitation frequency decreases from left to

right on the plot. In this work, the frequency was varied from 100 kHz to 0.1 Hz. The total impedance of the system can be described by a vector from the origin to the data, where ∅ is the angle between the vector and the x axis. These plots are very useful because the impedances due to the electrolyte and the electrodes can be easily identified by the points where the data crosses the x axis, as shown in Figure 2.5.

To interpret impedance data, it is useful to make an equivalent circuit model such as the one used in this work, which is shown in Figure 2.6. Although there are many different equivalent circuits that can be used to model SOFCs, this simple model which has been adapted from the model used by Leng et al. fits the system well [5]. In this model R_0 represents an ohmic resistance in the system, which is not affected by the frequency of the excitation. The three parallel circuits represent an impedance due to the electrodes, each with a different characteristic frequency. At high frequency, the CPE elements have very little impedance, and therefore the total resistance is due to R_0 which is mainly due to the electrolyte ($R_0 \approx R_{Elec}$) and has no imaginary part. As the frequency decreases, the impedance of the CPEs increase and current flows through both the CPE and the resistor, creating a semi-circular plot as shown in Figure 2.5. At very low frequencies, the CPEs act as infinite resistors, and all of the current flows through R_1, R_2, and R_3, which represent the total polarization resistance of the system.

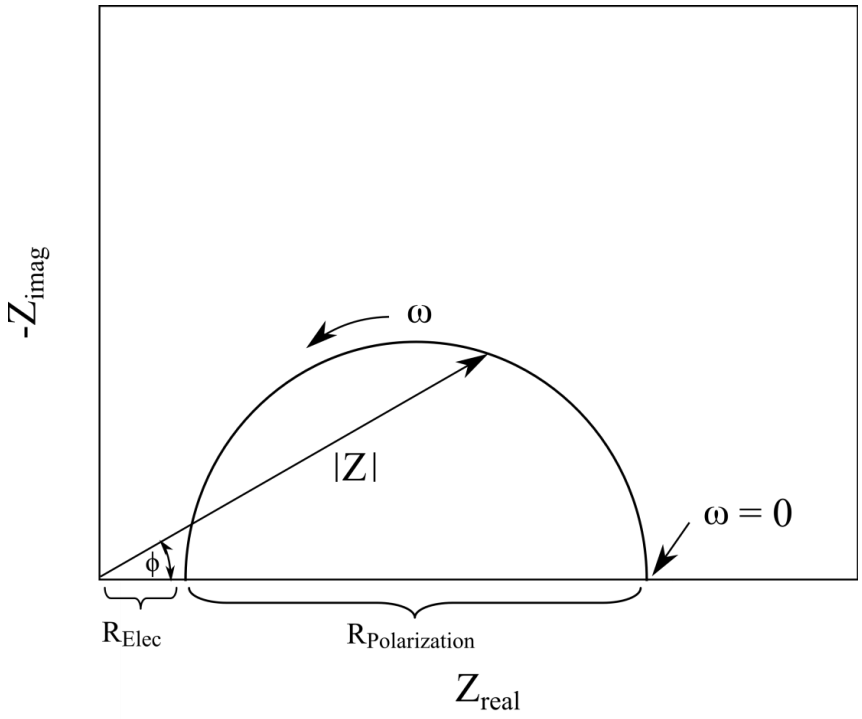

Figure 2.5: Nyquist Plot

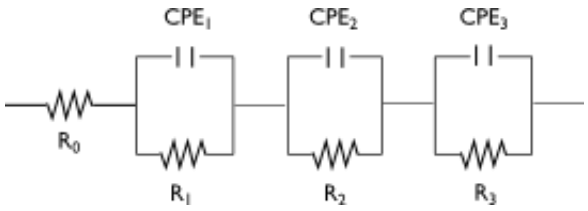

Symbol	Name	Impedance
R	Ohmic Resistor	R
L	Inductor	$j\omega L$
C	Capacitor	$^{1}/_{j\omega C}$
CPE	Constant Phase Element	$^{1}/_{Y_0(j\omega)^{\alpha}}$

Figure 2.6: Equivalent circuit model commonly used for SOFCs with a table of common circuit elements and their calculated impedance

Although modeling using equivalent circuits can provide numerical values for the elements in Figure 2.6, providing physical interpretations for those impedances (beyond R_0) is very difficult on SOFCs with thin film electrolytes. This is due to the fact that placing a reliable reference electrode in the system is nearly impossible, and therefore the polarization resistances cannot be attributed to either electrode with any certainty [6]. In this study we have not attempted to include a reference electrode and therefore we have limited our discussion to the total ohmic and polarization resistances.

2.5 Gas Chromatography

In the OCM studies included in this dissertation, gas chromatography was used to determine the type and quantity of chemicals present in the effluent gas. In gas chromatography, a small amount of the effluent sample is injected into a column along with a carrier gas (Ar or He). The sample interacts with the column, adsorbing to the solid surfaces. The components of the sample then migrate through the column at different velocities depending on the strength of their interaction with the solid phase, which causes the components to exit the column at different times [7]. This process can be further facilitated by heating the column if necessary. As the components of the sample exit the column, they are sent to a detector.

The detectors used in the OCM studies were thermal conductivity detectors (TCD) and a flame ionization detector (FID). In the TCDs the detector measures the change in resistance of a heated filament as the eluted gas passes over it. The change in the resistance is caused by a change in temperature of the filament due to the difference in the thermal conductivity of the sample compared to the carrier gas [7]. In the FID, the

eluted gas is injected into a flame produced from combusting hydrogen and air. Within the flame, the carbon components combust creating CHO^+ and H_3O^+ ions. The ions are collected by a detector, causing a current to flow which is proportional to the amount of C in the sample [7].

The gas chromatography system used to collect the data included in this dissertation was a Varian CP-3800 Natural Gas Analyzer. This GC has three sample loops. The first uses argon as a carrier gas and detects hydrogen and helium using a TCD. The second uses helium as a carrier gas and detects N_2, O_2, Ar, CH_4, CO, CO_2, Ethylene, Acetylene, and Ethane using a TCD. The final loop has an FID and detects all combustible carbon species. All of the columns are contained within the same furnace which ws held at 318 K for the first 10.5 minutes of the program, then increases to 473 K at 40 K/min. Each of the sample loops was calibrated using gases with certified compositions provided by Scotty Gases and Metro Welding Supply.

2.6 Reactor Models

In order to understand the effect of the reaction design on the yield of the desired products in an OCM reactor, a reactor model was built based on the kinetic model developed by Stansch et al [8]. In the kinetic model, Hougen-Watson type rate equations were used for the oxidation reactions to account for the inhibiting effect of oxygen and carbon dioxide on the catalyst and power-law rate equations were used for the rates of thermal dehydrogenation, steam reforming of ethylene, and the water gas shift reactions [8]. These reaction rates were combined with a mole balance for each chemical species and solved by a differential equation solver (ode15s in MATLAB) [9]. A plug flow packed bed reactor and a plug flow membrane reactor were modeled using the same code

with the exception of how oxygen was added to the reactor. The packed bed reactor model had an initial concentration of oxygen, whereas the flux of oxygen (J_{O2}) into the membrane reactor was calculated using equation 2.6. In this equation, the rate constant, k, and n were calculated from empirical data and P'' and P' are the oxygen partial pressures of the reaction side and the air side, respectively [10].

$$J_{O2} = k\left(P''^{1/n}_{O2} - P'^{1/n}_{O2}\right) \qquad (2.6)$$

2.7 Ex-situ Sample Characterization

2.7.1 Scanning Electron Microscopy

Images of the catalysts and reactors were taken using the secondary electron detector in a scanning electron microscope (SEM). In this technique, an electron gun generates electrons and accelerates them to 0.1-30 keV. The electron beam scans across the surface of the sample and the secondary electrons that reflect off the surface are collected by the detector [11]. The change in the signal from point to point is used to create the contrast in the image. The contrast in the image is therefore dependant on both the topography of the sample as well as its electrical conductivity.

The scanning electron microscopy (SEM) images included in this dissertation were collected using a Philips XL30 Scanning Electron Microscope using a working distance of 10 μm. The highest resolution of this microscope is a few nanometers at the highest accelerating voltage, however, most of the images herein were collected at an accelerating voltage of 10 keV. Higher accelerating voltages caused damage to the samples, particularly when imaging carbonaceous materials.

2.7.2 Energy Dispersive Spectroscopy

In addition to collecting images in the SEM, energy dispersive spectroscopy (EDS) was performed on many of the samples. In this technique, shown in Figure 2.7, an electron from the beam ejects a core electron from an inner orbital of an atom in the sample. When an electron from an outer orbital relaxes to fill the hole, a characteristic X-ray is released to balance the energy of the system [12]. The X-rays from the sample are collected in a detector and their energies are analyzed to determine the elemental composition of the sample. The data from this technique can be reported in a spectrum, which records the overall composition of an area, or it can be reported point by point in a line or a map. This technique is valuable for understanding the overall composition of a sample, however the overall resolution is only good to about 1 μm in the x, y, and z directions and it is not useful for understanding the composition of the surface of a sample [12].

2.7.3 X-Ray Photoelectron Spectroscopy

X-ray photoelectron spectroscopy (XPS) was used in this work to determine the elemental composition of the outer 1-10 nm of catalyst surfaces. In this technique, X-rays are directed at the sample, which cause core level electrons to be ejected from the atoms at the surface [13]. The electrons are collected by a detector, as shown in Figure 2.8. The binding energy of each electron is calculated from the kinetic energy of the electron and the photon energy of the X-rays. The binding energy can be used to determine what elements are present, and the quantity of electrons at each binding energy can then be used to determine the elemental composition of the surface [13].

The XPS system used in this study was a Kratos Axis Ultra XPS with a monochromated alumina Kα source operating at 8 mA and 14 kV. In all experiments, the charge neutralizer was used to prevent charging of the samples, and the carbon 1s peak at 284 eV was used to detect any shifting of the spectrum. The baseline for each spectrum was calculated using the Shirley algorithm, and peaks were fit and quantified using CasaXPS software.

2.7.4 X-Ray Diffraction

X-ray diffraction (XRD) was used in this work to determine the crystalline phases present in both fresh and used catalyst samples. In this technique, an X-ray beam is directed at a powder in a holder sample as the holder is rotated about an axis. When the X-rays reach the sample they can either transmit through the sample or be elastically scattered by atoms in the sample [14]. In general, the X-rays scatter in many different directions, and most of the signal is destroyed by destructive interference. However, for crystalline samples, certain angles satisfy Bragg's Law, equation 2.7. These signals add constructively and are picked up by the detector [14]. In Bragg's Law, d is the spacing between the atoms in the crystal, θ is the incident angle of the X-rays, n is any integer, and λ is the wavelength of the X-rays in the beam.

$$2dsin\theta = n\lambda \qquad (2.7)$$

The spectrum collected in an XRD experiment shows the intensity of the signal as a function of 2θ. The peaks in the spectrum give information about the location of the atoms in the sample, and therefore about the crystal structure. In this work, X-ray diffraction (XRD) was performed using a Rigaku MiniFlex spectrometer. This

instrument uses a Cu Kα X-ray source with a graphite monochromator. Data was acquired at a tube voltage and current of 40 kV and 15 mA. XRD patterns were collected with a continuous sweep from 2Θ of 20-80 at a rate of 2 2Θ/min and phases were identified using the assistance of Jade software.

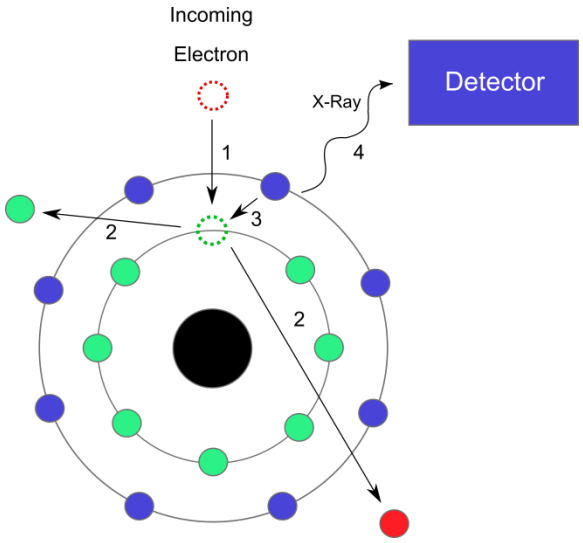

Figure 2.7: Diagram of EDS X-ray generation and collection. 1) An incoming electron strikes an atom. 2) The incoming electron and a core electron from an inner orbital are scattered. 3) An outer orbital electron relaxes to fill the hole. 4) An X-ray is released and collected by the detector

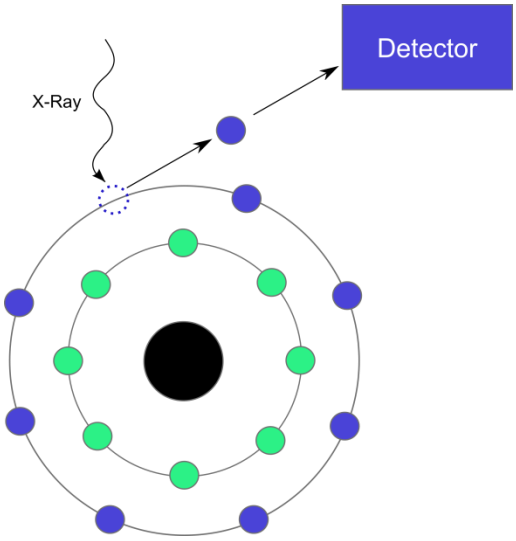

Figure 2.8: Diagram of XPS photoelectron generation and collection

2.8 References

[1] E. Nikolla, J. Schwank, S. Linic, Direct Electrochemical Oxidation of Hydrocarbon Fuels on SOFCs: Improved Carbon Tolerance of Ni Alloy Anodes, J. Electrochem. Soc. 156 (2009) B1312–B1316. doi:10.1149/1.3208060.

[2] A.J. Bard, L.R. Faulkner, Electrochemical Methods: Fundamentals and Applications, Second Edition, John Wiley & Sons, Inc, New York, 2001.

[3] B. Farrell, S. Linic, Direct electrochemical oxidation of ethanol on SOFCs: improved carbon tolerance of Ni anode by alloying, Submitted. (2015).

[4] GamryInstruments, Basics of Electrochemical Impedance Spectroscopy, (2009).

[5] Y. Leng, Performance evaluation of anode-supported solid oxide fuel cells with thin film YSZ electrolyte, Int. J. Hydrogen Energy. 29 (2004) 1025–1033. doi:10.1016/j.ijhydene.2004.01.009.

[6] E. Barsoukov, J.R. Macdonald, Impedance Spectroscopy Theory, Experiment, and Applications, Second Edition, John Wiley & Sons, Inc, Hoboken, 2005.

[7] C.F. Poole, Gas Chromatography, Elsevier Inc., New York, 2012.

[8] Z. Stansch, L. Mleczko, M. Baerns, Comprehensive Kinetics of Oxidative Coupling of Methane over the La_2O_3/CaO Catalyst, Ind. Eng. Chem. Res. 36 (1997) 2568–2579. doi:10.1021/ie960562k.

[9] H.S. Fogler, Elements of Chemical Reaction Engineering, Fourth Edition, Pearson Education, Inc, Upper Saddle River, 2006.

[10] F.T. Akin, J.Y.S. Lin, Oxygen permeation through oxygen ionic or mixed-conducting ceramic membranes with chemical reactions, J. Memb. Sci. 231 (2004) 133–146. doi:10.1016/j.memsci.2003.11.012.

[11] J.I. Goldstein, D.E. Newbury, P. Echlin, D.C. Joy, C.E. Lyman, E. Lifshin, et al., Scanning Electron Microscopy and X-Ray Microanalysis, Third Edition, Springer Science + Business Media, New York, 2003.

[12] J.J. Friel, X-Ray and Image Analysis in Electron Micrsocopy, Second Edition, Princeton Gamma-Tech, Princeton, 2003.

[13] P. van der Heide, X-Ray Photoelectron Spectroscopy: An Introduction to Principles and Practices, John Wiley & Sons, Inc, Hoboken, 2012.

[14] O.H. Seeck, X-Ray Diffraction: Modern Experimental Techniques, Pan Stanford Publishing Pte. Ltd., 2015.

Chapter 3

Direct electrochemical oxidation of ethanol on SOFCs: improved carbon tolerance of Ni anode by alloying[1]

3.1 Summary

Solid oxide fuel cells (SOFCs) are electrochemical devices that convert chemical energy in fuels into electrical energy through an electrochemical oxidation process. This technology is attractive since SOFCs can in principle utilize a range of combustible fuels including hydrogen, carbon monoxide, and hydrocarbons offering higher efficiencies than conventional electricity generators with limited emission of a number of common air pollutants such as NO_x and SO_x. The environmental efficiency of SOFC devices can further be improved by utilizing fuels that are more carbon-neutral (e.g., biofuels such as ethanol) than conventional fossil fuels. One of the problems with employing oxygenated liquid biofuels is that conventional Ni anode electro-catalysts deactivate due to carbon deposition on the surface of the anode during the process of electocatalytic fuel oxidation. In this chapter, the stability of Ni SOFC anode electrocatalysts during electrochemical oxidation of ethanol is significantly improved when a small amount of Sn is introduced in the electrocatalyst design. The improvement in the stability is manifested in a more stable operation and higher kinetic currents of Sn/Ni compared to Ni electrodes under identical conditions with ethanol fuel. We discuss

[1] The data included in this chapter has been included in the following publication:
Farrell, B., Linic, S. Direct electrochemical oxidation of ethanol on SOFCs: improved carbon tolerance of Ni anode by alloying. Applied Catalysis B: Environmental. Accepted.

the underlying molecular mechanisms responsible for the enhanced stability of the anodes and propose a number of guiding principles for the design of carbon-tolerant anodes for oxidation of oxygenated hydrocarbons.

3.2 Introduction

Solid oxide fuel cells (SOFCs) are electrochemical devices that convert the chemical energy in fuels into electrical energy through an electrochemical oxidation process. SOFCs operate at temperatures ranging from ~ 800 to 1300 K. This technology is attractive since SOFCs can in principle utilize a range of combustible fuels including hydrogen, carbon monoxide, hydrocarbons, and oxygenated hydrocarbons, offering higher efficiencies than conventional electricity generators [1,2] with little to no emission of air pollutants [3] such as NO_x, and SO_x. Although SOFCs still emit CO_2 when operating on hydrocarbon fuels, the CO_2 effluent is physically separated from the air side of the fuel cell, and it must only be separated from water and excess fuel [4,5]. This ease of separation makes the technology compatible with the process of CO_2 capture and sequestration. The carbon footprint of SOFC devices can also be lowered by utilizing fuels that are more carbon-neutral (e.g., biofuels) than conventional fossil fuels. When made from biomass, fuels such as ethanol and butanol have greenhouse gas reductions of up to 60% compared to petroleum-based fuels [6,7]. These fuels are liquid at standard conditions and therefore also have additional benefits over gaseous fuels including high specific energy density and ease of storage and transport.

SOFCs can in principle directly utilize hydrocarbon and oxygenated hydrocarbon fuels, including ethanol and butanol which can be produced from biomass, without any pre-reforming of the fuel. While the direct operation simplifies the design of the SOFC

system, it has been demonstrated that the stability of these cells is compromised due to high rates of carbon deposition on the conventional anode electrocatalysts, which contain nanometer to micrometer sized particles of Ni [1,8–13]. The carbon deposits take the form of graphitic carbon or carbon filaments. These deposits eventually physically degrade the structure of the Ni anode [14–16]. It has been reported that carbon deposition is even more dramatic for oxygenated hydrocarbons compared to alkanes. It has been argued that oxygenated fuels undergo gas phase pyrolysis at temperatures relevant to operating SOFCs [17,18]. During the pyrolysis process many different compounds are formed, including acetylene and ethylene which are very potent in forming carbon deposits on the surface of the anode [18,19].

Several strategies can be employed to inhibit the formation of carbon deposits on SOFC anodes. One strategy is to add a pre-reformer which converts hydrocarbon fuels to carbon monoxide and hydrogen, which are then used as the fuel for SOFC [20,21]. These additions add complexity to the fuel cell system. Furthermore, an incomplete reformation of the fuel can lead to the leakage of hydrocarbon fuel to the cell and carbon-induced degradation of the cell. Another strategy is to add an oxidant, such as water or air, to the fuel to decrease the carbon to oxygen ratio on the anode and in doing so avoid operation at the conditions where carbon deposition is thermodynamically favored [19,22,23]. The problem with this approach is that in fuel cell systems it is often the kinetics of the carbon forming and degrading reactions that governs the stability, and carbon-induced anode deactivation has been observed even in systems where solid carbon is not the most thermodynamically favorable product [9]. Another issue with adding oxidants to the fuel is that it decreases the efficiency of the device by lowering the open circuit potential of

the fuel cell. Furthermore, it has also been reported that water vapor can lead to sintering of the nickel in the anode lowering the rate of current generation (and therefore the power output) and decreasing the stability of the Ni anode [1]. A third strategy is to change the catalyst in the anode from Ni to a material that is less prone to carbon-induced deactivation. One approach is to utilize a composite containing Cu and CeO_2. It has been proposed that in these systems Cu functions as the electron conducting phase, while CeO_2 is the main catalyst for the conversion of hydrocarbons [8]. These systems show lower carbon deposit formation rates compared to the Ni anodes; however, they operate at lower temperatures which are required to prevent melting and sintering of the copper phase. Operating at lower temperatures offers some benefits since there are a larger number of the balance of plant materials that are stable under lower temperature conditions. However, the lower temperature operation decreases the reaction rates on the anode and the cathode sides as well as the flux of O^{2-} through the electrolyte. Another approach relies on the synthesis of Ni alloy electro-catalysts that exhibit physical properties similar to monometallic Ni while exhibiting improved carbon tolerance. For example, we have previously shown that the addition of a small amount of Sn to Ni anode catalysts creates a Sn/Ni surface alloy which showed improved tolerance to the carbon-induced deactivation with methane and isooctane fuels compared to fuel cells with monometallic Ni anodes [14,24,25]. These results have been supported by recent reports by Yoon and Kan and their respective coworkers [26,27].

In this chapter, we show that Ni electro-catalysts doped with a small amount of Sn (nominally 1% with respect to Ni) also show improved tolerance in electro-catalytic oxidation of oxygenated hydrocarbons (e.g., ethanol) compared to monometallic Ni

anodes. Our conclusions are based on experimental observations that Sn doped Ni/YSZ anode fuel cells show less physical damage, less carbon deposition in the anode, and more stable electrochemical performance over time when compared to monometallic Ni anode fuel cells in electro-catalytic oxidation of ethanol. We note that oxygenated hydrocarbons such as ethanol are readily produced from biomass. In addition to reporting our experimental findings our results shed some light on the design principles that should guide the development of carbon-resistant SOFC anodes.

3.3 Experimental

3.3.1 Electrochemical Measurements

Fuel cells used in this study were anode supported button cells with cathode areas of ~ 0.15 cm^2. The fuel cells were attached through the anode side directly onto the end of an alumina tube using alumina paste (Ceramabond 552), and fuel was fed via an inner tube perpendicular to the anode surface at atmospheric pressure. Gases were fed using either mass flow controllers or rotometers, and liquid fuels were fed using a bubbler at room temperature entrained by argon. Feed lines were heated to at least 373 K to avoid condensation of liquid fuels. The fuel cell cathode on the opposite side was open to the atmosphere. Electrochemical measurements were performed using a PARSTAT 2273 (Princeton Applied Research) and included linear sweep voltammetry, electrochemical impedance spectroscopy, and constant voltage stability tests.

3.3.2 Catalyst Characterization

3.3.2.1 Scanning Electron Microscopy

Electron micrographs were obtained using a Philips XL30FEG scanning electron microscope (SEM) which has a resolution of a few nanometers. We performed elemental

analysis on the samples using a Si-Li solid state x-ray detector attached to this microscope which provided energy dispersive x-ray spectroscopy (EDS) data. Both the images and EDS data were collected with an accelerating voltage of 10 kV and a working distance of 10 mm. In all SEM experiments, the anode pellets were fractured down the middle of the cathode in order to obtain cross sections of the active fuel cell area.

3.3.2.2 X-ray Photoelectron Spectroscopy

X-ray photoelectron spectroscopy (XPS) data was taken using a Kratos Axis Ultra XPS with a monochromated alumina Kα source operating at 8 mA and 14 kV. Experiments were performed on fuel cell anode catalysts to determine the relative concentration of Sn and Ni in fresh and used materials. In all experiments, the charge neutralizer was used to prevent charging of the samples, and the carbon 1s peak at 284 eV was used to detect any shifting of the spectrum. The baseline for each spectrum was calculated using the Shirley algorithm, and peaks were fit and quantified for Ni, NiO and Sn using CasaXPS software.

3.3.3 Synthesis

Figure 3.1 shows an SEM image of the cross section of a typical fuel cell, EDS mapping of the fuel cell anode, and the experimental setup used in this study. The planar fuel cell pellets were fabricated using yttria stabilized zirconia (YSZ) (8%, Tosoh), nickel oxide (NiO) (Alfa Aesar), and graphite (300 mesh, Alfa Aesar) powders in a weight ratio of 1:1:0.6. The powders were combined and ball-milled in de-ionized water for 24 hours, and the resulting slurry was then dried and sifted. The powder was then pressed into 15 mm diameter pellets with a thickness of about 1 mm. The pellets were pre-fired at 1273 K for 4 hours (2 K/min) to remove the carbon pore former. Solutions of $SnCl_2*2H_2O$ in

ethanol were added to the NiO/YSZ pellets using the incipient wetness technique to synthesize Sn/Ni anodes with a nominal Ni:Sn metal ratio of 100:1. The YSZ electrolyte was added drop wise to the surface of the pellets, suspended in a solution of ethanol and Ethocel-300 (Dow Chemical) and sintered at 1723K for 4 hours (1 K/min). The process resulted in the formation of the anode and electrolyte layers shown in Figure 3.1a. The electrolyte layer of the fuel cells was 15-20 μm thick, while the anode layers were typically about 500 μm thick consisting of a mixture of irregularly shaped NiO (or NiO/Sn for the alloys) and YSZ particles which range from approximately 0.5 μm to 5 μm in diameter according to SEM images and EDS mapping shown in Figure 3.1b. Two layers of cathode material were painted on the surface of the YSZ electrolyte in two steps using slurries ball-milled in ethanol for 24 hours. The first layer had a weight ratio of 1:1 YSZ and lanthanum strontium manganite (LSM) ($La_{0.8}Sr_{0.2}Mn_{0.98}$, Praxair), and the second layer had a weight ratio of 0.25:1 graphite:LSM. The layers were sintered at 673 K and 1423 K for 2 hours, respectively (2 K/min) creating a cathode layer about 50 μm thick. Gold mesh current collectors were secured to the cathode side using silver paste (Alfa Aesar), however gold mesh was not used on the anode side. Two gold wires were secured to each electrode using silver paste. The cells were secured to an alumina tube using alumina paste (Ceramabond 552) and placed in a furnace as shown in Figure 3.1c. After curing the alumina paste, the temperature was ramped 0.8 K/min to 973 K in air, the system purged with Ar, and switched to hydrogen to reduce the NiO in the anode for 16 hours. The cathode was left open to stagnant air during this process. The temperature was then brought up to the final fuel cell operating temperature.

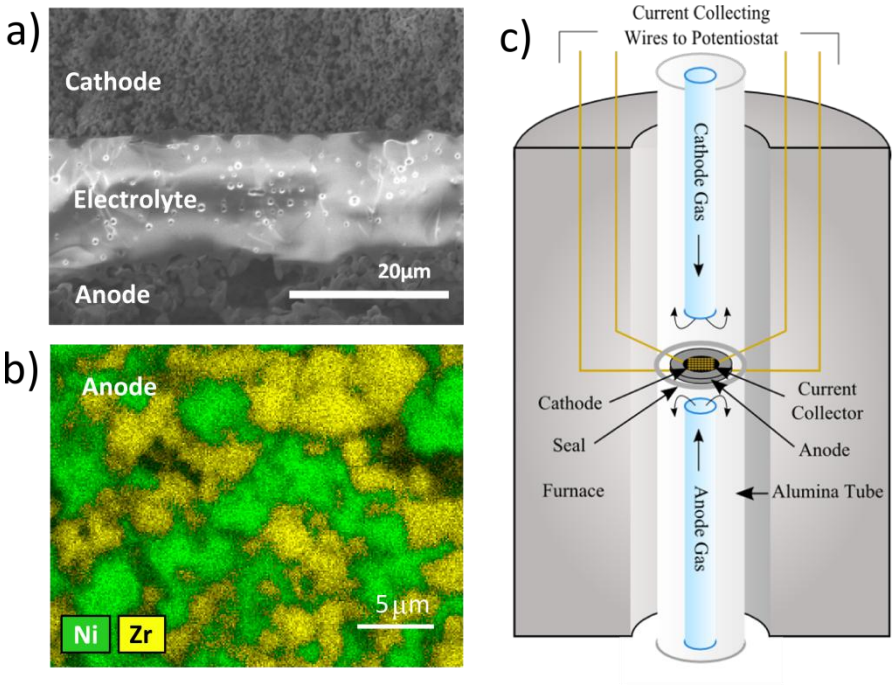

Figure 3.1: a) SEM image of the cross-section of the electrolyte of a fuel cell used in this study b) Energy dispersive spectroscopy of the anode structure showing areas of nickel and zirconia b) Diagram of the electrochemical testing setup.

3.4 Results

3.4.1 Electrochemical Testing

Figure 3.2 shows I-V and power curve data for monometallic Ni and 1%Sn/Ni cells after 10 minutes and 18-20 hours operation on ethanol. In all experiments, fuel cells were first run on hydrogen at 120 sccm and a constant voltage of 0.6 V (voltage difference between anode and cathode) for 4-6 hours. During this time, current density typically increased due to the activation of the cathode layer [28]. This operation on hydrogen allowed us to establish baseline activity for the fuel cell and to stabilize the cell operation. After this initial period, the fuel was switched from H_2 to 30 sccm argon bubbled through ethanol at room temperature (296 K). These conditions yield an ethanol vapor flow of approximately 2.2 sccm. The reported I-V curves and power data were taken by taking the cell to the open circuit voltage (OCV) and stepping down in voltage by 20 mV increments every 10 seconds from the OCV to 0.1 V. In all fuel cells, the initial OCV on hydrogen was between 1.05 and 1.08 V, which is close to the value predicted by the Nernst equation (~1.1 V). When the fuel was switched to ethanol, the OCV decreased to 1.01-1.03 V. This decrease was expected, because the theoretical OCV for the conditions of our system was ~1.04 V.

Figure 3.2a shows I-V and power curve data for a monometallic Ni cell. The data suggests ethanol-induced changes in the performance of the cell over time. There are three observable differences in the data collected after 10 minutes and 18 hours of operation: (i) at high voltages, close to the equilibrium voltage, a lower current is measured on the Ni cell operated for 18 hours compared to the same cell operated for 10 minutes. This change in the I-V characteristics suggests ethanol-induced polarization

losses, (ii) at the intermediate voltages (0.8 V-0.5 V), the slope of the I-V curve is smaller for the cell operated for 18 hours compared to the same cell operated for 10 minutes, suggesting that the ohmic losses are smaller for the cell operated for longer time on ethanol, (iii) at low voltage, the cell operated for 18 hours exhibits higher losses than the same cell operated for 10 minutes suggesting lower fuel mass transport rates after exposure to ethanol. All the observed changes in the I-V characteristics of the Ni cell can be explained by buildup of carbon deposits within the Ni anode. Carbon buildup lowers the concentration of active centers on Ni electrodes (thereby lowering the kinetic current measured at high voltage), improves the electronic contacts between neighboring Ni particles (therefore lowering ohmic resistance) [29], and lowers the rates of mass transport of the reactants by decreasing the porosity of the anode assembly. Figure 3.2b shows the data for the 1%Sn/Ni cell operated under identical conditions as the Ni cell using ethanol fuel. The data show no significant changes in the performance of the cell over the 20 hours of ethanol operation.

Figure 3.3 shows I-V and power curve data collected for the similar monometallic Ni and 1%Sn/Ni cells while operating on hydrogen before and after exposure to ethanol, along with a control experiment where a monometallic Ni cell was operated only with hydrogen (this cell was never exposed to ethanol). Figure 3.3a shows the I-V and power data from the control experiment where only hydrogen was used. The data show very little difference for data sets taken after 8 and 28 hours of operation on hydrogen, suggesting that the fuel cell is stable over this period of time. Figure 3.3b shows the I-V and power data for a monometallic Ni cell operated on hydrogen after the cell was exposed to 6 hrs of steady hydrogen operation (circles) and after an additional 18 hours

of ethanol operation (triangles). The ethanol-induced changes in the hydrogen I-V data include a decrease in the current at high voltages and an increase in current at intermediate voltages. These changes are consistent to those reported in Figure 3.2a, except that there are no significant changes at low voltage due to mass transport of the fuel. This is likely because hydrogen was fed in higher concentration and at a higher flow rate than ethanol which allowed for higher rates of hydrogen diffusion through the porous anode network. In addition, hydrogen is geometrically smaller than ethanol and its diffusion coefficient is inherently higher than that of ethanol. Figure 3.3c shows the I-V and power data for a 1%Sn/Ni cell operated on hydrogen after the cell was exposed to 4 hrs of steady hydrogen consumption (circles) and after an additional 20 hours of ethanol exposure. In contrast to Figure 3.3b, the data in Figure 3.3c show that the 1% Sn/Ni cell is significantly more stable than the cell containing a monometallic Ni anode.

To further analyze electrochemical characteristics of the cells containing Ni and Sn/Ni anodes, we preformed potentiostatic impedance spectroscopy measurements. Figure 3.4 shows Nyquist plots for the Ni cell operated only on hydrogen fuel as well as for the Ni and 1% Sn/Ni fuel cells operating on ethanol after 10 minutes and 18-20 hours of operation at 0.6 V. The impedance measurements were collected at OCV with the voltage perturbation amplitude of 10 mV at frequencies ranging from 100 kHz to 100 mHz. In each Nyquist plot, there are two points where the data intercept the real axis (x axis). One point is at high frequency and low Zreal. This high frequency resistance is associated with ohmic losses, and it is attributed mainly to the electrolyte and the conductivity of the electrodes. The second x-axis intercept occurs at lower frequency and high Zreal. The x axis distance between these two x-axis intercept points is commonly

referred to as the polarization resistance. It is attributed to polarization processes at the electrodes. We note that because the cells are anode supported with very thin electrolytes, no attempt was made to include a reference electrode and the polarization resistance contributions from the anode and cathode cannot be rigorously distinguished. We note that we do not expect significantly different changes on the cathodes for different cells since all the cells were exposed to air at identical conditions. Therefore, most of the differences in the changes in the polarization behavior of our devices can be attributed to the cell-specific changes in the anodes.

We first analyze the high frequency impedance (due to ohmic losses). We measure this impedance to be between 0.12 and 0.18 $\Omega*cm^2$ for all tested cells. These values are consistent with the theoretical resistance of YSZ, which for the YSZ electrolyte thickness of 10-20 μm used in our experiments is predicted to be 0.08-0.16 $\Omega*cm^2$ at 1013 K. The ohmic resistance decreases slightly over time for all cells which may be due to sintering of the electrode particles which could increase the electrode conductivity and connection to the electrolyte. We note that larger decreases in the ohmic resistance are seen for the monometallic Ni cell operating on ethanol where the resistance decreases by about 10-14 % after exposure to ethanol, as opposed to only 0-5 % for the 1%Sn/Ni cell. This is most likely due to the carbon-induced increase in the electron conductivity on the anode side. Similar observations were reported by McIntosh et al. who showed large decreases in the ohmic resistance of their cells after exposure to carbon fuels, which they attributed to carbon increasing the conductivity of the anode as well as connecting previously isolated sections of the catalyst [29].

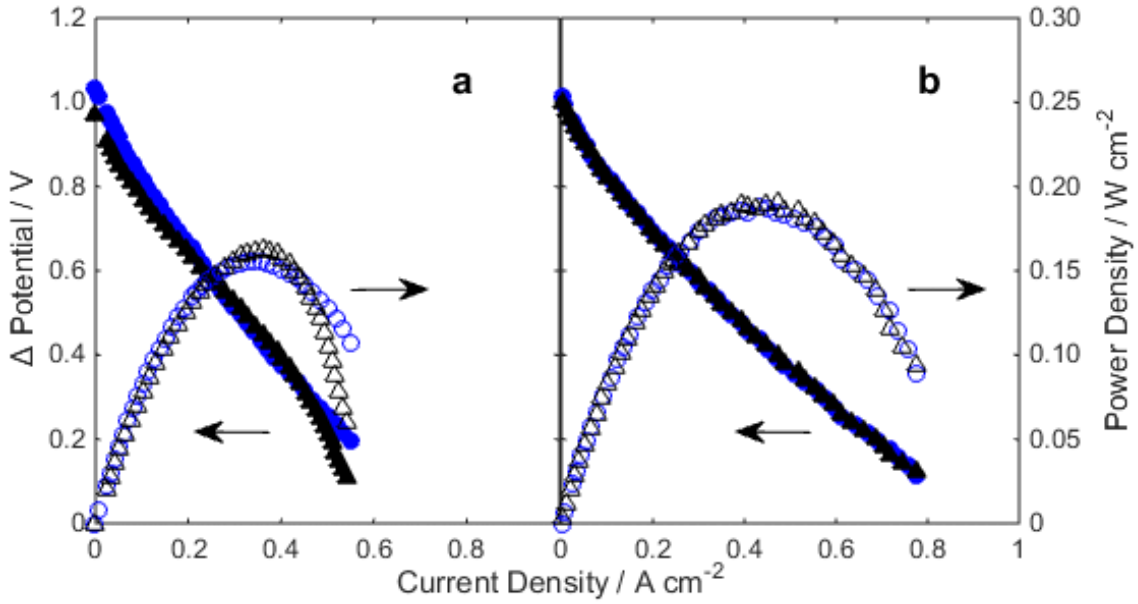

Figure 3.2: I-V (solid markers) and power density (open markers) curves for fuel cells operated on 30 sccm Ar bubbled through ethanol at 296 K at 1013 K (a) monometallic Ni anode cell: circles are data collected after 10 min of operation on ethanol, triangles are data collected after 18 hr operation on ethanol at 0.6 V (b) 1%Sn/Ni anode cell: circles are data collected after 10 min of operation on ethanol, triangles are data collected after 20 hr operation on ethanol at 0.6 V.

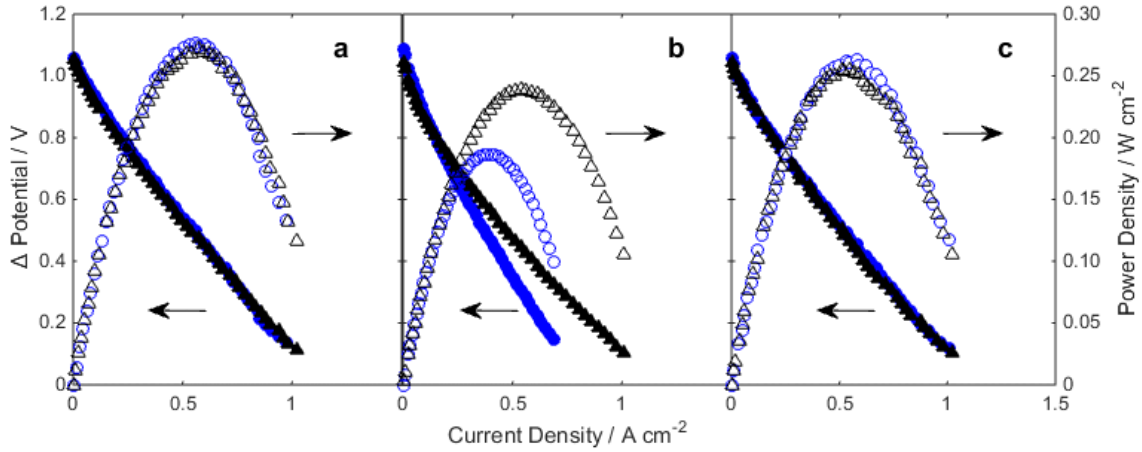

Figure 3.3: I-V (solid markers) and power density (open markers) curves for fuel cells operated on 120 sccm hydrogen at 1013 K (a) Ni cell operated only on hydrogen: circles are data collected after 8 hr at 0.6 V on hydrogen, triangles are data collected after 28 hr at 0.6 V on hydrogen. (b) Ni cell operated on hydrogen: circles are data collected after 6 hr at 0.6 V on hydrogen, triangles are data collected after 18 hr at 0.6 V on ethanol. (c) 1%Sn/Ni cell operated on hydrogen: circles are data collected after 4 hr at 0.6 V on hydrogen, triangles are data collected after 20 hr at 0.6 V on ethanol.

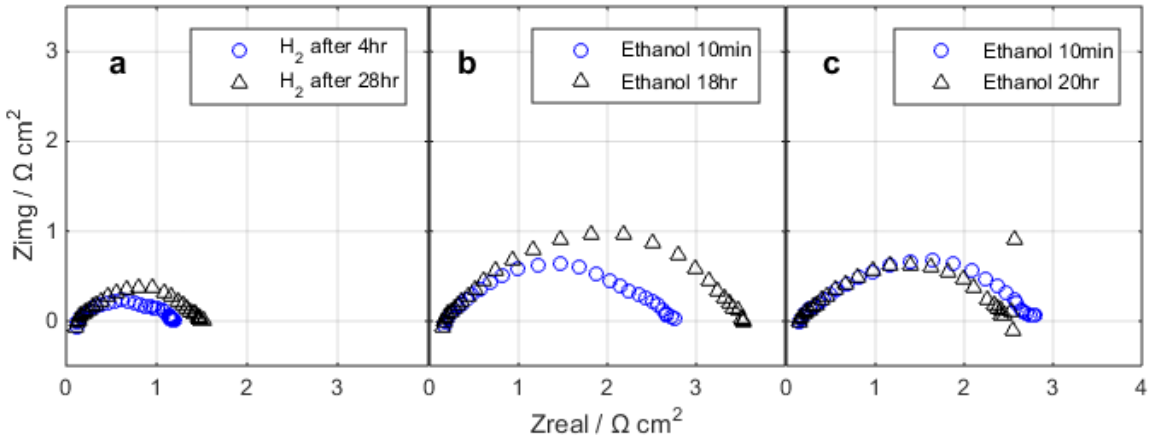

Figure 3.4: Impedance spectroscopy taken at OCV and 1013 K. (a) Ni cell operated on only hydrogen: circles are data collected after 4 hr at 0.6 V, triangles are data collected after 28 hr at 0.6 V (b) Ni cell operated on ethanol: circles are data collected after 10 min at 0.6 V, triangles are data collected after 18 hr at 0.6 V. (c) 1%Sn/Ni cell operated on ethanol: circles are data collected after 10 min at 0.6 V, triangles are data collected after 20 hr at 0.6 V.

The data in Figure 3.4 also show changes in the polarization resistance over time. Figure 3.4a shows that the polarization resistance increased slightly over time for the monometallic Ni cells operated on hydrogen only. These increases are likely due to changes in the electrodes over time due to sintering on Ni particles, which causes a decrease in the catalytic surface area of the electrode. Figure 3.4b shows that the polarization resistance also increases for the monometallic Ni cell operated on ethanol; however, this increase in the polarization resistance is much larger than the increase in Figure 3.4a for the Ni cell that operated on hydrogen. The additional increase in the resistance is likely caused by carbon blocking active sites on the Ni anode surface. Figure 3.4c shows that contrary to Ni, the polarization resistance decreased in the 1%Sn/Ni cell. This small decrease in the polarization resistance is likely caused by either a small loss or rearrangement of the Sn on the surface of the Ni. We have previously reported that while Sn aids the stability of the Ni electrodes, it also leads to a decrease in the inherent electrochemical activity of the Ni electro-catalysts. In Section 3.2 below we report XPS data which shows that some Sn has been lost from the surface of the anode particles after operation on ethanol fuel. We note that impedance spectroscopy measurements reported by Kan et al. on similar Sn/Ni systems in the electrochemical oxidation of alkanes showed a similar effect, and they also reported a small loss of Sn (~5%) from their system as measured by inductively coupled plasmon spectrometry (ICP) [27]. The lack of increase in the polarization resistance for the Sn/Ni anodes operated in ethanol is consistent with the observation that the rate of carbon deposition on the 1%Sn/Ni electrodes is significantly lower than on the Ni electrodes.

3.4.2 Ex-situ Anode Characterization

In addition to electrochemical testing, physical and chemical changes occurring in the SOFC anodes were analyzed ex-situ, using x-ray photoelectron spectroscopy (XPS) and scanning electron microscopy (SEM). Figure 3.5 shows XPS data for the Ni 2p edge (Figure 3.5a) and the Sn 3d edge (Figure 3.5b) for three anode samples. As shown in the figure, the XPS data can be deconvoluted in terms of Ni, NiO, and Sn. The top spectra are data from a 1%Sn/Ni anode which was reduced in hydrogen at 973 K following the procedure identical to the one used before electrochemical testing. This anode was never operated as a fuel cell, and therefore is representative of the anode composition before exposure to ethanol. The middle spectra are data from the 1%Sn/Ni anode operated on ethanol for 20 hours at 0.6 V and 1013 K, and the bottom spectra are data from the monometallic Ni anode that was operated on hydrogen at 0.6 V and 1013 K for 28 hours. The Ni 2p data show that all samples contained a mixture of Ni and NiO surface domains. Sn 3d peaks were observed for the two 1%Sn/Ni anodes, however the Sn $3d_{3/2}$ peak is partially obstructed by an intense Auger Na KLL peak (this is an impurity due to the sample and holder handling). Further analysis of the XPS spectra aimed at quantifying the relative concentration of Sn and Ni at the surface of the electro-catalytic particles demonstrated that for the nominal, bulk Sn loading of 1 %, the surface concentration of Sn was approximately 3 % (this is the concentration detected by XPS). This enrichment of Sn at the surface has been observed before and it is a consequence of the thermodynamically preferred Sn enrichment at the surface layers of Ni particles[30]. The analysis also showed that the Sn content in the surface of the particles was depleted to 1.8% after operation on ethanol for 20 h.

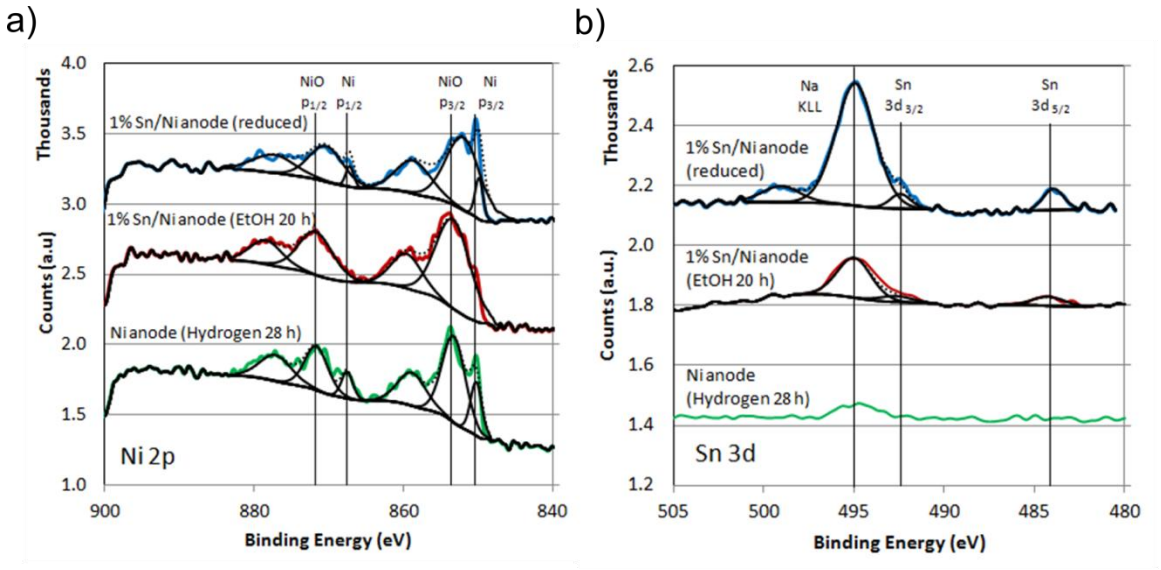

Figure 3.5: XPS data and curve fitting for a) the Ni 2p edge and b) the Sn 3d edge

To further investigate the composition of the material, the used cells were fractured and the cross-sections were imaged using SEM with an EDS detector. Figure 3.6 shows SEM images and corresponding EDS maps of Ni and 1%Sn/Ni fuel cells obtained for the regions ~ 100 μm from the outer edge of the anode (~400 μm from the electrolyte). Figure 3.6a shows an SEM image of a Ni/YSZ anode that has operated on hydrogen for 28 hours at 0.6 V. Figure 3.6b shows the corresponding EDS map. These images provide a baseline to compare to the cells run on ethanol. The Ni particles obtained after the cell was operated on hydrogen are smooth and the map shows only large areas occupied by Ni and Zr. Figure 3.6c and 3.6d show the SEM image and EDS map for the Ni cell after operation on ethanol for 18 hours at 0.6 V. The SEM image shows many regions where the Ni and YSZ particles appear rough and broken apart. These regions correspond to areas occupied by carbon in the EDS map. Figure 3.6e and 3.6f show images for the 1%Sn/Ni cell after operation on ethanol for 20 hours at 0.6 V. The SEM image shows mainly smooth particles, and the EDS map indicates only a few small areas of carbon buildup.

Although the SEM images provide good visualization of the degradation and carbon deposition on the anode surface, SEM can only provide images of small areas which may not be representative of the overall anode structure. Therefore, in addition to the imaging and mapping of the carbon deposits within the fuel cells, we have also used EDS to quantify where the carbon deposits are concentrated within the anode. Figure 3.7 shows the ratio of the C to Ni EDS signals (C/Ni peak ratio) obtained at several distances from the electrolyte for fuel cells operating at several different conditions. The C/Ni peak ratios were averaged over several points along the electrolyte to give a better indication

of the carbon deposition over a larger fuel cell area. Spectra were taken approximately every 50 μm along lines orthogonal to the electrolyte. A fuel cell operated on only hydrogen is included with the data to indicate a baseline for comparison of C/Ni peak ratios of the other fuel cells. In the figure, a C/Ni peak ratio larger than the baseline indicates carbon deposition. Overall, three major trends can be observed from Figure 3.7. First, carbon deposition is most severe at the outer edge of the anode, furthest from the electrolyte. This is shown in Figure 3.7 as an increase in C/Ni peak ratios as distance from the electrolyte increases. This is not surprising since the outer edge of the anode is exposed to the highest carbon concentration from the fuel, and the lowest concentration of oxygen from the electrolyte, causing higher carbon deposition on the outer edge of the anode. The second trend is that the operating voltage has a large effect on the carbon deposition on the anode surface. Figure 3.7 shows that after cell operation on ethanol at 0.5 V for 18 hours, there is very little carbon detected. Similarly, even smaller amounts of carbon were detected in the 1%Sn/Ni cell after 18 hours of exposure to ethanol at 0.5 V. At 0.6 V, there is carbon detected at the outer edge of both the monometallic and 1%Sn/Ni cells. This is also not surprising since a lower ΔV results in higher current which means that the rate of the transport of oxygen ions through the electrolyte is higher, indicating that effective O/C ratio is higher at lower ΔV. Finally, for all tested cells, the cells that employed the 1%Sn/Ni anodes exhibited less carbon deposition than the cell with monometallic Ni anodes operating at identical conditions. This is most apparent in the data from the cells operated at 0.6 V, where the 1%Sn/Ni cell only has a relatively small amount of carbon detected at 50 μm from its outer edge. In contrast, for

the Ni cell operating at similar conditions, carbon is detected 200 μm from the outer edge of the cell, with very large amounts of carbon near the outer edge.

3.5 Discussion

The data discussed above showed that the introduction of small amounts of Sn to Ni anode electro-catalysts enhances the stability of the anode to carbon-induced deactivation over a range of operating conditions when oxygenated hydrocarbons such as ethanol are employed as fuels. This was demonstrated through the observations that after exposure to ethanol, the cells fabricated with monometallic Ni anodes showed decreased current densities at high voltages, and increased polarization resistance at OCV. Both of these effects are likely due to carbon blocking of the active sites at the surface of the electro-catalyst particles. We have previously reported similar findings for the Ni-based anodes operating on methane and iso-octane [14]. These previous studies included a detailed characterization of the anode electro-catalysts which suggested that Sn atoms preferentially segregate to the under-coordinated sites on the surface of Ni electro-catalyst nanoparticles, eliminating nucleation sites for carbon growth [11,31]. Furthermore, it was postulated that Sn atoms break up the ensembles of the surface Ni atoms that are required for the formation of extended carbon planar networks and filaments [25,31]. Since the Ni and Sn/Ni anode electro-catalysts employed in this study are identical to those used previously, we postulate that the underlying molecular mechanisms associated with the observed extended lifetime of the Sn/Ni anode electro-catalysts are identical, and that they include the Sn-induced changes in the carbon chemistry of Ni surfaces [14,24,25,30,31].

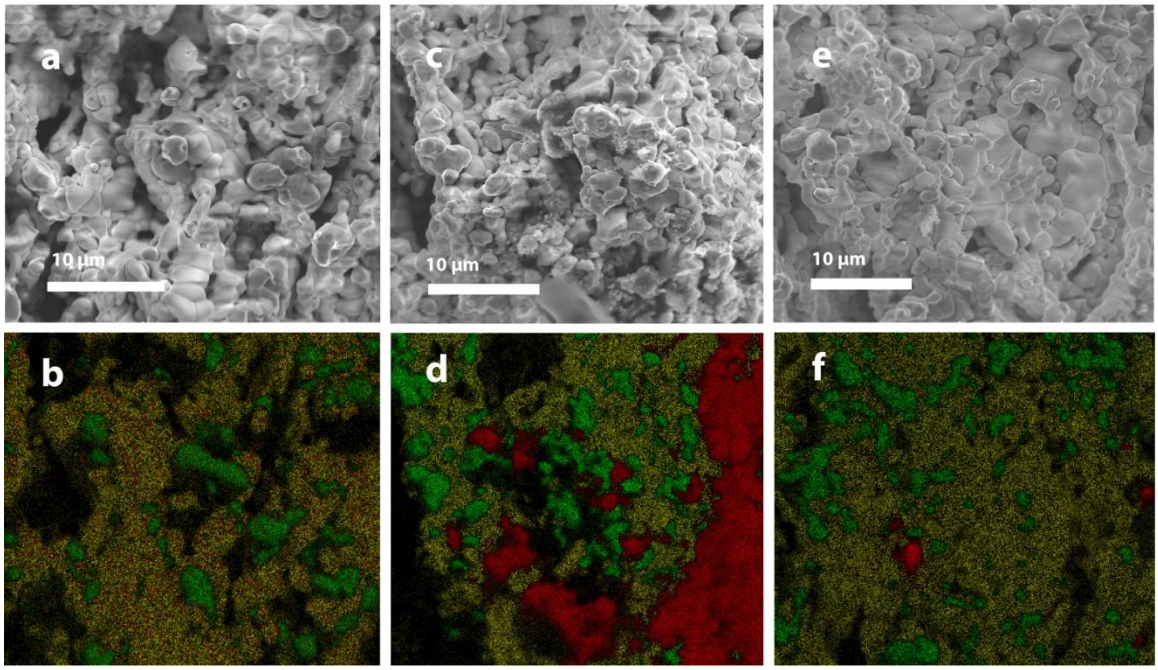

Figure 3.6: SEM images (top) with EDS maps (bottom) taken 100 µm from the outside of the anode showing Ni (green), Zr (yellow) and C (red) for (a, b) Ni anode fuel cell operated on only H_2 for 28 hr(c, d) Ni anode fuel cell operated on ethanol at 0.6 V for 18 hr (e, f) 1%Sn/Ni anode fuel cell operated on ethanol at 0.6 V for 20 hr.

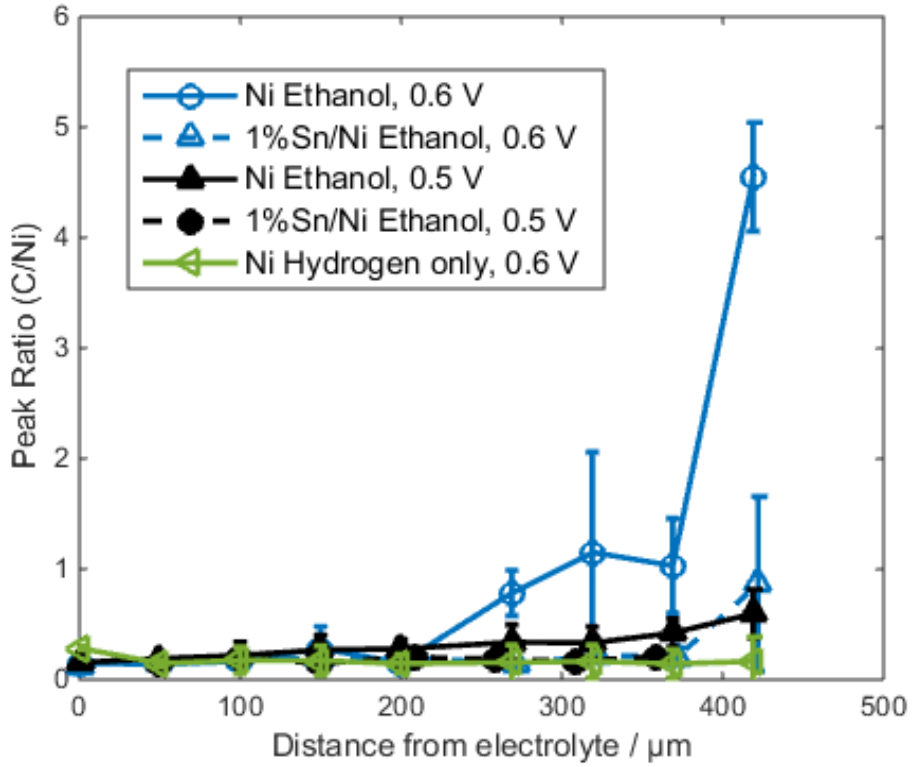

Figure 3.7: EDS C/Ni peak ratios for fuel cells as a function of distance from the electrolyte. The final measurement for each cell is taken 50 µm from the outer edge of the anode.

The studies above also shed light on a few critical guiding principles that need to be considered when designing SOFC systems that utilize hydrocarbons or bio-derived oxygenated hydrocarbons fuels. First, it has to be recognized that there are many chemical and electro-chemical reactions that are taking place in the anode compartment when these fuels are fed directly to the cell. The nature of these reactions and the regions of anode compartments where they are dominant are heavily influenced by the local oxygen (including O^{2-} ions) to fuel ratios. For example, at the three-phase-boundary (TPB), where electrolyte and anode electro-catalysts are in contact with each other, due to high activity of oxygen ions (which is the result of high transport rates through the electrolyte), deep and partial electrochemical oxidation reactions will dominate. These reactions are not the source of the formation of carbon deposits, as illustrated in Figure 3.7. On the other hand in the regions away from the TPB, steam and dry reforming of the fuel that involve water and CO_2 respectively take place. We note that water and CO_2 are produced at the TPB boundary during the electrochemical oxidation process. These reforming reactions could result in the formation of carbon deposits. In addition, even further from the electrolyte where oxygen content is depleted even more, hydrocarbon pyrolysis reactions take place. For oxygenated hydrocarbons such as ethanol at the operating temperature of 1013 K, the process of pyrolysis results in the formation of CO, CO_2, CH_4, ethylene, ethane, and hydrogen. While some of these compounds are excellent fuels for SOFCs, others are very potent in forming carbon deposits in the anode. For example, ethylene has been shown to rapidly build graphitic carbon deposits on Ni catalyst surfaces.[15] This is supported by Figure 3.7 which shows that the extent of carbon deposition increases for the regions farther away from the electrolyte.

If the process of carbon deposition is to be limited, it is imperative to design anodes that operate with high oxygen to carbon ratios. Therefore, thin membranes that are excellent ion conductors are preferred. Furthermore, since the activity of oxygen is the highest at the TPB, it is important to increase the ratio of the TPB surface to the volume of the anode compartment. Even if these design principles are embraced, there will be reforming and pyrolysis reactions taking place at the elevated SOFC operating temperatures. As discussed above, these reactions can lead to rapid degradation of conventional Ni anode electro-catalysts. In this case, significant reductions in the rates of formation of carbon deposits can be achieved by designing electro-catalysts, such as the above discussed Sn/Ni alloy, that have lower propensity to activate the formation of carbon deposits compared to monometallic Ni without significant reduction of the reaction rates. It is important to point out that even when these catalysts are employed, if the local oxygen to carbon ratio is exceedingly low (below the stoichiometric limit for the formation of CO), the carbon deposition cannot be prevented and the cell will eventually accumulate carbon and deactivate.

3.6 Conclusions

We have demonstrated in this chapter that carbon deposition catalyzed on monometallic Ni in the process of electrochemical oxidation of oxygenated hydrocarbon fuels (e.g. ethanol) can be decreased by Ni alloying with small amounts of Sn. In SOFCs fabricated using monometallic Ni, carbon deposition resulted in physical and electrochemical changes to the Ni anode. In contrast, Sn/Ni alloy anodes inhibited the formation of carbon-induced degradation catalyzed by Ni, resulting in smaller electrochemical changes over time and less carbon deposition. Additionally, we have

shown that carbon deposition is affected by the location of the catalyst in the anode as well as the operating voltage, which are both factors that affect the local C/O ratio on the catalyst surface. Overall our results indicate that the catalyst surface chemistry and local C/O ratios are both important factors that must be considered in the design of fuel cell anode catalysts operating on oxygenated hydrocarbon fuels.

3.7 References

[1] R.M. Ormerod, Solid oxide fuel cells, Chem. Soc. Rev. 32 (2003) 17–28. doi:10.1039/b105764m.

[2] E.D. Wachsman, C. A. Marlowe, K.T. Lee, Role of solid oxide fuel cells in a balanced energy strategy, Energy Environ. Sci. 5 (2012) 5498–5509. doi:10.1039/c1ee02445k.

[3] A. Atkinson, S. Barnett, R.J. Gorte, J.T.S. Irvine, A J. McEvoy, M. Mogensen, et al., Advanced anodes for high-temperature fuel cells., Nat. Mater. 3 (2004) 17–27. doi:10.1038/nmat1040.

[4] T.A. Adams II, P.I. Barton, High-Efficiency Power Production from Coal with Carbon Capture, Process Syst. Eng. 56 (2010) 3120–3136. doi:10.1002/aic.

[5] T. A. Adams II, P.I. Barton, High-efficiency power production from natural gas with carbon capture, J. Power Sources. 195 (2010) 1971–1983. doi:10.1016/j.jpowsour.2009.10.046.

[6] D.D. Hsu, D. Inman, G. A. Heath, E.J. Wolfrum, M.K. Mann, A. Aden, Life Cycle Environmental Impacts of Selected U.S. Ethanol Production and Use Pathways in 2022, Environ. Sci. Technol. 44 (2010) 5289–5297. doi:10.1021/es100186h.

[7] H. Wu, M., Wang, M., Liu, J., Huo, Life-Cycle Assessment of Corn-Based Butanol as a Potential Transportation Fuel, 2007.

[8] R.J. Gorte, J.M. Vohs, Catalysis in Solid Oxide Fuel Cells, Annu. Rev. Chem. Biomol. Eng. 2 (2011) 9–30. doi:10.1146/annurev-chembioeng-061010-114148.

[9] S. McIntosh, R.J. Gorte, Direct hydrocarbon solid oxide fuel cells., Chem. Rev. 104 (2004) 4845–65.

[10] S. Park, J. Vohs, R. Gorte, Direct oxidation of hydrocarbons in a solid-oxide fuel cell, Nature. 404 (2000) 265–7. doi:10.1038/35005040.

[11] S. Helveg, C. Lopez-Cartes, J. Sehested, P. Hansen, B. Clausen, J. Rostrup-Nielsen, et al., Atomic-scale imaging of carbon nanofibre growth, Nature. 427 (2004) 426–429. doi:10.1038/nature02308.1.

[12] Y. Kim, J.H. Kim, J. Bae, C.W. Yoon, S.W. Nam, In Situ Analyses of Carbon Dissolution into Ni-YSZ Anode Materials, J. Phys. Chem. C. 116 (2012) 13281–13288. doi:10.1021/jp3035693.

[13] K.S. Blinn, H. Abernathy, X. Li, M. Liu, L. A. Bottomley, M. Liu, Raman spectroscopic monitoring of carbon deposition on hydrocarbon-fed solid oxide fuel cell anodes, Energy Environ. Sci. 5 (2012) 7913–7917. doi:10.1039/c2ee21499g.

[14] E. Nikolla, J. Schwank, S. Linic, Direct Electrochemical Oxidation of Hydrocarbon Fuels on SOFCs: Improved Carbon Tolerance of Ni Alloy Anodes, J. Electrochem. Soc. 156 (2009) B1312–B1316. doi:10.1149/1.3208060.

[15] M.B. Pomfret, J. Marda, G.S. Jackson, B.W. Eichhorn, A. M. Dean, R. A. Walker, Hydrocarbon Fuels in Solid Oxide Fuel Cells: In Situ Raman Studies of Graphite Formation and Oxidation, J. Phys. Chem. C. 112 (2008) 5232–5240. doi:10.1021/jp711312p.

[16] M.B. Pomfret, D. A. Steinhurst, J.C. Owrutsky, Methanol and Ethanol Fuels in Solid Oxide Fuel Cells: A Thermal Imaging Study of Carbon Deposition, Energy & Fuels. 25 (2011) 2633–2642. doi:10.1021/ef2003975.

[17] M.B. Pomfret, J.C. Owrutsky, R. A Walker, High-temperature Raman spectroscopy of solid oxide fuel cell materials and processes., J. Phys. Chem. B. 110 (2006) 17305–8. doi:10.1021/jp063952l.

[18] R.A. Eigenbrodt, Bryan C., Kirtley, J.D., Walker, In-situ optical studies of solid oxide fuelcell operating with dry and humidified oxygenated fuels, ECS Trans. 35 (2011) 2789–2798.

[19] K. Sasaki, K. Watanabe, Y. Teraoka, Direct-Alcohol SOFCs: Current-Voltage Characteristics and Fuel Gas Compositions, J. Electrochem. Soc. 151 (2004) A965–A970. doi:10.1149/1.1756884.

[20] S.D. Nobrega, M.V. Galesco, K. Girona, D.Z. de Florio, M.C. Steil, S. Georges, et al., Direct ethanol solid oxide fuel cell operating in gradual internal reforming, J. Power Sources. 213 (2012) 156–159. doi:10.1016/j.jpowsour.2012.03.104.

[21] X.F. Ye, S.R. Wang, Q. Hu, Z.R. Wang, T.L. Wen, Z.Y. Wen, Improvement of multi-layer anode for direct ethanol Solid Oxide Fuel Cells, Electrochem. Commun. 11 (2009) 823–826. doi:10.1016/j.elecom.2009.02.003.

[22] K. Sasaki, Y. Teraoka, Equilibria in Fuel Cell Gases II, J. Electrochem. Soc. 150 (2003) A885–A888. doi:10.1149/1.1577338.

[23] K. Sasaki, Y. Teraoka, Equilibria in Fuel Cell Gases I, J. Electrochem. Soc. 150 (2003) A878–A884. doi:10.1149/1.1577338.

[24] E. Nikolla, J. Schwank, S. Linic, Hydrocarbon steam reforming on Ni alloys at solid oxide fuel cell operating conditions, Catal. Today. 136 (2008) 243–248. doi:10.1016/j.cattod.2008.03.028.

[25] E. Nikolla, J. Schwank, S. Linic, Comparative study of the kinetics of methane steam reforming on supported Ni and Sn/Ni alloy catalysts: The impact of the formation of Ni alloy on chemistry, J. Catal. 263 (2009) 220–227. doi:10.1016/j.jcat.2009.02.006.

[26] D. Yoon, A. Manthiram, Hydrocarbon-fueled solid oxide fuel cells with, J. Mater. Chem. A. 2 (2014) 17041–17046. doi:10.1039/C4TA02662D.

[27] H. Kan, H. Lee, Sn-doped Ni/YSZ anode catalysts with enhanced carbon deposition resistance for an intermediate temperature SOFC, Appl. Catal. B Environ. 97 (2010) 108–114. doi:10.1016/j.apcatb.2010.03.029.

[28] Y. Leng, Performance evaluation of anode-supported solid oxide fuel cells with thin film YSZ electrolyte, Int. J. Hydrogen Energy. 29 (2004) 1025–1033. doi:10.1016/j.ijhydene.2004.01.009.

[29] S. McIntosh, J.M. Vohs, R.J. Gorte, Role of Hydrocarbon Deposits in the Enhanced Performance of Direct-Oxidation SOFCs, J. Electrochem. Soc. 150 (2003) A470–A476. doi:10.1149/1.1559064.

[30] E. Nikolla, J. Schwank, S. Linic, Promotion of the long-term stability of reforming Ni catalysts by surface alloying, J. Catal. 250 (2007) 85–93. doi:10.1016/j.jcat.2007.04.020.

[31] E. Nikolla, A. Holewinski, J. Schwank, S. Linic, Controlling carbon surface chemistry by alloying: carbon tolerant reforming catalyst., J. Am. Chem. Soc. 128 (2006) 11354–5. doi:10.1021/ja0638298.

Chapter 4

Oxidative Coupling of Methane to Ethane and Ethylene: Assessment of Membrane Reactors for Potential Increases in Yield and Selectivity of C_2 Products

4.1 Summary

Despite large amounts of research performed on processes to convert methane directly to higher value fuels and chemicals, there are still no commercial scale processes that use these technologies due to the low single pass yield of products that can be obtained. In this chapter, the process of oxidative coupling of methane (OCM) to ethane and ethylene (C_2) is analyzed in order to determine how the single pass yield could be increased. A model was developed using kinetic data available in the literature and is used to demonstrate that a plug flow reactor system with distributed oxygen (a plug flow solid oxide membrane reactor) could substantially increase the C_2 yield for this process over a packed bed reactor. Additionally, the state of the art of solid oxide membrane reactors for oxidative coupling of methane is discussed along with potential improvements that could increase the oxygen flux, catalyst integration, and overall C_2 yield of solid oxide membrane reactors.

4.2 Introduction

Over the last several decades, a large amount of research has focused on the direct conversion of methane to alcohols or higher hydrocarbons. Although much of this research was conducted in the 1980's and 1990's, interest in these processes is currently increasing. The value proposition of such a process is compelling for several reasons. First, over the last decade, methane production has increased due to recovery of shale gas and tight oil [1,2], while at the same time, the price of methane rich natural gas has decreased compared to crude oil [3]. Furthermore, the current processes that convert methane to alcohols or olefins require the intermediate step of reforming methane to synthesis gas (CO and H_2). This step not only complicates the overall process, but it is also very expensive [2,4]. Finally, much of the natural gas that is recovered as a byproduct of oil recovery is considered "stranded", and because it cannot currently be utilized economically, it is combusted in flares releasing the greenhouse gas CO_2 into the atmosphere [2].

Although there are potentially financial and environmental incentives to convert methane directly to more valuable products, there is still yet to be a commercial scale chemical plant converting methane directly to methanol or olefins. In this chapter, we have analyzed one of these processes, the oxidative coupling of methane, in order to determine where research should be focused to result in higher single pass yields of methane.

Oxidative coupling of methane (OCM) has been researched extensively since the first reports in the early 1980's by Keller and Bhasin and Hinsen and Baerns [5,6]. The proposed mechanism for this process involves the extraction of a hydrogen atom from a

methane molecule by oxygen on the surface of a metal oxide catalyst [7]. The remaining methyl radical ($*CH_3$) is then released from the surface of the catalyst and couples with another methyl radical in the gas phase to form ethane [8]. The OH group on the catalyst surface then extracts another hydrogen atom from methane and desorbs from the surface as water.

Since the initial reports of the process, several strategies have been used by researchers to find catalysts that would increase the yield of ethane and ethylene (C_2 products). Many of the studies have focused on mixed metal oxide catalysts operating at temperatures between 943 and 1223 K [9]. As of 2011 more than 2800 papers, patents, and technical reports had been published on this type of catalyst [9]. In 2011, a statistical analysis of OCM data from over 400 publications was done by Zavyalova et al. which resulted in recommendations for elemental composition that would likely give high selectivity and yield [9]. In a follow up publication, many of their proposed catalysts were tested and they found that although the model based on their statistical analysis was moderately accurate at predicting the overall yield in a packed bed reactor, there was no catalyst found that was significantly better than those previously tested [10]. In addition to the metal oxide catalyst testing, there have also been reports using sulfur as an oxidant instead of oxygen to limit the thermodynamic driving force to undesired products [11] and studies demonstrating C-C coupling using liquid phase complexes operating at low temperatures [12]. Although these reports are scientifically interesting, the yield of C_2 products and the likelihood for commercialization are very low for these processes.

Figure 4.1 shows the single pass methane conversion and C_2 selectivity for published OCM catalysts with some of the highest C_2 yields. Dashed lines mark C_2

yields of 20% and 30% on the graph for reference. We note that all of the catalysts that show high yields of C_2 products are mixed metal oxides with relatively complex formulas. Figure 4.1 also shows a shaded area which represents the techno-economic targets for commercialization of OCM. The techno-economic targets state that in order to be economically commercialized, single pass yield and selectivity need to be greater than 30% (yield) and about 90% (selectivity) [13]. Although these techno-economic targets are highly cited in OCM literature, the targets were published in a 1989 report considering methane to olefins processes using un-diluted feed streams of methane and air, and different targets may be more applicable to current processes.

The data in Figure 4.1 show that OCM catalysts can be operated at high selectivity and relatively low conversion or at high conversion with low selectivity. This trend is due to formation of the undesired products CO and CO_2 (CO_x) within the reactor. CO_x products are thermodynamically more favorable than the C_2 products as shown in Figure 4.2a, where the ΔG of the CO_x products is lower than that of the C_2 products at 1073 K. Figure 4.2b shows the equilibrium carbon product distributions at 1073 K for varied O_2/CH_4 ratios introduced into the reactor. At low O_2/CH_4 ratios, solid carbon makes up the largest fraction of the products. As the O_2/CH_4 ratio increases, the favored product switches to CO and then CO_2 at very high ratios of O_2/CH_4. It is interesting to note that ethane and ethylene are never represented in the equilibrium product distribution, indicating that for high selectivity to ethane and ethylene, OCM reactors should be kept far from equilibrium. It is suggested that the CO_x products can be formed either directly from methane and oxygen, or by the sequential oxidation of the C_2 products [14], as shown in Scheme 4.1. A kinetic analysis of the reactions in the network

in Scheme 4.1, performed using a La_2O_3/CaO catalyst, illustrated that the reactions leading to CO_x products exhibited approximately 1st order dependence on the partial pressure of O_2, while the reactions leading to the desired C_2 products showed ½ order dependence on O_2 [14]. This kinetic information suggests that higher C_2 selectivity should be achieved at relatively low partial pressures of oxygen. However, in a conventional plug flow packed bed reactor, high oxygen partial pressures are required for high methane conversion. This, coupled with the strong thermodynamic driving force towards undesired reactions results in reactor systems that are unable to operate within the techno-economic target area.

After considering the reaction network and kinetic data, it is clear that improvements in the catalyst alone will likely not significantly increase the yield of C_2 products produced by an OCM reactor. Instead, the entire reactor system needs to be considered. From our analysis of the reaction network, the reaction will have the highest selectivity to C_2 products when operated under the conditions of *low mixing and low partial pressures of oxygen*. Low mixing can be achieved when plug flow reactors are used, however low partial pressures of oxygen are more difficult to achieve while maintaining high conversion. One strategy is to have multiple catalyst beds in series with the flow of oxygen divided across them. This technique has been effective at slightly increasing the yield of packed bed reactors [15]. Another strategy is to use a reactor where the methane and oxygen streams are kept separate, and a membrane material selectively allows oxygen flux (as O^{2-}) from the oxygen side to the methane side along the entire length of the reactor (a plug flow membrane reactor) [16].

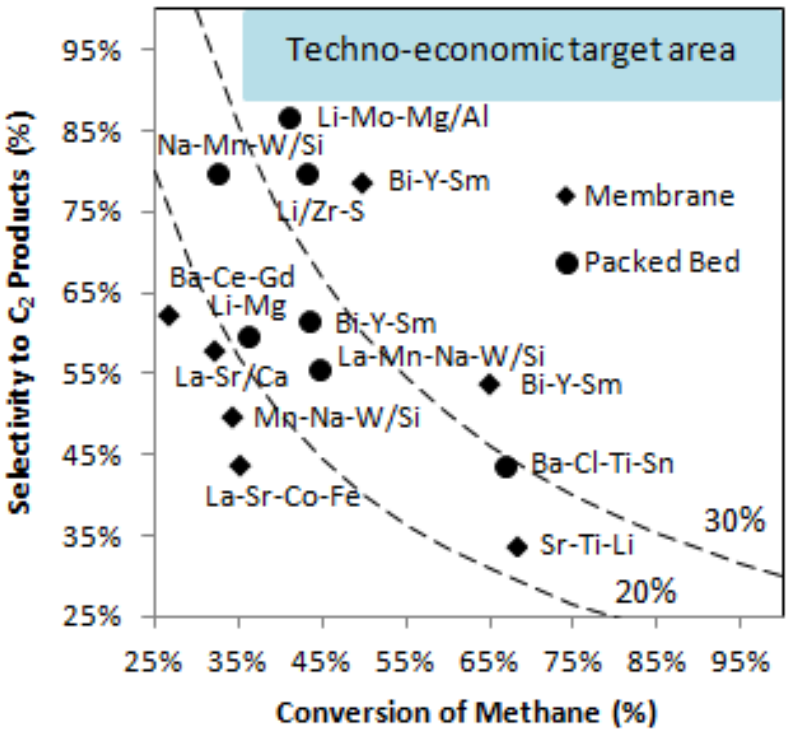

Figure 4.1: Published methane conversion and C_2 selectivity data for metal oxide catalysts (all catalysts are oxides, however oxygen has been omitted in the formulas to save space). Circles indicate that the reaction was performed in a packed bed reactor and diamonds indicate that the reaction was performed in a membrane reactor. Data from [15,17–30]

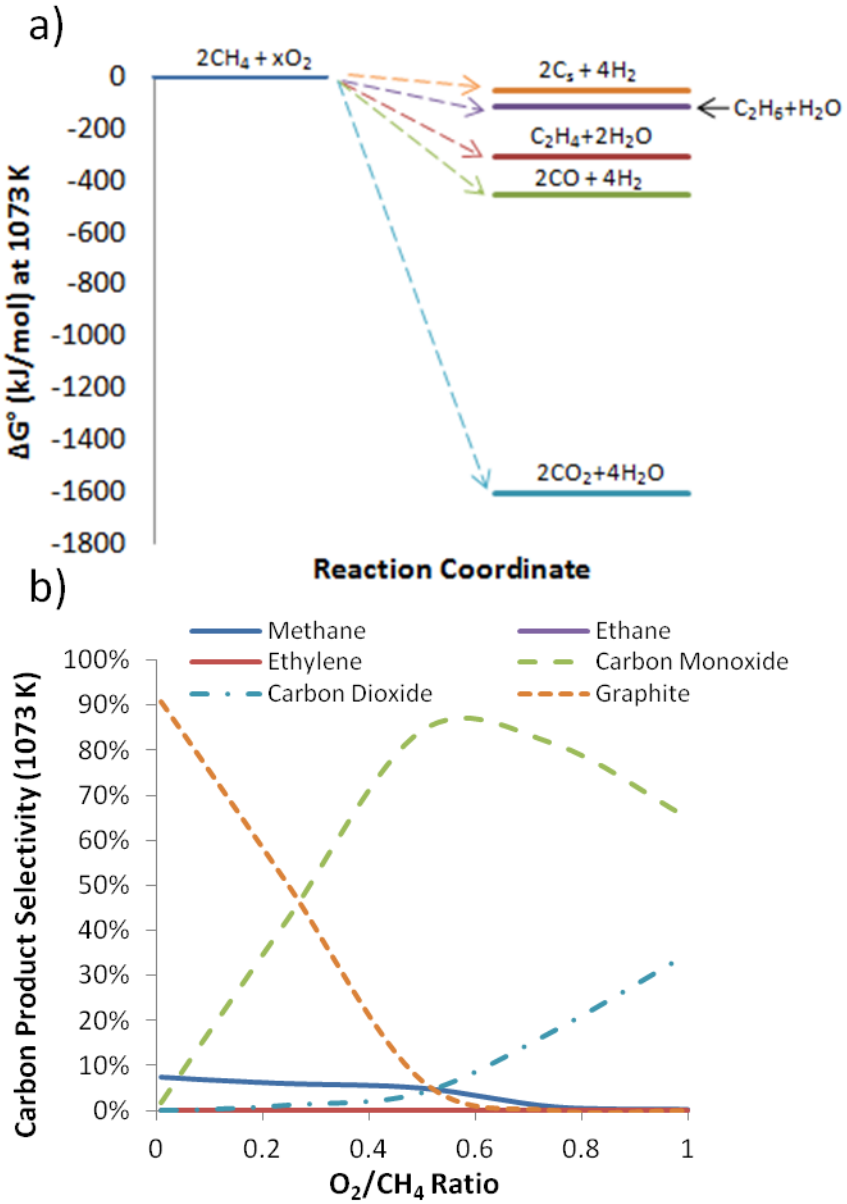

Figure 4.2: a) The change in Gibbs free energy for the reactions that can occur in an OCM reactor at 1073 K and 1 atm, where C_s is solid graphitic carbon b) Thermodynamic carbon product selectivity for a reactor at 1073 K with minimized Gibbs free energy as a function of the O_2/CH_4 ratio in the feed

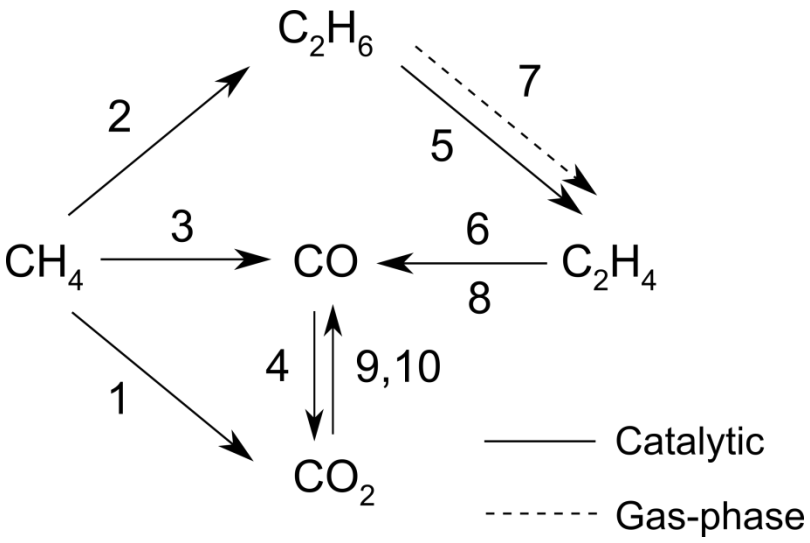

Reaction 1: $CH_4 + 2O_2 \rightarrow CO_2 + 2H_2O$

Reaction 2: $2CH_4 + 0.5O_2 \rightarrow C_2H_6 + H_2O$

Reaction 3: $CH_4 + O_2 \rightarrow CO + H_2O + H_2$

Reaction 4: $CO + 0.5O_2 \rightarrow CO_2$

Reaction 5: $C_2H_6 + 0.5O_2 \rightarrow C_2H_4 + H_2O$

Reaction 6: $C_2H_4 + 2O_2 \rightarrow 2CO + 2H_2O$

Reaction 7: $C_2H_6 \rightarrow C_2H_4 + H_2$

Reaction 8: $C_2H_4 + 2H_2O \rightarrow 2CO + 4H_2$

Reaction 9: $CO + H_2O \rightarrow CO_2 + H_2$

Reaction 10: $CO_2 + H_2 \rightarrow CO + H_2O$

Scheme 4.1: OCM reaction network, reproduced from Stansch et al [14]

4.3 Reactor Models

To determine the potential impact of using a plug flow membrane reactor on the conversion of methane and the selectivity and yield of C_2 products, we created a plug flow reactor model in MatLab using the reaction network, rate equations, and kinetic parameters provided by Stansch et al. for a La_2O_3/CaO catalyst [14]. This was a relatively simple model which considers only the 10 reactions shown in Scheme 4.1, and it was not intended to be a universal kinetic model for all OCM catalysts. However, it was useful to gain insights into which processes have the largest impact on the yield and selectivity in different types of reactors. One version of the model was set up as a plug flow reactor with oxygen and methane flows set as initial conditions, and the other as a membrane reactor where the membrane tube is modeled as $La_{0.6}Sr_{0.4}Co_{0.2}Fe_{0.8}O_{3-\delta}$ (LSCF). The equations and parameters describing the flux through the membrane are from Akin et al [31]. Table 4.1 shows the inputs for each model.

Table 4.1: OCM Reactor model inputs. [a] Based on catalyst weight/density [b] Based on membrane reactor diameter of 6 mm [c] This parameter is listed as the "number of experiments" in the kinetic model but its value was not specified by Stansch et al.

Parameter	Packed Bed Reactor (plug flow)	Membrane Reactor (plug flow)
CH_4/O_2	4.26	4.26
Reactor Temperature (K)	1073	1073
Methane flow rate/catalyst mass (mol/(min*g))	0.0087	0.0087
Reactor Volume (cm^3)	0.06[a]	7.8[b]
n [c]	1	1
Membrane Surface Area (cm^2)	N/A	50

Figure 4.3 shows the molar flow rate of each component in mmol/sec as a function of the catalyst surface area in the packed bed plug flow reactor model and in the

membrane plug flow reactor model. The results from the packed bed reactor model showed a C_2 selectivity of 57%, a methane conversion of 28%, and C_2 yield of 16%. These results are reasonable compared to the experimental data available for a similar La_2O_3/CaO catalyst with C_{2+} selectivity of 47.2%, CH_4 conversion of 34.0%, and C_{2+} yield of 16.0% at 1113 K [32]. The results from the membrane reactor model showed a C_2 selectivity of 85%, a C_2 conversion of 45%, and a C_2 yield of 38%. Therefore, the membrane reactor model predicted significantly higher selectivity and yield of C_2 products. It is also interesting to note that the conversion of methane in the membrane reactor is higher than in the packed bed reactor. This is due to the fact that the C_2 products require less oxygen consumption than the unselective CO_x products. The results for the membrane reactor are promising in terms of the yield and selectivity to C_2 products, however it is important to note that the membrane reactor requires a much larger volume due to the membrane surface area that is required for oxygen flux into the reactor. This will not only impact the overall cost of the reactor, but the gas phase reactions will also likely be more significant.

4.4 Sensitivity Analysis

To further understand the influence of the reaction steps on the C_2 yield and selectivity, we performed a sensitivity analysis on the reaction network. For each reaction in the network, a sensitivity coefficient (S_i) was calculated using equation 4.1, where Z_{C2} is the overall yield or selectivity to C_2 products, and k_i is the rate constant for the reaction [33]:

$$S_i = \left(\frac{\partial Z_{C2}}{\partial k_i}\right)_{k_j} \left(\frac{k_i}{Z_{C2}}\right) \approx \left(\frac{\delta Z_{C2}}{\delta k_i}\right)_{k_j} \left(\frac{k_i}{Z_{C2}}\right) \qquad (4.1)$$

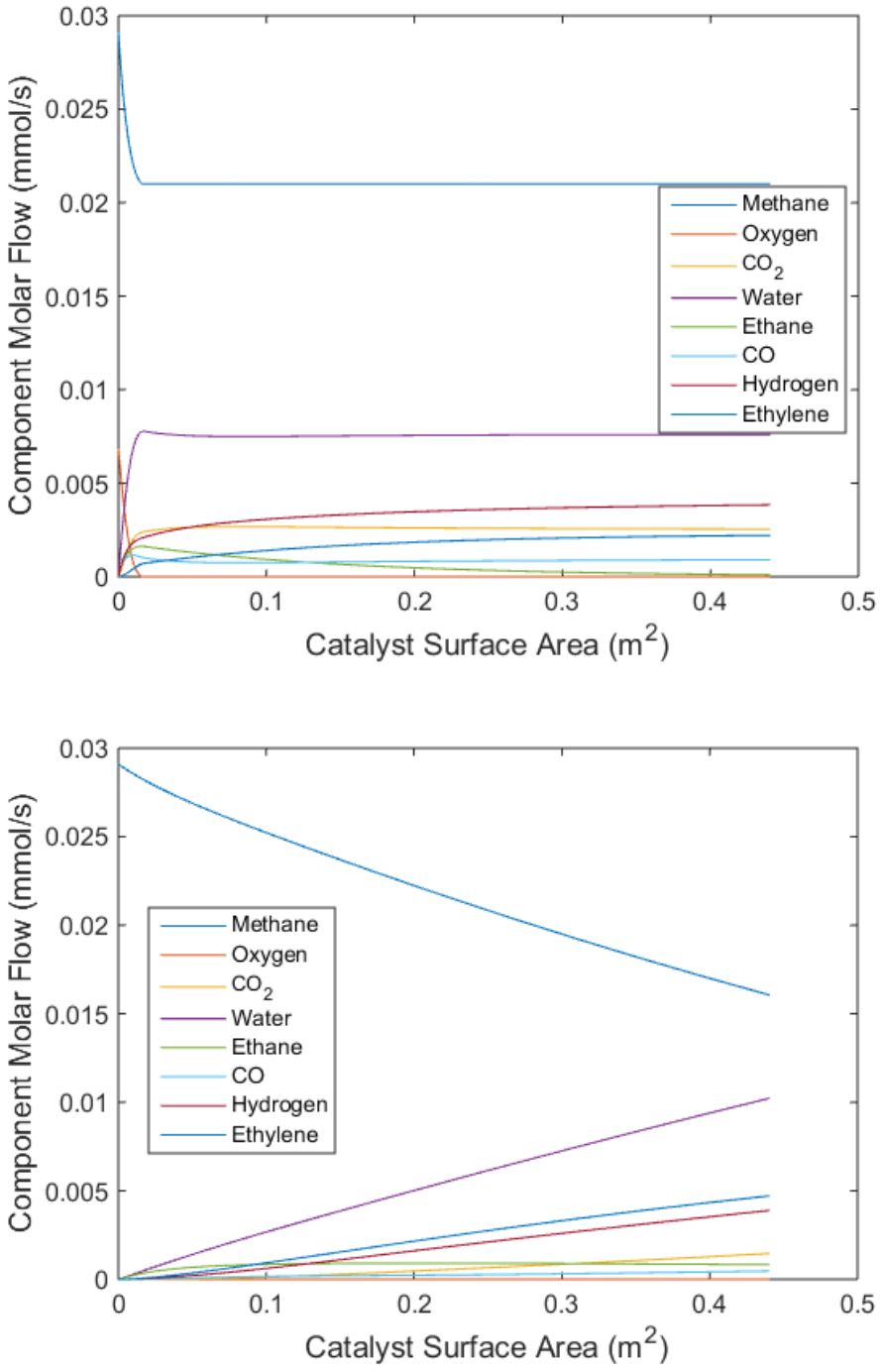

Figure 4.3: Molar flow rate of each reactant and product within a packed bed plug flow reactor (top) and a membrane plug flow reactor (bottom).

Figure 4.4 shows the sensitivity coefficients for each reaction in the reaction network of Scheme 1 as well as for the oxygen flux in the membrane reactor. For these calculations, δk_i was 0.1% of the original published value. A positive sensitivity coefficient indicates that the change in yield or selectivity (δZ_{C2}) has the same sign as δk_i (e.g. the yield increases as k_i increases), whereas a negative sensitivity coefficient indicates that δZ_{C2} has the opposite sign as δk_i. For the packed bed reactor the sensitivity coefficients for the yield indicate that the C_2 yield is most dependent on the rate of ethane production, followed by the rate of the oxidation of ethane to ethylene, and finally the rate of direct conversion of methane to CO_x products. The sensitivity coefficients for the selectivity in the packed bed reactor have the same sign as the sensitivity coefficients for the yield, indicating that the changes in yield correspond to the changes in the selectivity. On the other hand, for the membrane reactor, the C_2 yield is most dependent on the rate of the oxygen flux into the reactor, followed by the rate of ethane production, and finally the rate of ethylene oxidation. The sensitivity coefficients for the C_2 selectivity in the membrane reactor also have the same sign as the sensitivity coefficients for the yield, except for the oxygen flux, where the sensitivity coefficients for the selectivity and yield have opposite signs. This indicates that the increase in yield due to the higher oxygen flux is due to an increase in the conversion.

Overall, the sensitivity coefficients indicate that beyond ethane formation from the oxidative coupling reaction, the packed bed and membrane reactors have different critical reactions and thus their catalysts should be optimized differently. For the packed bed reactor, the rate of direct conversion of methane to CO_x is significant, and ethylene that is formed is quickly consumed by sequential reactions. To increase the yield, the

oxidative coupling reaction to form ethane should be accelerated, while the direct formation of CO_x products and the production of ethylene should be suppressed as much as possible. For the membrane reactor, the critical steps are the rate of oxygen into the reactor and oxidation of ethylene. To increase the yield, membranes with higher oxygen flux should be used and the catalyst should accelerate the oxidative coupling reaction to form ethane and suppress the oxidation of ethylene. Of course, in reality it is difficult to change rate constants independently on the same catalyst; however, increasing the oxygen flux may be a realistic goal.

The analysis presented on the reactors using a kinetic model indicates that membrane reactors can theoretically offer higher selectivity to C_2 products and higher conversion of methane leading to higher C_2 yields; however, data for membrane reactors in Figure 4.1 indicates that the yields of C_2 products for this type of reactor are not substantially higher than the best performing packed bed reactors. Although this seems discouraging, this may be due to the fact that there are relatively few reports of OCM membrane reactors, and only a small number of membranes and catalysts have been tested. Therefore, more research is needed to determine the full potential of this technology.

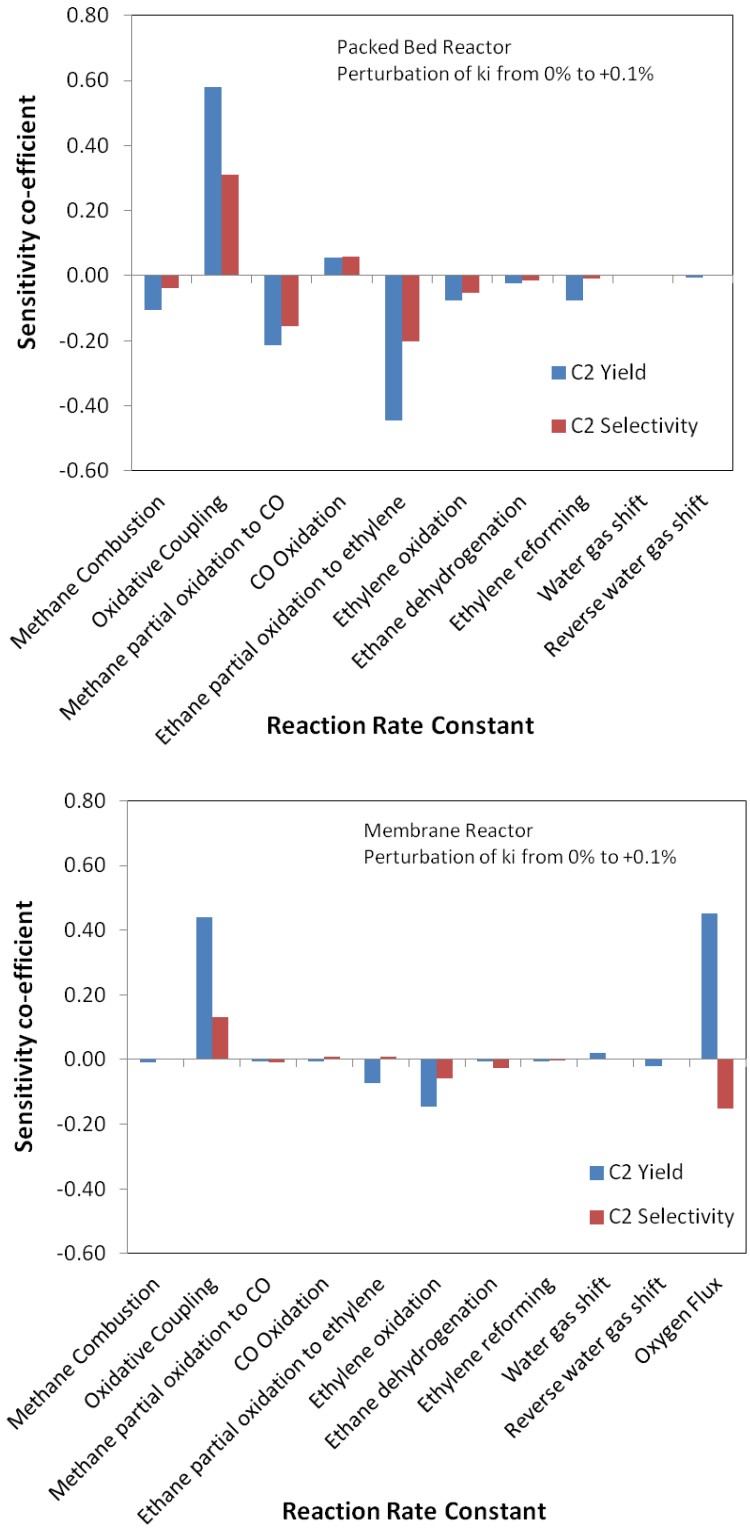

Figure 4.4: Sensitivity coefficients for the yield and selectivity of C_2 products for packed bed and membrane plug flow reactors

4.5 Solid Oxide Membrane Reactors

It is well established that high temperature membrane reactors using solid oxide materials can transport oxygen as O^{2-} through oxygen vacancies in the solid oxide lattices [34]. However, limits on oxygen flux across the membrane result in either large membrane surface areas or limited methane conversion. In order for oxygen to move from one side of the membrane to the other several processes must occur. 1) Oxygen dissociates and combines with electrons on the air side catalyst surface to form O^{2-}. 2) O^{2-} is transported through oxygen vacancies in the air side catalyst to the membrane. 3) O^{2-} is transported through the oxygen vacancies in the membrane to the methane side. 4) O^{2-} is transferred to the methane side catalyst where it reacts with methane. 5) Electrons are returned to the air side catalyst. The last step can occur in two different ways, depending on the type of membrane used. There are two main types of membranes, those with ionic conductivity and those with mixed ionic and electronic conductivity (MIEC). Figure 4.5 shows the two basic types of membrane reactor and how they are operated; 1) a membrane reactor with an electronically and ionically conductive membrane and electron transfer directly through the membrane (Figure 4.5a), and 2) a membrane reactor with an ionically conductive membrane, electronically and ionically conductive catalyst on either side of the membrane, and an external circuit for electron transfer (Figure 4.5b). In both types of membrane reactor, the O^{2-} flux is dependent on the temperature, oxygen partial pressure difference across the membrane, membrane thickness, and the difference in the potential across the membrane (for reactors including an external circuit). The increases in O^{2-} flux due to increased temperature and partial pressure of oxygen across the membrane have been well documented by many researchers [31]; however, the effect

of the membrane thickness and the effect of controlling the flux by changing the potential across the membrane have not been well studied for OCM.

The membrane reactors recently fabricated and tested for OCM have been membrane supported, where the membrane itself provides the structure for the reactor. These membranes have a thickness of ~200 μm or more in most cases. However, solid oxide membranes supported by porous structures can be much thinner. Membrane thicknesses of 10-50 μm can be relatively easily fabricated, and it has been found that thinner membranes decrease the resistance across the membrane, increasing oxygen flux [35]. Similar techniques should be explored to increase oxygen flux in OCM membrane reactors.

Another strategy to increase the flux in solid oxide membrane reactors is to use a membrane without electronic conductivity, and control the flux electrochemically using a system like the one in Figure 4.5b. Although there have been studies which employed this technique for OCM, there have been many advances in solid oxide membrane reactor technology since their publication [16]. One advantage to this type of system is that membrane materials could be used that have higher ionic conductivity than MIEC materials but do not have electronic conductivity, such as lanthanum gallate doped with strontium and magnesium ($La_{0.8}Sr_{0.2}Ga_{0.8}Mg_{0.2}O_{3-\delta}$ or LSGM) [36] or lanthanum germanates (such as $La_{9.33}Ge_6O_{26}$) [37]. Use of these materials could lead to increased flux of O^{2-} across the membrane. Additionally, the external circuit in these systems can be used to change the potential difference across the membrane and therefore control the O^{2-} flux. The circuit can also be used to add additional electrons to the system, using the system as an oxygen pump to increase the flux electrochemically [16]. These advantages

could be really useful in an OCM system, however more research must be done to determine what materials are best suited for each component in this type of system.

Beyond just increasing the flux of O^{2-} across the membrane, research should also be focused on developing OCM catalysts that are specifically tailored for membrane reactor systems. Although it is possible to use the membrane for both oxygen flux and activation of methane, from the available literature on OCM membrane reactors, it is apparent that adding a selective OCM catalyst to the membrane reactor results in higher yields [27,29]. Despite these findings, few catalysts have been tested, and many were not chosen specifically for their compatibility in a membrane reactor. Therefore it is likely that improvements can be made if catalysts are developed specifically for this type of reactor.

Optimal catalysts for membrane reactor systems not only need to have high selectivity to C_2 products, but they also need to be designed to be integrated with the solid oxide membrane and operated at membrane reactor conditions (we note here that the "catalyst" in a membrane reactor system could be one material or multiple materials that when mixed together have the desired properties). The properties required for a membrane reactor catalyst are summarized in Table 4.2. In a membrane reactor system, oxygen is transported through the solid oxides as O^{2-}, and in order for the transfer of O^{2-} between the membrane and catalysts to occur, the catalyst must be ionically conductive and in close contact with the membrane. To achieve the contact area required for O^{2-} transfer, catalysts in solid oxide membrane systems are often fabricated at high temperatures (>1273 K) where the catalyst is sintered to the membrane layer. At these high temperatures, solid state reactions can occur between the membrane and catalyst

materials which can change the material properties [38,39]. Furthermore, materials with dissimilar coefficients of thermal expansion can cause problems including delamination of the catalyst from the membrane, or in more extreme cases, can cause the membrane reactor to crack and leak [35]. Therefore, the compatibility of the membrane and catalyst materials should be considered carefully. In membrane reactors using an external circuit for electron transfer, the methane side catalyst must also be electronically conductive to transfer electrons to the external circuit. In addition to these requirements, the catalyst material must also be designed to withstand the high temperatures and high methane and ethylene concentrations that are present in a membrane reactor. High concentrations of methane and ethylene and low concentrations of oxygen at high temperatures can result in carbon deposits that form on the catalyst and degrade its activity [40].

Table 4.2: Properties required for an optimal membrane reactor catalyst

Property	Electronically and ionically conductive membrane reactor	Ionically conductive membrane with external circuit
High selectivity to C_2 products	x	x
Ionic conductivity	x	x
Electronic conductivity		x
Chemical compatibility at high temperature	x	x
Similar coefficient of thermal expansion as the membrane	x	x
Stable at high temperatures and high concentrations of methane and ethylene	x	x

4.6 Conclusions

In this chapter, we have assessed a methane oxidative coupling process in packed bed and membrane reactors. From the results, we have found that it is likely that improvements in packed bed reactor catalysts alone will not reach the techno-economic targets for OCM. In order to increase the single pass yield of C_2 products, solid oxide membrane reactors should be tested with catalysts that are specifically designed to operate in a membrane reactor. More research is required to develop membrane reactors for this process that are made of compatible materials, have high O^{2-} flux through the membrane, have facile O^{2-} transfer between the membrane and the catalyst, are capable of returning the electrons to the air side, and have high selectivity to C_2 products at the operating conditions. Overall, many technical hurdles must be overcome before membrane reactors can be considered as an option for commercialization, however, they can theoretically provide large increases in selectivity and yield of C_2 products over packed bed reactors.

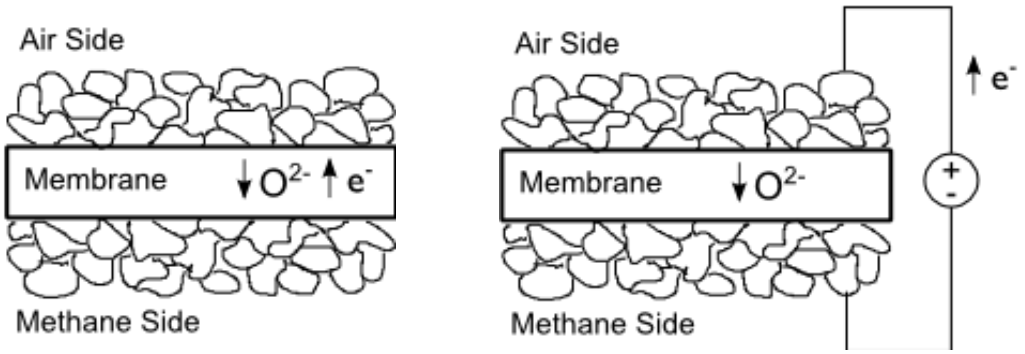

Figure 4.5: Schematic of solid oxide membrane reactors with: a) electronic and ionically conductive membrane and b) ionically conductive membrane with electronically conductive catalysts and external circuit

4.7 References

[1] BP Energy Outlook 2035, 2014.

[2] E. McFarland, Unconventional Chemistry for Unconventional Natural Gas, Science (80-.). 338 (2012) 340–342. doi:10.1126/science.1226840.

[3] Energy Information Administration, Monthly Energy Review: September 2015, (n.d.). http://www.eia.gov/totalenergy/data/monthly/#prices (accessed December 10, 2015).

[4] K. Aasberg-Petersen, C.S. Nielsen, I. Dybkjær, J. Perregaard, Large Scale Methanol Production from Natural Gas, n.d.

[5] G. Keller, M. Bhasin, Synthesis of ethylene via oxidative coupling of methane I. Determination of active catalysts, J. Catal. 73 (1982) 9–19. doi:10.1016/0021-9517(82)90075-6.

[6] W. Hinsen, M. Baerns, Oxidative coupling of methane to C2 hydrocarbons in the presence of different catalysts, Chem. Zeitung. 107 (1983) 223–226.

[7] J.H. Lunsford, Catalytic conversion of methane to more useful chemicals and fuels: A challenge for the 21st century, Catal. Today. 63 (2000) 165–174. doi:10.1016/S0920-5861(00)00456-9.

[8] L. Luo, X. Tang, W. Wang, Y. Wang, S. Sun, F. Qi, et al., Methyl Radicals in Oxidative Coupling of Methane Directly Confirmed by Synchrotron VUV Photoionization Mass Spectroscopy., Sci. Rep. 3 (2013) 1625. doi:10.1038/srep01625.

[9] U. Zavyalova, M. Holena, R. Schlögl, M. Baerns, Statistical analysis of past catalytic data on oxidative methane coupling for new insights into the composition of high-performance catalysts, ChemCatChem. 3 (2011) 1935–1947. doi:10.1002/cctc.201100186.

[10] E. Kondratenko, M. Schluter, M. Baerns, D. Linke, M. Holena, Developing catalytic materials for the oxidative coupling of methane through statistical analysis of literature data, Catal. Sci. Technol. 5 (2015) 1668–1677. doi:10.1039/C4CY01443J.

[11] Q. Zhu, S.L. Wegener, C. Xie, O. Uche, M. Neurock, T.J. Marks, Sulfur as a selective "soft" oxidant for catalytic methane conversion probed by experiment and theory., Nat. Chem. 5 (2013) 104–109. doi:10.1038/nchem.1527.

[12] M.D. Lotz, M.S. Remy, D.B. Lao, A. Ariafard, B.F. Yates, A.J. Canty, et al., Formation of ethane from mono-methyl palladium(II) complexes, J. Am. Chem. Soc. 136 (2014) 8237–8242. doi:10.1021/ja412338k.

[13] J.C.W. Kuo, C.T. Kresge, R.E. Palermo, Evaluation of Direct Methane Conversion to Higher Hydrocarbons and Oxygenates, Catal. Today. 4 (1989) 463–470.

[14] Z. Stansch, L. Mleczko, M. Baerns, Comprehensive Kinetics of Oxidative Coupling of Methane over the La_2O_3/CaO Catalyst, Ind. Eng. Chem. Res. 36 (1997) 2568–2579. doi:10.1021/ie960562k.

[15] B.K. Miremadi, S.R. Morrison, K. Colbow, Ethylene from Methane and Catalysts Therefor, United States Patent 5245124, 1993.

[16] D. Eng, M. Stoukides, Catalytic and Electrocatalytic Methane Oxidation with Solid Oxide Membranes, Catal. Rev. 33 (1991) 375–412. doi:10.1080/01614949108020304.

[17] J. Wu, H. Zhang, S. Qin, C. Hu, La-promoted $Na_2WO_4/Mn/SiO_2$ catalysts for the oxidative conversion of methane simultaneously to ethylene and carbon monoxide, Appl. Catal. A Gen. 323 (2007) 126–134. doi:10.1016/j.apcata.2007.02.009.

[18] V. Choudhary, Influence of Precursors Used in Preparation of MgO on Its Surface Properties and Catalytic Activity in Oxidative Coupling of Methane, J. Catal. 145 (1994) 300–311. doi:10.1006/jcat.1994.1038.

[19] S. Zarrinpashne, R. Ahmadi, M. Zekordi, Catalyst Direct Conversion of Methane to Ethane and Ethylene, United States Patent Application 20060155157A1, 2006.

[20] K. Murata, T. Hayakawa, K. Fujita, Excellent effect of lithium-doped sulfated zirconia catalysts for oxidative coupling of methane to give ethene and ethane, Chem. Commun. 45 (1997) 221–222. doi:10.1039/a606624k.

[21] I. Matsuura, Y. Utsumi, M. Nakai, T. Doi, Oxidative Coupling of Methane over Lithium-Promoted Zinc Oxide Catalyst, Chem. Lett. (1986) 1981–1984.

[22] Y. Zeng, F.T. Akin, Y.S. Lin, Oxidative coupling of methane on fluorite-structured samarium–yttrium–bismuth oxide, Appl. Catal. A Gen. 213 (2001) 33–45. doi:10.1016/S0926-860X(00)00877-2.

[23] E. Bagherzadeh, A. Hassan, A. Hassan, Preparation of Catalyst and Use for High Yield Conversion of Methane to Ethylene, United States Patent Application 20040220053A1, 2004.

[24] X. Tan, K. Li, Oxidative coupling of methane in a Perovskite Hollow-Fiber Membrane Reactor, Ind. Eng. Chem. Res. 45 (2006) 142–149. doi:10.1016/0926-860X(95)00098-4.

[25] F.T. Akin, Y.S. Lin, Oxidative coupling of methane in dense ceramic membrane reactor with high yields, AIChE J. 48 (2002) 2298–2306. doi:10.1002/aic.690481019.

[26] L. Olivier, S. Haag, C. Mirodatos, A.C. van Veen, Oxidative coupling of methane using catalyst modified dense perovskite membrane reactors, Catal. Today. 142 (2009) 34–41. doi:10.1016/j.cattod.2009.01.009.

[27] N.H. Othman, Z. Wu, K. Li, An oxygen permeable membrane microreactor with an in-situ deposited Bi1.5Y0.3Sm0.2O3−δ catalyst for oxidative coupling of methane, J. Memb. Sci. 488 (2015) 182–193. doi:10.1016/j.memsci.2015.04.027.

[28] O. Czuprat, T. Schiestel, H. Voss, J. Caro, Oxidative Coupling of Methane in a BCFZ Perovskite Hollow Fiber Membrane Reactor, Ind. Eng. Chem. Res. 49 (2010) 10230–10236. doi:10.1021/ie100282g.

[29] X. Tan, Z. Pang, Z. Gu, S. Liu, Catalytic perovskite hollow fibre membrane reactors for methane oxidative coupling, J. Memb. Sci. 302 (2007) 109–114. doi:10.1016/j.memsci.2007.06.033.

[30] Y. Lu, A.G. Dixon, W.R. Moser, Y.H. Ma, U. Balachandran, Oxygen-permeable dense membrane reactor for the oxidative coupling of methane, J. Memb. Sci. 170 (2000) 27–34. doi:10.1016/S0376-7388(99)00354-3.

[31] F.T. Akin, J.Y.S. Lin, Oxygen permeation through oxygen ionic or mixed-conducting ceramic membranes with chemical reactions, J. Memb. Sci. 231 (2004) 133–146. doi:10.1016/j.memsci.2003.11.012.

[32] Mleczko, Pannek, Rothaemel, Baerns, Oxidative Coupling of Methane over a La2O3/CaO Catalyst. Optimization of Reaction Conditions in a Bubbling Fluidized-bed Reactor, Can. J. Chem. Eng. 74 (1996) 279–287. doi:10.1002/cjce.5450740213.

[33] J. Sun, J. Thybaut, G. Marin, Microkinetics of methane oxidative coupling, Catal. Today. 137 (2008) 90–102. doi:10.1016/j.cattod.2008.02.026.

[34] J. Sunarso, S. Baumann, J.M. Serra, W. a. Meulenberg, S. Liu, Y.S. Lin, et al., Mixed ionic-electronic conducting (MIEC) ceramic-based membranes for oxygen separation, J. Memb. Sci. 320 (2008) 13–41. doi:10.1016/j.memsci.2008.03.074.

[35] R.M. Ormerod, Solid oxide fuel cells, Chem. Soc. Rev. 32 (2003) 17–28. doi:10.1039/b105764m.

[36] T. Ishihara, Novel electrolytes operating at 400-600 C, in: Handb. Fuel Cells Fundam. Technol. Appl. Part 2, 2003: pp. 1109–1122.

[37] G. Yin, H. Yin, M. Sun, L. Zhong, J. Zhang, R. Cong, et al., New approach to improve the conductivity of apatite-type lanthanum germanate $La_{9.33}Ge_6O_{26}$ as electrolyte for IT-SOFCs, RSC Adv. 4 (2014) 15968. doi:10.1039/C4RA00713A.

[38] Z. Bi, Y. Dong, M. Cheng, B. Yi, Behavior of lanthanum-doped ceria and Sr-, Mg-doped LaGaO3 electrolytes in an anode-supported solid oxide fuel cell with a La0.6Sr0.4CoO3 cathode, J. Power Sources. 161 (2006) 34–39.

doi:10.1016/j.jpowsour.2006.03.065.

[39] J.A. Labrincha, J.R. Frade, F.M.B. Marques, La2Zr2O7 formed at ceramic electrode/YSZ contacts, J. Mater. Sci. 28 (1993) 3809–3815. doi:10.1007/BF00353183.

[40] K. Sasaki, K. Watanabe, Y. Teraoka, Direct-Alcohol SOFCs: Current-Voltage Characteristics and Fuel Gas Compositions, J. Electrochem. Soc. 151 (2004) A965–A970. doi:10.1149/1.1756884.

Chapter 5

Oxidative coupling of methane over mixed oxide catalysts designed for solid oxide membrane reactors[1]

5.1 Summary

Oxidative coupling of methane (OCM) is a process that converts methane directly to ethane and ethylene without the intermediate steps associated with synthesis gas (CO and H_2). This technology is attractive since oxidative coupling can utilize the abundant sources of methane, however selectivity and yield to the desired C_2 products is low when conventional plug flow reactors are employed. In order to achieve higher C_2 selectivity, plug flow membrane reactors (with O^{2-} conducting membranes) can be utilized, which in principle can limit the reactions that contribute to the low selectivity to C_2 products. The optimal design of a membrane OCM reactor system would include a catalyst that is integrated with the membrane and is active and selective under the relevant operating conditions. In this chapter we have identified and tested several catalysts for OCM activity and selectivity which could be integrated into a solid oxide membrane reactor. Catalysts tested include lanthanum gallate doped with strontium and magnesium ($La_{0.8}Sr_{0.2}Ga_{0.8}Mg_{0.2}O_{3-x}$, LSGM), lanthanum manganite doped with strontium ($La_{0.8}Sr_{0.2}MnO_{3-x}$, LSM) and lanthanum strontium cobalt ferrite ($La_{0.8}Sr_{0.2}Fe_{0.8}Co_{0.2}O_{3-x}$, LSCF). We show that in packed bed reactor tests LSGM and LSGM doped with lithium

[1] The work in this chapter is also included in the following publication: Farrell, B., Linic, S., Oxidative coupling of methane over mixed oxide catalysts designed for solid oxide membrane reactors. Submitted.

reached over 90 % selectivity to C_{2+} products at high CH_4/O_2 operating ratios which are applicable to membrane reactor designs. We also show that although new phases are formed under the reaction conditions, the new phases are stable and reactive over a period of 48 hours. Further, we discuss how the LSGM catalysts might be integrated into a membrane reactor system.

5.2 Introduction

Over the past few decades, methane production has increased due to the availability of shale gas and tight oil [1,2]. Most methane produced is combusted to generate heat and power. A smaller fraction is reformed to produce synthesis gas, a mixture of CO and H_2, which is used to make chemicals and fuels including methanol, alkanes, and olefins [2]. In these indirect methane conversion processes, the methane reforming and compression account for a large fraction of the overall capital cost (60% or more) [2,3]. Therefore, there is significant interest in processes that could convert methane directly into higher value chemicals or fuels without expensive reforming steps.

Methane can be directly converted to ethane and ethylene (C_2) using oxidative coupling. The proposed mechanism of this process on most studied heterogeneous catalysts involves an extraction of a hydrogen atom from methane on a catalyst surface to form a methyl radical ($*CH_3$) [4]. The methyl radical is then released from the surface, coupling with another methyl radical in the gas phase to form ethane which can be subsequently dehydrogenated to form ethylene [5]. Water is formed as a byproduct from the extracted hydrogen and oxygen on the catalyst surface. This process was reported in the early 1980's by Keller and Bhasin and Hinsen and Baerns [6,7]. Since then, there have been a large number of catalysts tested [8]; however, few have shown product yield

and conversion that meet broadly accepted techno-economic targets of ~ 35 % yield of C_2 products (ethane and ethylene) per pass with the C_2 selectivity around 90%, at reasonably high rates using undiluted air and methane feeds [8,9]. We note that these techno-economic targets were reported in 1989 for processes converting methane to olefins, and it is possible that slightly different targets would apply today.

The reported C_2 yields in oxidative coupling of methane (OCM) are relatively low because at high operating temperatures (>873 K for most catalysts) required for the activation of strong C-H bonds in methane, CO_2 is the most thermodynamically favorable product [10]. It has been suggested that the undesired CO_2 and CO products (the C_1 products) are formed in two ways: 1) in a parallel reaction path directly from methane and oxygen via combustion and reforming reactions and 2) in sequential reactions, indirectly by further oxidation of ethane and ethylene [11]. The suggested network of reactions involved in oxidative methane coupling is shown in Scheme 1.

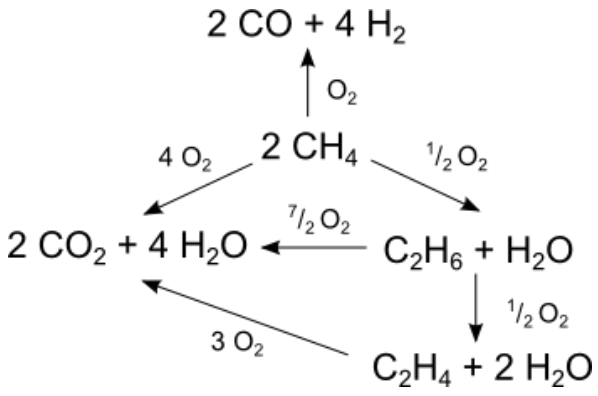

Scheme 5.1: OCM reaction network

Even a cursory analysis of the network in Scheme 1 sheds light on the difficulties associated with the design of efficient OCM chemical processes. An optimal catalyst needs to extract a hydrogen atom from methane and release the methyl radical. The catalyst needs to accomplish this task without oxidizing ethane and ethylene in sequential reactions. The activation of C-H bonds in ethane and ethylene compared to the C-H bonds in methane represents a significant constraint since the activation of C-H bonds in ethane and ethylene leads to the complete oxidation of these desired product compounds [12]. It can be easily demonstrated that reaction networks where sequential reactions lead to unselective products achieve higher yields to selective products when operated in reactors with low degree of mixing between reactants and products. Therefore, a large fraction of studies performed to date have employed plug flow reactors (PFR) with low mixing. These studies have demonstrated that alkali-promoted oxides and mixed oxides, mainly Li-MgO and $NaMnWO_3$, yielded some of the highest measured yields to C_2 products. For example, Li-MgO operated at 973-1073 K reached the C_2 yield of 18-22% with the selectivity to C_2 products of 55-65% [13], while $NaMnWO_3$ operated at temperatures higher than 1073 K reached the C_2 yields of 20-30% and the selectivity of 70-80% [14]. Furthermore, a kinetic analysis of the reactions in the network in Scheme 1, performed on an oxide catalyst (La_2O_3/CaO was used), illustrated that the reactions leading to C_1 products (CO and CO_2) exhibited approximately 1^{st} order dependence on the partial pressure of O_2, while the reactions leading to the desired C_2 products showed ½ order dependence on O_2 [11]. This kinetic information suggests that to increase the C_2 selectivity, it is important to operate at relatively low partial pressures of oxygen.

One way to achieve the above discussed optimal operating conditions of *low reactant and product mixing and low partial pressure of oxygen* is to employ membrane plug flow reactors, which allow for a controlled flux of oxygen along the length of the reactor. The main difference between conventional plug flow reactors (PFR) and a membrane plug flow reactor is that in the conventional PFR the local partial pressure of O_2 at the entrance of the reactor is high. This results in high rates of the reactions leading to the combustion products and therefore low C_2 selectivity. On the other hand, the flux of oxygen species into the membrane PFR is steady along any point in the reactor and the deep oxidation reactions can in principle be better controlled. It is important to note that at high temperatures required for activation of methane C-H bonds, membrane materials that can selectively transport only one reactant are limited to solid oxide materials. In this design, oxygen diffuses in the reactor through the solid membrane in the form of an O^{2-} ion [15].

There have been relatively few studies where solid oxide membrane reactors were employed for oxidative coupling of methane [15–19]. While these studies have demonstrated that the selectivity of C_2 products can be increased by using membrane reactors, no system has achieved the above-described techno-economic targets [17,18,20–22]. There are two major factors that have hindered the performance of membrane reactors for OCM. First, in general these systems suffer from low reactant conversion due to the relatively low flux of oxygen through the solid oxide membrane. To increase the oxygen flux, the operating temperature can be increased; however, this has a negative effect on the selectivity to the desired products. Recent advances in solid oxide fuel cell (SOFC) and oxygen separation technologies, including the development of methods to

manufacture very thin oxide membranes as well as the discovery of new membrane materials that transport oxygen anions at lower temperatures and that conduct both oxygen ions and electrons, may provide new opportunities for the development of improved oxidative coupling processes [23,24]. Another issue with membrane reactors is that many membranes have been tested without a selective OCM catalyst on the methane side of the membrane, i.e., the membrane served not only to conduct the O^{2-} ions but also to catalyze the chemical reactions. Adding a selective catalyst, tailored for OCM, to the membrane surface should increase the C_2 selectivity [20,25]. We note that optimal systems will require catalysts that are not only active and selective for OCM but also that can be seamlessly integrated with the membrane material in a functioning device.

The focus of this chapter is to test the performance of a number of potential OCM catalysts that based on their physical properties can be seamlessly integrated with state of the art solid oxide membranes. This is a necessary starting point for the development of optimal solid oxide membrane-based OCM catalytic systems. The catalysts were selected based on three criteria that make them potentially suitable for the membrane OCM systems. The first criterion was to focus on catalysts that contain elements which have shown high C_2 selectivity in previous OCM studies. In this, we were guided by the work performed by Zavyalova et al. who performed statistical analysis of published data (from over 400 references) reporting the C_2 OCM selectivites and yields of various complex multi-component catalysts. The statistical analysis suggested that in general, catalysts containing La and Mg host oxides exhibit the best performance. It also showed that the addition of a number of dopants including Ba, Sr, Mn, W, Na, Li, or Cs had a positive effect on the C_2 yield for a large fraction of catalysts [8]. Second, catalysts were chosen

for their stability and compatibility with solid oxide membrane materials at fabrication and reaction conditions. Solid oxide membranes are typically fabricated at temperatures above 1273 K to sinter the catalyst layer to the membrane surface, which is required to provide the O^{2-} ions with a direct pathway between the membrane and catalyst phases. At these processing temperatures, solid state reactions resulting in changes in the composition and properties of the membrane and catalyst materials can occur. Furthermore, it is important to have membrane and catalyst materials with similar coefficients of thermal expansion to avoid stresses on the membrane that can lead to rupture and leakage of reactants. Finally, in addition to the above mentioned requirements of high C_{2+} selectivity and stability, catalysts that exhibit high O^{2-} ionic affinity and conductivity at high temperatures were the focus of our attention. This requirement ensures that the transport of O^{2-} from membrane to the catalyst is facile.

Considering these three criteria, we narrowed our focus to lanthanum gallate oxides doped with strontium and magnesium ($La_{0.8}Sr_{0.2}Ga_{0.8}Mg_{0.2}O_{3-\delta}$ or LSGM), lanthanum manganite doped with strontium ($La_{0.8}Sr_{0.2}Mn_{0.98}O_{3-\delta}$ or LSM) and lanthanum ferrite doped with strontium and cobalt ($La_{0.6}Sr_{0.4}Co_{0.2}Fe_{0.8}O_{3-\delta}$ or LSCF). All three materials contain compositions that the above-mentioned statistical analysis suggested are promising for OCM, they are stable at elevated processing temperatures, and they are able to efficiently shuttle O^{2-} ions. Our objective was to measure the conversion-selectivity curves of the catalytic materials in OCM under different operating conditions. The measurements were performed in a plug flow packed bed reactor. We found that lanthanum gallate doped with strontium and magnesium ($La_{0.8}Sr_{0.2}Ga_{0.8}Mg_{0.2}O_{3-\delta}$, or LSGM) has the highest selectivity to C_2 products at low partial pressures of oxygen. We

also found that adding a small amount of lithium in the form of Li_2CO_3 to LSGM slightly improves its overall yield at higher oxygen partial pressures. These results suggest that LSGM is a promising as catalyst for the potential use in a solid oxide membrane reactor.

5.3 Experimental Methods, Results, and Discussion

The mixed metal oxide powders used in this study were lanthanum gallate doped with strontium and magnesium ($La_{0.8}Sr_{0.2}Ga_{0.8}Mg_{0.2}O_{3-\delta}$ or LSGM, Sigma Aldrich), lanthanum strontium manganite ($La_{0.8}Sr_{0.2}Mn_{0.98}O_{3-\delta}$ or LSM, Praxair) and lanthanum strontium cobalt ferrite ($La_{0.6}Sr_{0.4}Co_{0.2}Fe_{0.8}O_{3-\delta}$ or LSCF, Sigma Aldrich). Each powder was combined with graphite (300 mesh, Alfa Aesar) in a weight ratio of 1:0.56. The resulting powder was ground by hand using a mortar and pestle then pelletized into cylinders that were 6 mm in diameter and 3.5 mm in length. The carbon was then burned out of the catalyst pellets at 1273 K for 4 hr (ramp rate of 2 K/min) to create porous catalyst pellets weighing 0.11 g each. Lithium was added in the form of Li_2CO_3 (99+%, Acros Organics) to some of the LSGM catalysts in an aqueous solution and dried at 348 K, resulting in catalysts that are 1% Li by weight. Table 5.1 shows the BET surface area and the median particle diameter for the powders used in this study. Due to the fact that these catalysts are designed to be sintered at high temperatures into self-supporting porous structures that can be integrated in membrane reactors, the particle sizes are large and the surface areas are relatively low.

Table 5.1: BET surface area and particle size for the catalysts used in this study

	BET surface area (m^2/g)	Particle size d50 (μm)
LSGM	4	0.8
LSCF	5.5	0.4
LSM	4.77	1.1

For each experiment, a catalyst pellet was loaded into a ¼" inner diameter alumina tube resulting in a total catalyst weight of 0.11 g. Silica wool was added to both sides of the tube to prevent movement of the catalyst pellet. The alumina tube was placed in a horizontal tube furnace and heated under Ar flow to 1023-1123 K at 2 K/min. After reaching the reaction temperature, the catalysts were held under Ar flow for ~8 hours before air and a certified mixture of 95% CH_4 and 5% He (Cryogenic Gases) were fed using mass flow controllers. The outlet gas was analyzed using a Varian CP 3800 gas chromatography system (GC) equipped with two thermal conductivity detectors and a flame ionization detector. All measured peak areas were compared to gas calibration standards (SCOTTY, Cryogenic Gases) to determine the outlet gas concentrations. Prior to catalyst testing, the system was operated without catalyst to determine the role of gas phase reactions and reactions due to the tube walls and silica wool. At a O_2:CH_4:Inert molar ratios of 1:3:4 (where the inert gas is a mixture of N_2 from air and He from the methane mixture) and a total flow rate of 100 sccm, the methane conversion without catalyst was 1.3% and 4.1% at 1023 K and 1073 K, respectively. This conversion is approximately 5 % of the conversion obtained using the catalysts at 1023 K, and it does not impact the results reported below.

X-ray diffraction (XRD) was performed using a Rigaku MiniFlex spectrometer. This instrument uses a Cu Kα X-ray source with a graphite monochromator. Data was acquired at a tube voltage and current of 40 kV and 15 mA. XRD patterns were collected with a continuous sweep from 2Θ of 20-80 at a rate of 2 2Θ/min. Phases were identified using the assistance of Jade software.

The data in Figure 5.1 show the C_{2+} (ethane, ethylene, propane, and propylene) selectivity and yield as a function of methane conversion and CH_4/O_2 ratio for the tested catalysts. Methane conversion, C_{2+} selectivity, and C_{2+} yield were based on molar fractions in the outlet gas and calculated using the following equations:

$$X_{CH4} = \frac{CO_2 + CO + 2C_2H_6 + 2C_2H_4 + 3C_3H_8 + 3C_3H_6}{CH_4 + CO_2 + CO + 2C_2H_6 + 2C_2H_4 + 3C_3H_8 + 3C_3H_6} \quad 5.1$$

$$S_{C2+} = \frac{2C_2H_6 + 2C_2H_4 + 3C_3H_8 + 3C_3H_6}{CO_2 + CO + 2C_2H_6 + 2C_2H_4 + 3C_3H_8 + 3C_3H_6} \quad 5.2$$

$$Y_{C2+} = X_{CH4} * S_{C2+} \quad 5.3$$

The temperature at the inlet of the reactor was 1023 K, and the total inlet flow rate of the air and methane mixture was held constant at 100 sccm. The conditions yielded approximately equivalent space and weight hourly space velocities for all the tested materials. The CH_4/O_2 molar ratios at the inlet of the reactor were between 0.8 and 160. We note that for the sake of completeness we probed the behavior of the system under some extreme CH_4/O_2 molar ratios (i.e., as high as 160). Although the yields at these conditions are quite low in a packed bed reactor, these ratios were included in our tests since the partial pressure of oxygen in solid oxide membrane reactors can be very low.

We note that in packed bed reactors the C_2 yield typically reaches a maximum at a CH_4/O_2 ratio of ~ 3 [13]. The tested range of molar flow rate ratios allowed for the manipulation of methane conversion up to ~ 65 % for the given set of operating conditions. We found that over this range of CH_4/O_2 molar ratios, oxygen was always the limiting reactant. Oxygen consumption was above 82% in all experiments, and above 90% in most experiments. The catalysts were tested at each reaction condition multiple times over the course of 48 hours. The error bars represent the standard error (the standard deviation of the measurements divided by the square root of the number of measurements) of the measurements at each reaction condition.

The data in Figure 5.1 show that the LSGM and 1% Li-LSGM catalysts had selectivity to the C_{2+} products of ~ 90%, achieved at the lowest CH_4 conversions, which corresponded to the highest CH_4/O_2 molar ratios. As the conversion increased (corresponding to a decrease in the CH_4/O_2 molar ratio), the selectivity to C_{2+} products decreased. The data in Figure 5.1 show that the yield of C_{2+} products for the LSGM catalysts reached a maximum of ~ 10% at the CH_4 conversion of 28% and (CH_4/O_2 molar ratio of 3). This yield was slightly increased to over 11% for the LSGM catalysts when 1 wt% Li was added. The selectivity-conversion curves in Figure 5.1 for LSM show similar trends as those observed for LSGM; however, the C_{2+} yields and selectivity were considerably lower. For example, the highest C_{2+} selectivity for LSM was ~ 6.0% observed at high CH_4/O_2 ratio and low CH_4 conversion. On the other hand, LSCF showed slightly different behavior with very low C_{2+} selectivity (approaching zero) at low conversion (high CH_4/O_2 ratio). As the conversion increased and the CH_4/O_2 ratio

decreased, the selectivity to C_{2+} products increased to a maximum of ~ 4.5% and then decreased at higher conversion.

The data in Figure 5.2 show the selectivity of each product as a function of the conversion and CH_4/O_2 ratio for tested catalysts. This data gives insights into the mechanism of the reaction on each catalyst. On the LSGM and Li-LSGM catalysts, ethane selectivity was high at low conversion (high CH_4/O_2 ratio) and decreased with increasing CH_4 conversion. The selectivity of ethylene, CO, and the C_3 products went through a maximum as a function of an increasing CH_4 conversion. On the other hand, CO_2 selectivity was low at low conversion (high CH_4/O_2 ratio), and increased as the CH_4 conversion increased. These trends indicate that on LSGM and Li-LSGM, ethane is the primary product, and the main pathway leading to the combustion products includes the sequential oxidation of ethane. The data for the LSM catalyst show that similar to LSGM, the ethane selectivity decreased as the conversion increased. However, unlike LSGM there were also large amounts of the deeper oxidation products (CO and CO_2) produced at low conversion and high CH_4/O_2 ratios. This indicates that the deep oxidation reactions, triggered by the activation of C-H bonds in methane, ethane, and ethylene, are more facile on this material compared to LSGM. In contrast, the LSCF catalyst had very high selectivity to CO and no selectivity to ethane at low conversion (high CH_4/O_2 ratio). This behavior of LSCF suggests that compared to the other tested materials the direct CH_4 partial oxidation to CO and H_2 is a more dominant unselective pathway for this material. In general, we postulate that the low selectivity exhibited by LSCF and LSM is likely due to the presence of transition metals (particularly Co and Fe)

in the catalysts. These transition metals are effective catalysts for the deeper oxidation of hydrocarbons.

The catalyst testing demonstrated that the LSGM and Li-LSGM catalysts produced the highest C_{2+} yields. To further understand the effect of the reaction conditions on the catalysts, we varied the reactor temperature. The data in Figure 5.3 a and b show the yield of the combined C_{2+} products (ethane, ethylene, propane and propylene) at operating temperatures between 1023 K and 1123 K for the O_2:CH_4:Inert ($He+N_2$) molar ratio of 1:3:4 with a total flow rate of 100 sccm for the LSGM and Li-promoted LSGM catalysts. These are the conditions that resulted in the highest C_{2+} yields. While the Li doped catalysts exhibit slightly improved performance, the overall yield of C_{2+} products for both catalysts decreases with increased temperature. Furthermore, the ethylene/ethane ratio increased as the operating temperature increased. These results are consistent with the sequential reactions occurring where ethane reacts with oxygen to form ethylene and unselective C_1 products (CO_2 and CO).

For catalysts containing Li, the stability of the catalyst is an important factor because Li can be lost over time when it is converted to LiOH in the presence of oxygen. Figure 5.4 shows data from a stability test of the 1% Li-LSGM catalyst over 48 hours of constant reaction conditions of 1073 K with a O_2:CH_4:Inert ($He+N_2$) ratio of 1:3:4 and a total flow rate of 100 sccm. The data show that the catalyst was stable over 48 hours under these conditions with little change in conversion of CH_4 or the yield and selectivity of C_{2+} products.

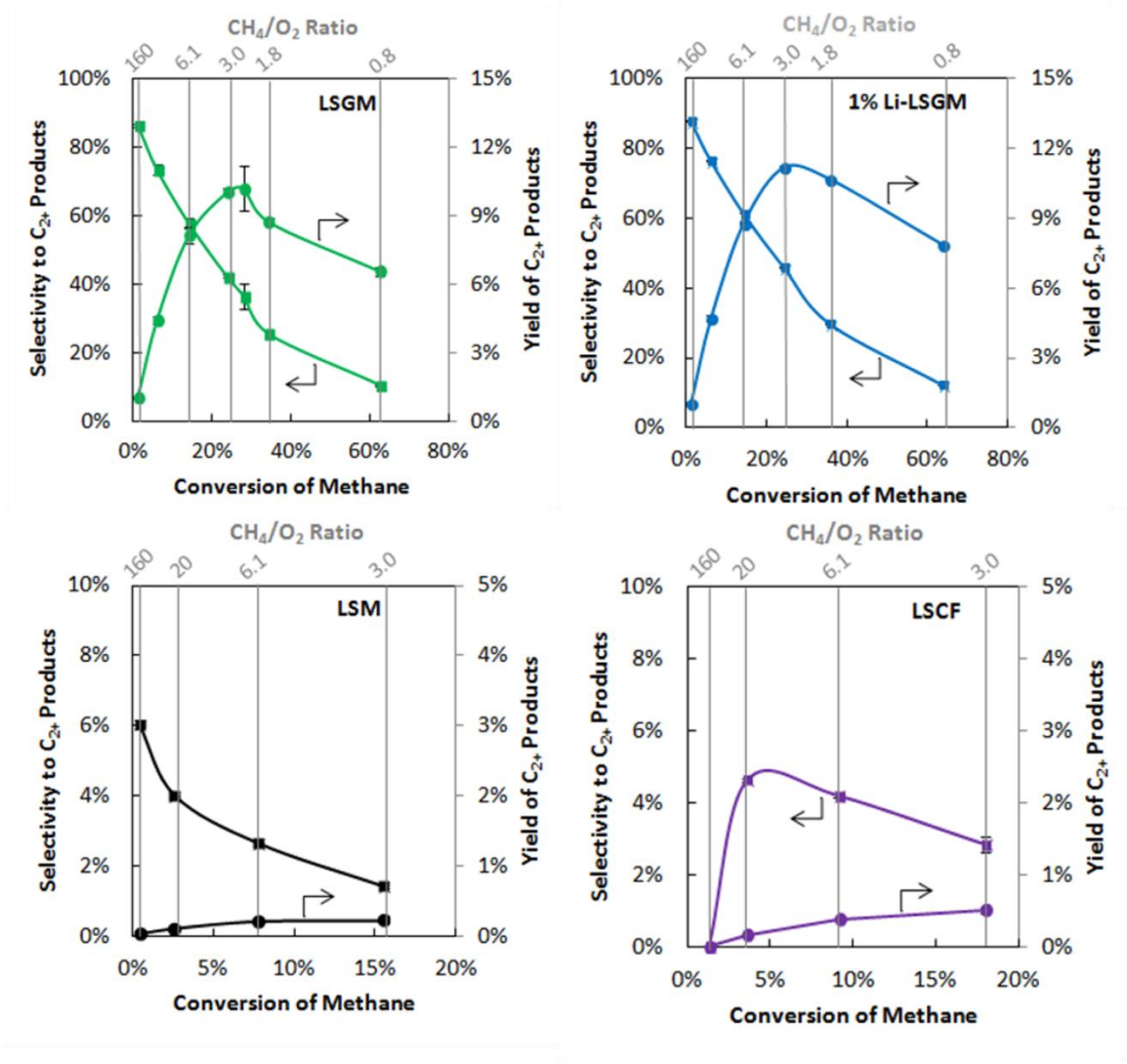

Figure 5.1: Selectivity and yield of C_{2+} products for each catalyst tested at 1023 K with a total inlet flow rate of 100 sccm. Lines are included to guide the eye.

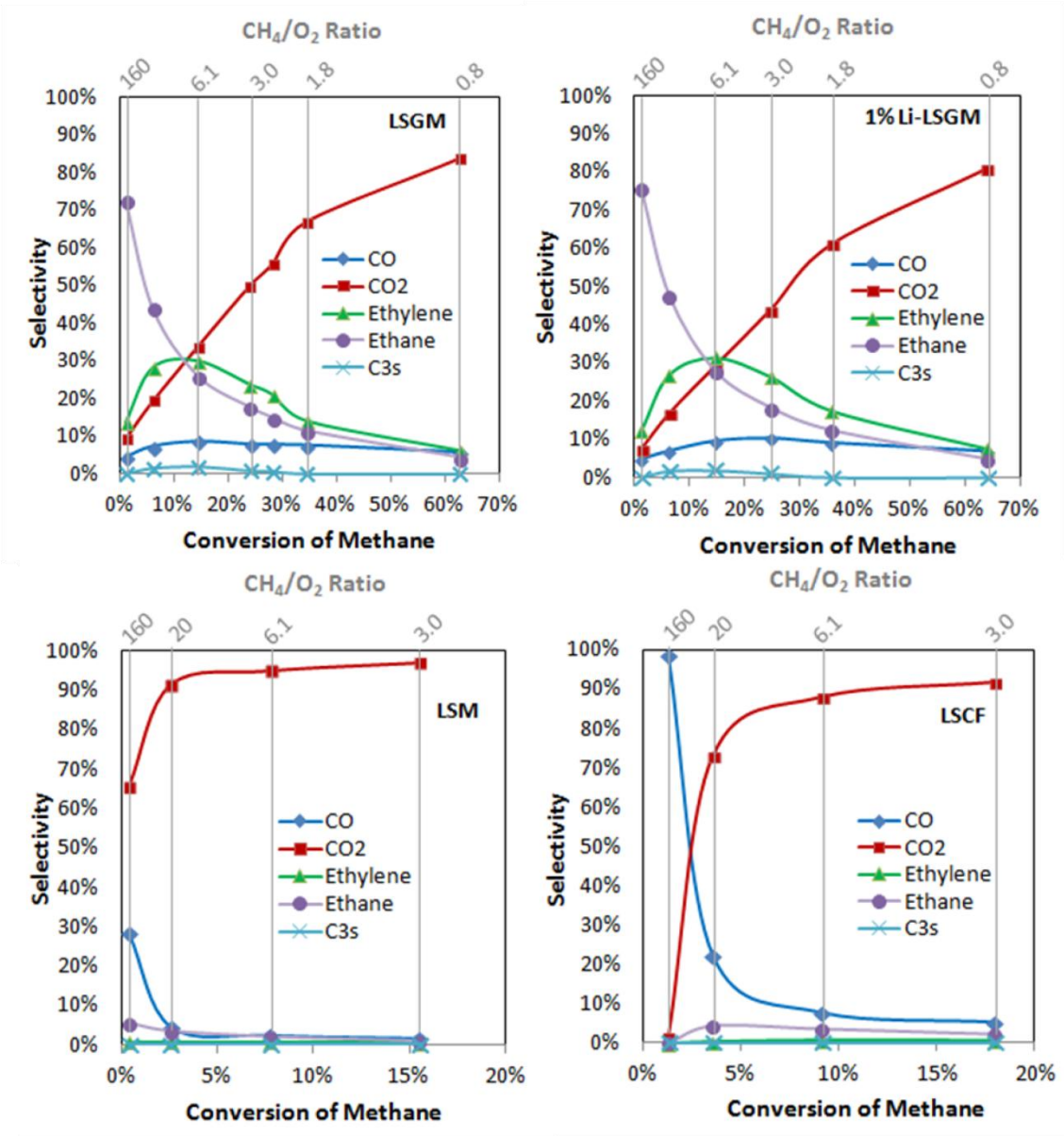

Figure 5.2: Selectivity of CO (diamonds), CO_2 (squares), Ethylene (triangles), Ethane (circles), and C_3 products (x) as a function of methane conversion and CH_4/O_2 ratio for LSGM, 1% Li-LSGM, LSCF, and LSM catalysts. Lines are included to guide the eye.

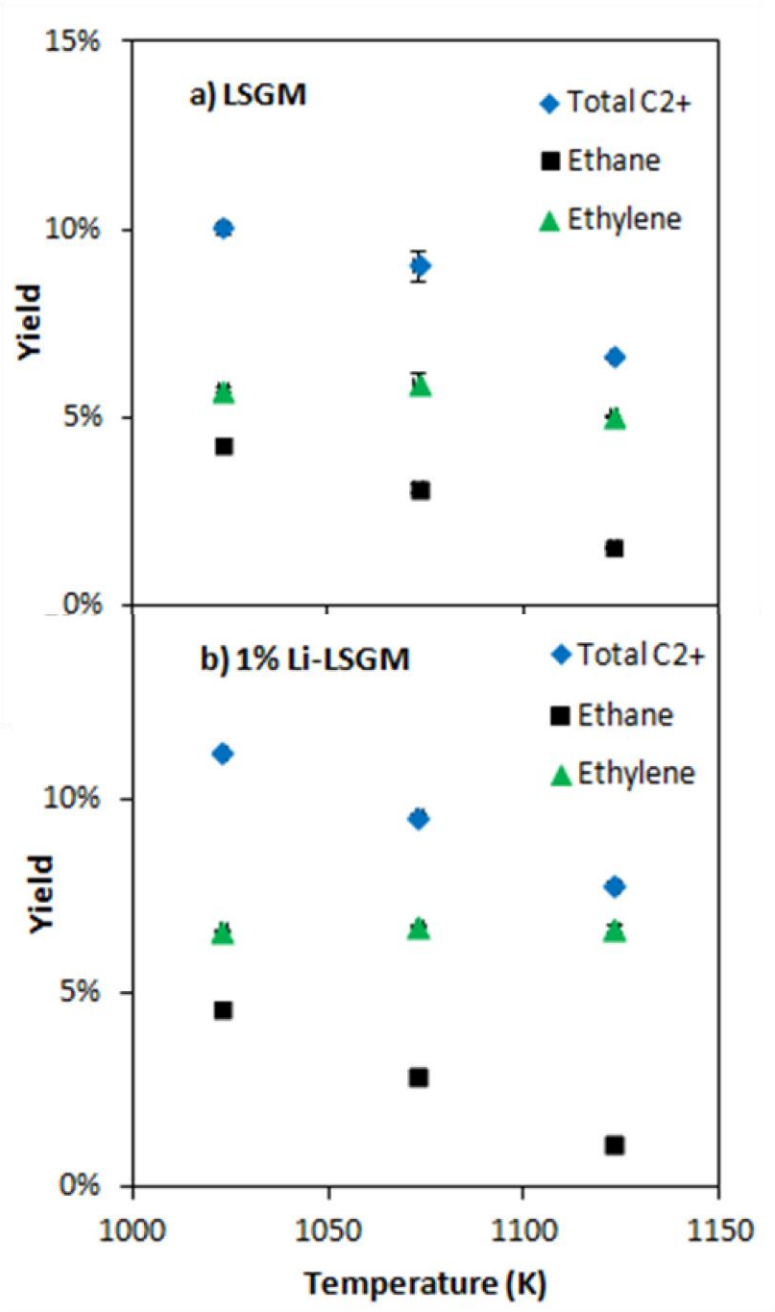

Figure 5.3: Effect of temperature on the overall yield of C_{2+} products and on the yields of ethane and ethylene for LSGM and 1% Li-LSGM catalyst operating at O_2:CH_4:Inert ($He+N_2$) ratio of 1:3:4 and total flow rate of 100 sccm: a) LSGM b) 1% Li-LSGM

We have also characterized fresh and used LSGM and 1% Li-LSGM catalysts using XRD. The data in Figure 5.5 show the normalized X-ray diffraction pattern of fresh LSGM (Fig. 5.5a), LSGM after heating to 1073 K and cooling back to room temperature in Ar gas (Fig. 5.5b), and the LSGM catalyst after it has been under reaction conditions at 1073 K for 48 hours (Fig. 5.5c). Comparison between the diffraction spectra in Figures 5.5a, 5.5b, and 5.5c shows that there are new features that appear in the XRD spectra of the pretreated and used catalysts. We have assigned the new features to $SrLaGaO_4$ and carbon deposits. There are several peaks that we were unable to assign, including a peak at 2Θ of 29.7 that appears in both of the catalysts that have been exposed to methane as well as the LSGM when heated in Ar. $SrLaGaO_4$ can be formed when the LSGM is held under reducing conditions at high temperatures [26]. The presence of this impurity phase indicates that the LSGM was partially reduced. The appearance of the new phases after the thermal treatment in an inert environment in Figure 5.5b suggests that this new phase is not the result of the catalyst operation at the reaction condition, but rather it is a consequence of the thermal reduction of the material. It is important to point out that the conversion and selectivity were stable (at least for 48 hours, the period over which our testing was performed). The data in Figure 5.5d show X-ray diffraction patterns for the 1% Li-LSGM catalyst after it has been heated in Ar to 1073 K and cooled down to room temperature, while the data in Figure 5.5e show the diffraction pattern of 1% Li-LSGM after its operation at the reaction conditions at 1073 K for 48 hours. The two catalysts doped with Li show the same $SrLaGaO_4$ phase that appeared in the LSGM, along with two new phases that we have assigned as $La_4Ga_2O_9$

and $SrLaGa_3O_7$. Comparison of Figure 5.5d and Figure 5.5e show that these phases are formed during the thermal reduction of the material (in argon), and that the materials is otherwise stable at the reaction conditions over 48 hours. As shown in Figure 5.4, the selectivity and conversion are steady over this period of time for 1% Li-LSGM.

The data presented above show that LSGM and 1% Li-LSGM are highly selective towards the C_{2+} products at high CH_4/O_2 ratios and low methane conversion. In addition, this material has several other characteristics that make it potentially useful as a catalyst and/or membrane material in solid oxide membrane OCM reactors. First, when compared to other O^{2-} ion conducting materials, LSGM has relatively high O^{2-} ionic conductivity of ~ 0.17 S/cm at 1073 K [23,27]. Therefore, LSGM should be able to accept oxygen anions directly from a membrane and rapidly transfer them to the active centers where the reactions are taking place. Therefore the diffusion of ions through the catalyst in a solid oxide membrane device should not be an issue. The high ionic conductivity of LSGM also suggests that this material could serve a dual role, acting as the catalyst and membrane. Using LSGM as both the membrane and catalyst material has the advantage of avoiding high temperature reactions between dissimilar materials that commonly occur at the temperatures used to create solid oxide membrane devices. Furthermore, in this design thermal stresses that are the consequence of the difference in the thermal expansion coefficients of the catalyst and membrane materials can be minimized. To use LSGM as both a catalyst and membrane material, it will be necessary to provide a way to balance the charge of the system. We note that LSGM transports oxygen in the form O^{2-} ion and to achieve high ion conductivity, which is required to achieve high overall conversion, it is necessary to provide electronic pathways between

the oxygen and methane sides of the membrane. This can be done in a few ways: 1) An external electronic connection could be employed to connect the two sides of the membrane, or 2) LSGM can be doped with Mn, Ni, Co, or Fe to induce electronic conductivity into the membrane itself [28]. Both of these methods have advantages and disadvantages. For the external circuit method, an advantage is that the electronic potential difference across the membrane can be controlled, with the option of increasing the oxygen flux electrochemically. A disadvantage is that in order to make a circuit, there must be an electronically conductive material on the methane side which may decrease the selectivity of the overall system. In the case where the membrane itself is electronically conductive, an advantage would be that the system is relatively simple, but the disadvantages are that there is no control over the oxygen flux through the membrane. Furthermore, adding transition metals to LSGM will likely decrease the selectivity of the material to C_{2+} products as these metals are very efficient in performing complete and partial oxidation reactions [29,30].

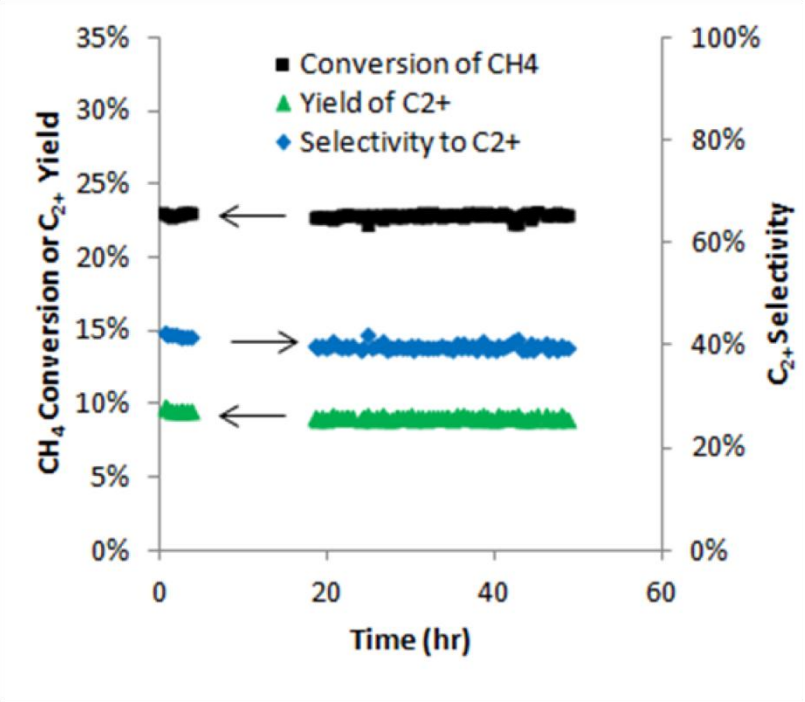

Figure 5.4: Stability of 1% Li-LSGM catalyst at 1073 K and O_2:CH_4:Inert molar ratio of 1:3:4 at a total of 100 sccm.

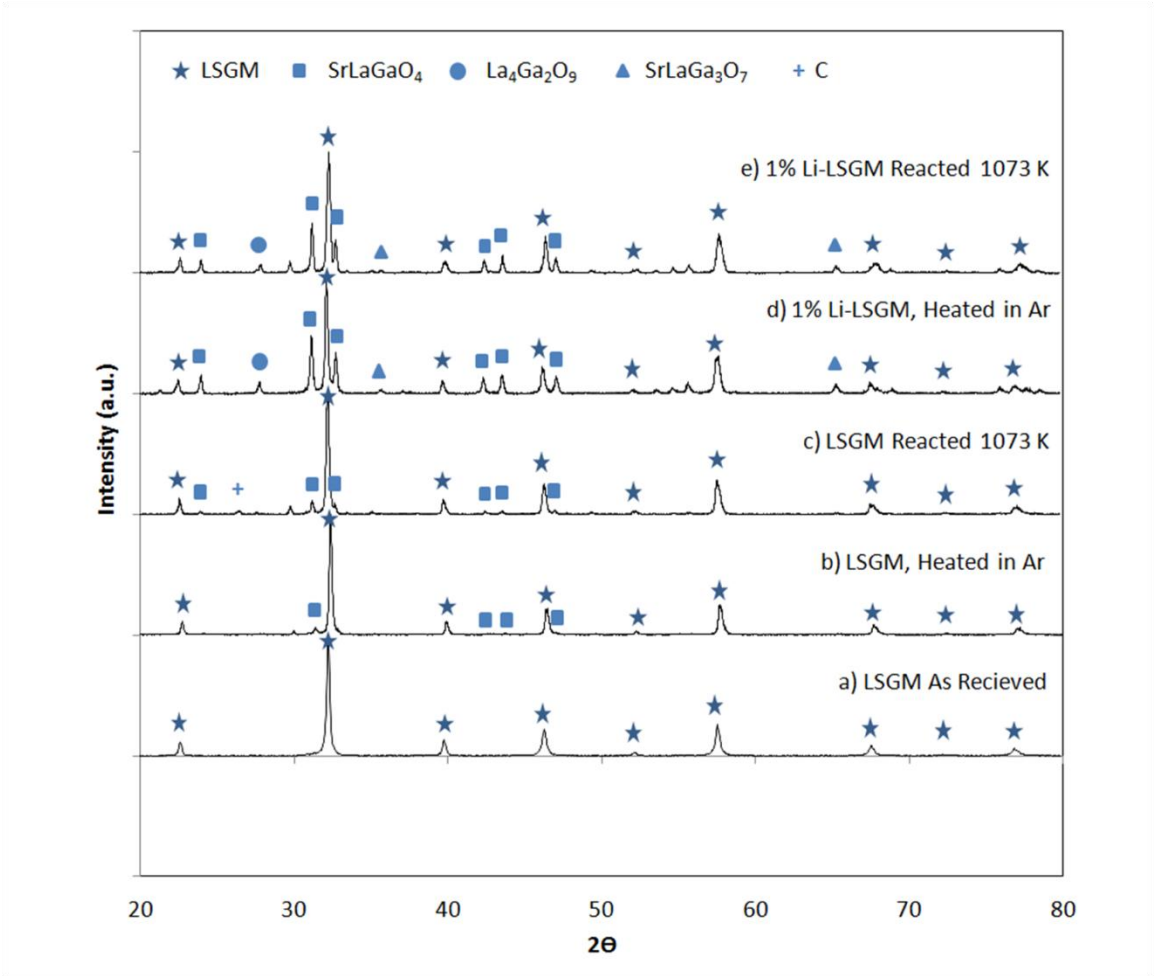

Figure 5.5: X-ray diffraction patterns for LSGM catalysts: a) LSGM as received, b) LSGM after heating to 1073 K in Ar c) LSGM after reaction at 1073 K for 48 hours, d) 1% Li-LSGM after heating to 1073 K in Ar, e) 1% Li-LSGM after reaction at 1073 K for 48 hours

Another option would be to use LSGM as a catalyst material in conjunction with a different membrane material that exhibits electronic and ionic conductivities. While there are many solid oxide membrane materials that offer mixed ionic and electronic conductivities [24], the material choice will need to be carefully considered. It is usually required to heat the solid oxide components to temperatures in excess of 1273 K in order to achieve good electronic contact between the membrane and catalyst materials. At these temperatures, it is well known that LSGM can react with the components of many mixed ion-electron conducting oxide materials that could serve as membranes including ceria, zirconia, and LSCF [31,32], The high temperature solid state reactions result in migration of the metals and new phases between the materials, and the new materials that are formed may or may not have the desired conductive and catalytic properties necessary for a membrane reactor. For example, when lanthanum and zirconium based materials are used in the same device, lanthanum zirconates can be formed [32]. This material can block the transfer of O^{2-} across the membrane leading to the loss of methane conversion.

5.4 Conclusions

In conclusion, we have demonstrated that LSGM and 1% Li-LSGM are active and selective as catalysts for oxidative coupling of methane. In packed bed reactor tests, these materials reached over 90 % selectivity to the C_{2+} products at high CH_4/O_2 operating ratios which are applicable to membrane reactor designs. We have shown that although these materials undergo thermal reduction due to the reducing operating conditions, characterized by high operating temperatures and CH_4/O_2 ratios, the new phases that are formed are stable and reactive. Overall, our results indicate that LSGM

and 1% Li-LSGM are promising candidates for catalysts to be used in conjunction with a membrane reactor for oxidative coupling of methane.

5.5 References

[1] BP Energy Outlook 2035, 2014.

[2] E. McFarland, Unconventional Chemistry for Unconventional Natural Gas, Science (80-.). 338 (2012) 340–342. doi:10.1126/science.1226840.

[3] K. Aasberg-Petersen, C.S. Nielsen, I. Dybkjær, J. Perregaard, Large Scale Methanol Production from Natural Gas, n.d. http://www.topsoe.com/business_areas/methanol/~/media/PDF files/Methanol/Topsoe_large_scale_methanol_prod_paper.ashx.

[4] J.H. Lunsford, Catalytic conversion of methane to more useful chemicals and fuels: A challenge for the 21st century, Catal. Today. 63 (2000) 165–174. doi:10.1016/S0920-5861(00)00456-9.

[5] L. Luo, X. Tang, W. Wang, Y. Wang, S. Sun, F. Qi, et al., Methyl Radicals in Oxidative Coupling of Methane Directly Confirmed by Synchrotron VUV Photoionization Mass Spectroscopy., Sci. Rep. 3 (2013) 1625. doi:10.1038/srep01625.

[6] G. Keller, M. Bhasin, Synthesis of ethylene via oxidative coupling of methane I. Determination of active catalysts, J. Catal. 73 (1982) 9–19. doi:10.1016/0021-9517(82)90075-6.

[7] W. Hinsen, M. Baerns, Oxidative coupling of methane to C2 hydrocarbons in the presence of different catalysts, Chem. Zeitung. 107 (1983) 223–226.

[8] U. Zavyalova, M. Holena, R. Schlögl, M. Baerns, Statistical analysis of past catalytic data on oxidative methane coupling for new insights into the composition

of high-performance catalysts, ChemCatChem. 3 (2011) 1935–1947. doi:10.1002/cctc.201100186.

[9] J.C.W. Kuo, C.T. Kresge, R.E. Palermo, Evaluation of Direct Methane Conversion to Higher Hydrocarbons and Oxygenates, Catal. Today. 4 (1989) 463–470.

[10] Q. Zhu, S.L. Wegener, C. Xie, O. Uche, M. Neurock, T.J. Marks, Sulfur as a selective "soft" oxidant for catalytic methane conversion probed by experiment and theory., Nat. Chem. 5 (2013) 104–109. doi:10.1038/nchem.1527.

[11] Z. Stansch, L. Mleczko, M. Baerns, Comprehensive Kinetics of Oxidative Coupling of Methane over the La_2O_3/CaO Catalyst, Ind. Eng. Chem. Res. 36 (1997) 2568–2579. doi:10.1021/ie960562k.

[12] P. Tang, Q. Zhu, Z. Wu, D. Ma, Methane Activation: The past and future, Energy Environ. Sci. 7 (2014) 2580–2591. doi:10.1039/c4ee00604f.

[13] S. Arndt, G. Laugel, S. Levchenko, R. Horn, M. Baerns, M. Scheffler, et al., A Critical Assessment of Li/MgO-Based Catalysts for the Oxidative Coupling of Methane, Catal. Rev. 53 (2011) 424–514. doi:10.1080/01614940.2011.613330.

[14] S. Arndt, T. Otremba, U. Simon, M. Yildiz, H. Schubert, R. Schomäcker, Mn-Na 2WO 4/SiO 2 as catalyst for the oxidative coupling of methane. What is really known?, Appl. Catal. A Gen. 425-426 (2012) 53–61. doi:10.1016/j.apcata.2012.02.046.

[15] D. Eng, M. Stoukides, Catalytic and Electrocatalytic Methane Oxidation with Solid Oxide Membranes, Catal. Rev. 33 (1991) 375–412. doi:10.1080/01614949108020304.

[16] E.A. Hazbun, Ceramic Membrane for Hydrocarbon Conversion, 4791079, 1986.

[17] X. Tan, Z. Pang, Z. Gu, S. Liu, Catalytic perovskite hollow fibre membrane reactors for methane oxidative coupling, J. Memb. Sci. 302 (2007) 109–114. doi:10.1016/j.memsci.2007.06.033.

[18] Y. Lu, A.G. Dixon, W.R. Moser, Y.H. Ma, U. Balachandran, Oxygen-permeable dense membrane reactor for the oxidative coupling of methane, J. Memb. Sci. 170 (2000) 27–34. doi:10.1016/S0376-7388(99)00354-3.

[19] O. Czuprat, T. Schiestel, H. Voss, J. Caro, Oxidative Coupling of Methane in a BCFZ Perovskite Hollow Fiber Membrane Reactor, Ind. Eng. Chem. Res. 49 (2010) 10230–10236. doi:10.1021/ie100282g.

[20] L. Olivier, S. Haag, C. Mirodatos, A.C. van Veen, Oxidative coupling of methane using catalyst modified dense perovskite membrane reactors, Catal. Today. 142 (2009) 34–41. doi:10.1016/j.cattod.2009.01.009.

[21] N.H. Othman, Z. Wu, K. Li, An oxygen permeable membrane microreactor with an in-situ deposited $Bi_{1.5}Y_{0.3}Sm_{0.2}O_{3-\delta}$ catalyst for oxidative coupling of methane, J. Memb. Sci. 488 (2015) 182–193. doi:10.1016/j.memsci.2015.04.027.

[22] F.T. Akin, Y.S. Lin, Oxidative coupling of methane in dense ceramic membrane reactor with high yields, AIChE J. 48 (2002) 2298–2306. doi:10.1002/aic.690481019.

[23] T. Ishihara, Novel electrolytes operating at 400-600 C, in: Handb. Fuel Cells Fundam. Technol. Appl. Part 2, 2003: pp. 1109–1122.

[24] J. Sunarso, S. Baumann, J.M. Serra, W. A. Meulenberg, S. Liu, Y.S. Lin, et al., Mixed ionic-electronic conducting (MIEC) ceramic-based membranes for oxygen separation, J. Memb. Sci. 320 (2008) 13–41. doi:10.1016/j.memsci.2008.03.074.

[25] N.H. Othman, Z. Wu, K. Li, An oxygen permeable membrane microreactor with an in-situ deposited $Bi_{1.5}Y_{0.3}Sm_{0.2}O_{3-\delta}$ catalyst for oxidative coupling of methane, J. Memb. Sci. 488 (2015) 182–193. doi:10.1016/j.memsci.2015.04.027.

[26] E. Djurado, M. Labeau, Second phases in doped lanthanum gallate perovskites, J. Eur. Ceram. Soc. 18 (1998) 1397–1404. doi:10.1016/S0955-2219(98)00016-8.

[27] S.P.S. Badwal, S. Giddey, C. Munnings, a. Kulkarni, Review of progress in high temperature solid oxide fuel cells, J. Aust. Ceram. Soc. 50 (2014) 23–37.

[28] T. Ishihara, T. Yamada, H. Arikawa, H. Nishiguchi, Y. Takita, Mixed electronic – oxide ionic conductivity and oxygen permeating property of Fe- , Co- or Ni-doped $LaGaO_3$ perovskite oxide, Solid State Ionics. 135 (2000) 631–636. doi:10.1246/cl.1999.1257.

[29] E. Nikolla, J. Schwank, S. Linic, Hydrocarbon steam reforming on Ni alloys at solid oxide fuel cell operating conditions, Catal. Today. 136 (2008) 243–248. doi:10.1016/j.cattod.2008.03.028.

[30] E. Nikolla, J. Schwank, S. Linic, Comparative study of the kinetics of methane steam reforming on supported Ni and Sn/Ni alloy catalysts: The impact of the formation of Ni alloy on chemistry, J. Catal. 263 (2009) 220–227. doi:10.1016/j.jcat.2009.02.006.

[31] Z. Bi, Y. Dong, M. Cheng, B. Yi, Behavior of lanthanum-doped ceria and Sr-, Mg-doped $LaGaO_3$ electrolytes in an anode-supported solid oxide fuel cell with a $La_{0.6}Sr_{0.4}CoO_3$ cathode, J. Power Sources. 161 (2006) 34–39. doi:10.1016/j.jpowsour.2006.03.065.

[32] J.A. Labrincha, J.R. Frade, F.M.B. Marques, $La_2Zr_2O_7$ formed at ceramic electrode/YSZ contacts, J. Mater. Sci. 28 (1993) 3809–3815. doi:10.1007/BF00353183.

Chapter 6

Oxidative coupling of methane using oxygen permeable solid oxide membrane reactors with Li-LSGM catalyst

6.1 Summary

Oxidative coupling of methane is a process that converts methane directly to ethane and ethylene, as discussed in previous chapters. In this chapter, lanthanum gallate doped with strontium and magnesium ($La_{0.8}Sr_{0.2}Ga_{0.8}Mg_{0.2}O_{3-x}$, LSGM) was doped with 1% Li and tested as a catalyst material for the oxidative coupling of methane in membrane reactors. Small disk shaped membrane supported reactors were fabricated from $La_{0.6}Sr_{0.4}Co_{0.2}Fe_{0.8}O_{3-\delta}$ (LSCF) and $La_{0.8}Sr_{0.2}Ga_{0.8}Mg_{0.2}O_{3-\delta}$ (Ni-LSGM), with porous air and methane catalysts on either side. Characterization of the physical and chemical properties of the reactors showed good contact between the layers of each reactor, however there was some transfer of cobalt between the layers. In both types of membrane reactor, the selectivity to ethane and ethylene ($C_{2+)}$ products was above 90% at 1073 K despite the presence of transition metals in the membranes. The highest methane conversion achieved in the reactors at 1073 K was 1.8% with a C_{2+} yield of 1.6%, however the conversion declined over time. The decline in conversion was likely due to carbon deposition on the surface of the methane catalyst, and the presence of carbon was confirmed by XRD.

6.2 Introduction

As described in Chapters 4 and 5, the oxidative coupling of methane (OCM) can be used to generate ethane and ethylene directly from methane over metal oxide catalysts. Although this process has been studied extensively since the first reports by Keller and Bhasin and Hinsen and Baerns in the 1980's [1,2], there are still no commercial chemical plants operating using this technology because of the low single pass yields of C_2 products (ethane and ethylene). In order to obtain higher C_2 yields, a different approach needs to be taken that deviates from testing catalysts in packed bed reactors.

A different type of reactor that is well suited to OCM is a solid oxide membrane reactor that selectively allows oxygen across the membrane as O^{2-} [3]. Although these reactors are typically used for solid oxide fuel cells and oxygen separation from air, they also have properties that make them useful for OCM. First, they operate at the high temperatures (973-1273 K) required to activate methane on metal oxide catalysts. Additionally, when shaped into tubes and operated under plug flow conditions, this type of reactor has much higher theoretical yields than packed bed reactors operating with the same catalyst under similar conditions. The increase in yield compared to packed bed reactors is due to the distribution of oxygen along the length of the reactor which favors C_2 coupling reactions over deeper oxidation reactions that form the unselective products CO and CO_2 (CO_x).

Out of the thousands of publications, patents, and reports of OCM, there are relatively few studies performed using solid oxide membrane reactors. These studies have shown that dense, gas tight, solid oxide membrane reactors can be fabricated using a variety of solid oxide materials including $La_{0.6}Sr_{0.4}Co_{0.2}Fe_{0.8}O_{3-\delta}$ (LSCF) [4],

$Bi_{1.5}Y_{0.3}Sm_{0.2}O_{3-\delta}$ (BYS) [5], and $BaCe_{0.8}Gd_{0.2}O_3$ (BCG) [6], and that adding a selective catalyst material to the methane side of the membrane is beneficial to the yield of the reactor [7,8]. In a recent publication, Othman et al. showed that a LSCF membrane reactor coupled with a BYS catalyst reached a yield of 39% and selectivity of 79% to C_2 products at 1173 K [8], which represents one of the highest single pass yields reported in any type of OCM reactor. Although this is a promising result, in this reactor study the methane flow was diluted to ~10% methane. This type of dilution is typical in membrane reactor studies [4,9–12] in order to increase the conversion of methane and decrease carbon poisoning on the surface of the catalyst. However, this dilution would be unrealistic for a commercial process because the diluent gas would need to be separated from the products, which would be an expensive process. In order to show commercial viability, membrane reactors should be tested at realistic operating conditions with a high concentration of methane.

One catalyst that is promising for use in membrane reactors is $La_{0.8}Sr_{0.2}Ga_{0.8}Mg_{0.2}O_{3-\delta}$ (LSGM) doped with a small amount of Li [13]. This catalyst has high selectivity to C_{2+} products at high methane to oxygen ratios [13] as well as high ionic conductivity [14], allowing it to accept oxygen anions directly from the membrane. LSGM does not have electronic conductivity, and therefore in order to use 1% Li-LSGM as a methane side catalyst, a membrane with ionic and electronic conductivity is required to return the electrons to the air side catalyst. In this work, membrane reactors were fabricated and tested using 1% Li-LSGM as the methane side catalyst, LSCF or Ni-LSGM as the membrane material, and LSCF as the air side catalyst. It is important to note that the objective of this study was not to achieve the highest yield possible, but to

understand the interactions between the reactor materials, and test the catalyst under realistic membrane reactor operating conditions. To achieve this, the reactors were characterized for both their structure and elemental composition, and tested using high concentrations of methane. Overall, the selectivity to C_{2+} products was high (~90%) but the small surface area of the reactors limited the conversion of methane and the overall yield of C_{2+} products. There was also a significant decrease in the conversion over time, which was due, at least in part, to carbon accumulation on the surface of the catalyst.

6.3 Experimental Methods

6.3.1 Membrane and Reactor Fabrication

The membrane reactors used in this study were membrane supported, where the membrane material provided the structure of the reactor. $La_{0.6}Sr_{0.4}Co_{0.2}Fe_{0.8}O_{3-\delta}$ (LSCF) and Ni doped $La_{0.8}Sr_{0.2}Ga_{0.8}Mg_{0.2}O_{3-\delta}$ (Ni-LSGM) were tested as membrane materials. LSCF has electronic and ionic conductivity, and was used as received from Sigma Aldrich. LSGM was doped with Ni in order to give electronic conductivity to LSGM [15], which is ionically conductive, but has negligible electronic conductivity. Ni was added to the LSGM in the form of NiO to order to dope the Ga sites with ~15% Ni. To synthesize the Ni-LSGM, LSGM (Sigma Aldrich) and NiO (Alfa Aesar) powders were mixed in a mass ratio of 18:1 in a mortar and pestle until the mixture was uniform in color. The mixture was then heated on a quartz plate to 1273 K in air for 6 hours with heating and cooling rates of 2 K/min. The resulting mixture was deep brown in color.

The LSCF and Ni-LSGM powders were measured into 0.18 g samples and pressed into pellets using a 15 mm diameter stainless steel die and a pellet press. The pellets were carefully removed from the die, placed on zirconia plates, and sintered at

1723 K in air for 4 hours with heating and cooling rates of 1 K/min. After this sintering process, catalysts were added to either side of the membranes.

1% Li-LSGM was used as the methane side catalyst in the membrane reactors. LSGM (Sigma Aldrich) was mixed with graphite (Alfa Aesar) in a mass ratio of 3:1 in a mortar and pestle. The catalyst was then suspended in ethanol and approximately 8 mg of catalyst was drop coated onto the surface of each membrane. The air side catalyst, LSCF (Sigma Aldrich), was mixed with graphite in a mass ratio of 1.75:1 in a mortar and pestle. The mixture was then suspended in ethanol and painted onto the surface of the membrane on the opposite side of the methane catalyst. The membrane reactors were then heated to 1423 K in air for 2 hours with heating and cooling rates of 2 K/min. Li_2CO_3 (Acros Organics) was dissolved in water and added to the LSGM in four additions, allowing the catalyst to dry at 348 K between additions. This process resulted in a total of 1% Li by weight in the catalyst.

The reactors were mounted onto the top of a ceramic tube with the 1% Li-LSGM catalyst facing the inside of the tube. The junction was then sealed with a paste made from glass powder (Bullseye Glass) and an aqueous solution of polyvinylpyrrolidone (PVP). As the reactors were heated the PVP burned away and the glass powder melted, creating a molten glass seal at the operating temperature.

6.3.2 Reactor Testing

The alumina tube with the reactor was then mounted inside of a vertically oriented tube furnace capable of temperatures up to 1473 K. The reactors were heated from room temperature to the operating temperature at 1.3 K/min under Ar flow. After reaching the reaction temperature, dry air was fed to the air side of the reactor at 50 sccm

and a mixture of 95% CH_4 and 5% He (Cryogenic Gases) were fed to the methane side of the reactor at 5 sccm using mass flow controllers. Effluent gases were analyzed by gas chromatography. Thermal conductivity detectors were used to monitor H_2, He, O_2, N_2, CO, and CO_2, while a flame ionization detector was used to monitor CH_4, C_2H_6, C_2H_4, and C_3 products. The detectors were calibrated using certified gas mixtures (Scotty Gases and Cryogenic Gases).

6.3.3 X-Ray Diffraction

X-ray diffraction (XRD) was used to characterize the crystal structure of the membranes and the catalysts used in this study. The XRD patterns were collected using a Rigaku MiniFlex spectrometer. This instrument uses a Cu Kα X-ray source with a graphite monochromator. Data was acquired at a tube voltage and current of 40 kV and 15 mA. XRD patterns were collected with a continuous sweep from 2Θ of 20-80 at a rate of 2 2Θ/min. Phases were identified using the assistance of Jade software.

6.3.4 Scanning Electron Microscopy

Scanning electron microscopy (SEM) was used in this study to determine the physical structure of the membrane reactors as well as perform elemental analysis on the membranes and catalysts. Electron micrographs were obtained using a Philips XL30FEG scanning electron microscope which has a resolution of a few nanometers. The elemental analysis on the samples was performed using a Si-Li solid state x-ray detector attached to the microscope which provided energy dispersive x-ray spectroscopy (EDS) data. Both the images and EDS data were collected with an accelerating voltage of 10-30 kV at a working distance of 10 mm. In all SEM experiments, the membrane reactors were fractured in order to view the cross section of the reactor.

6.4 Experimental results and discussion

6.4.1 Reactor Characterization

6.4.1.1 Membranes

Figure 6.1 shows XRD patterns for the membrane materials used in this study, along with the peaks that would be expected for NiO. In order for Ni-LSGM to have electronic and ionic conductivity, the Ni from the NiO must be incorporated into the perovskite lattice. In the data in Figure 6.1, there are nine peaks labeled with * which correspond to the perovskite structure of the LSCF and LSGM materials [16]. The diffraction pattern for the Ni-LSGM material shows the same nine peaks, and shows only a very small peak at 43.1 which corresponds to NiO. This provides evidence that the Ni has been incorporated into the perovskite lattice during the thermal treatments used to fabricate the membranes. The Ni-LSGM also shows some additional small impurity peaks which indicate that there is an impurity phase formed when Ni is incorporated into the lattice.

6.4.1.2 Reactor Structure

Figure 6.2 shows SEM micrographs of the cross section of the membrane reactors used in this study. In each membrane reactor, the top layer is a porous 1% Li-LSGM catalyst layer, with a thickness of 25-50 μm. The middle layer is the membrane layer made from either LSCF or Ni-LSGM. From the micrographs it can be determined that the membrane materials are dense and non-porous which is important because high membrane density facilitates the transfer of ions and electrons across the membrane without allowing gases from either side to pass through. Using data from the SEM micrographs of several of the membrane reactors, the thickness of the membranes was

215 +/- 3.5 µm. The bottom layer is a porous LSCF catalyst layer, with a thickness of 25-50 µm. From the micrographs, it can be determined that the catalyst layers have good contact with the membrane and neither catalyst has delaminated from the surface. Delamination can be caused by differences in the thermal expansion coefficients of the materials and results in poor contact between the layers of the membrane reactor.

6.4.1.3 Catalyst/Membrane Interfaces

In addition to determining the structure of the membrane reactors, the SEM was also used to perform EDS on the membrane/catalyst interfaces to probe the elemental composition of each layer. Using this technique, we can determine if the components of the membranes or catalysts are migrating between the layers of the membrane reactors at the fabrication or operating temperatures. Figure 6.3 shows the interfaces between a LSCF catalyst and a LSGM membrane (Figure 6.3a), a LSCF membrane and 1% Li-LSGM catalyst (Figure 6.3b), and a Ni-LSGM membrane and a 1% Li-LSGM catalyst (Figure 6.3c). In Figure 6.3a and 6.3b, the iron and cobalt (Fe and Co) signals have been mapped. In both of these samples the iron signal (blue) is constrained to the portion of the reactor containing LSCF, however, the Co signal (green) is present in both the LSCF and LSGM portions of the reactor. The movement of Co from LSCF into LSGM is well documented in solid oxide fuel cell literature [17]. There are a few consequences of the diffusion of Co from one part of the reactor to another. In the case of the LSCF catalyst and LSGM membrane (Figure 6.3a), the addition of Co to the membrane will increase the electronic conductivity of the membrane. In membranes that are meant to be electronically conductive, this will likely not cause any problems, however, this could affect the performance of reactors that are designed to operate using an external circuit.

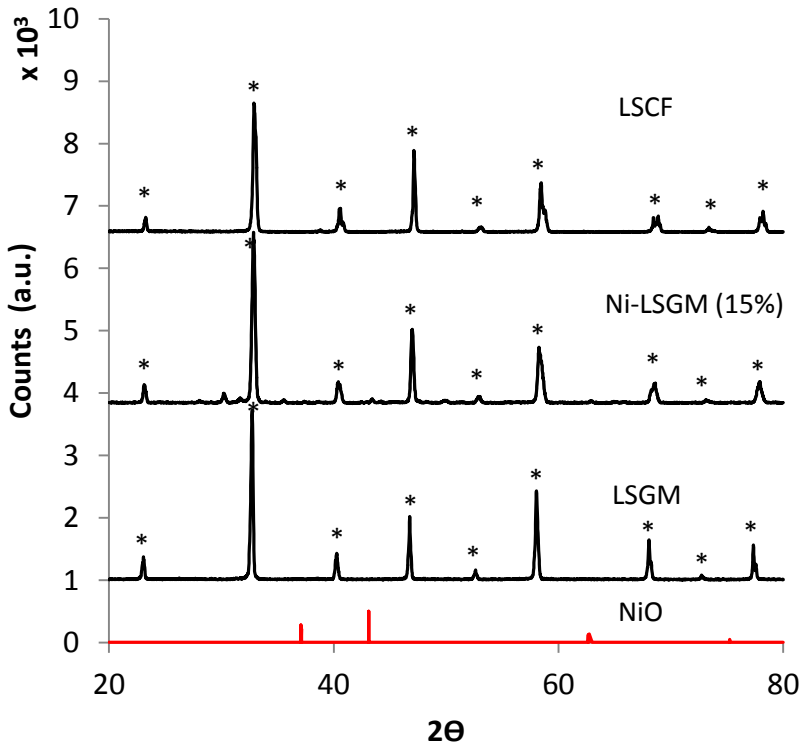

Figure 6.1: X-ray diffraction patterns for the sintered membrane disks

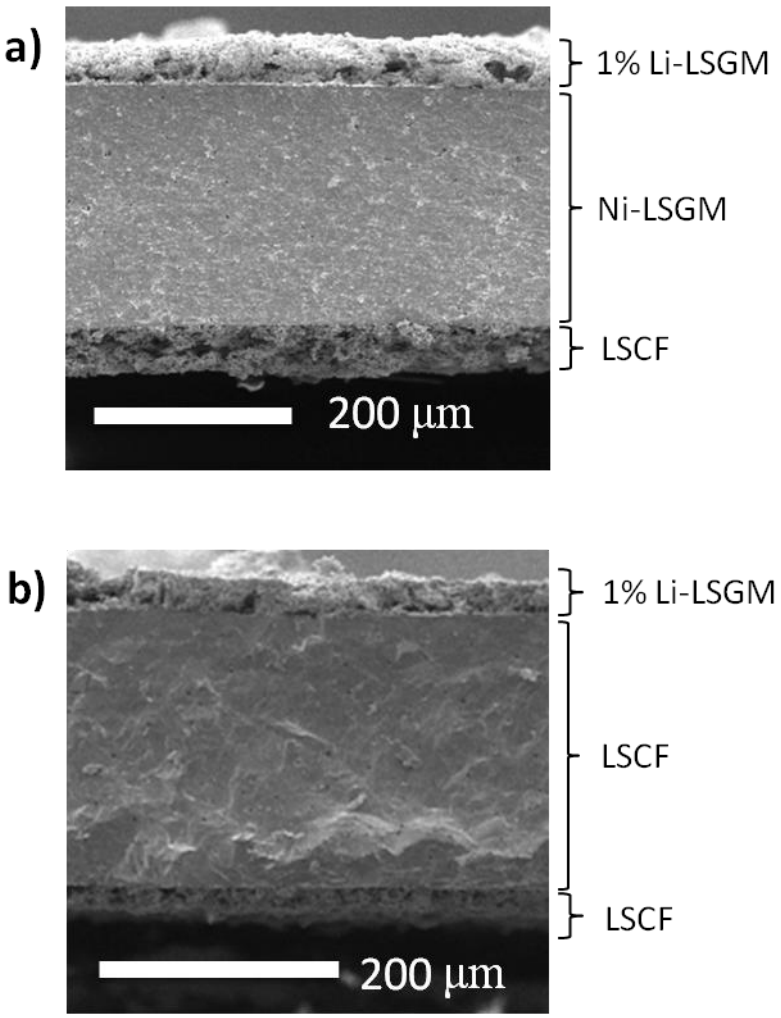

Figure 6.2: Scanning electron microscopy images for cross-sections of the membrane reactors. a) Ni-LSGM membrane reactor b) LSCF membrane reactor.

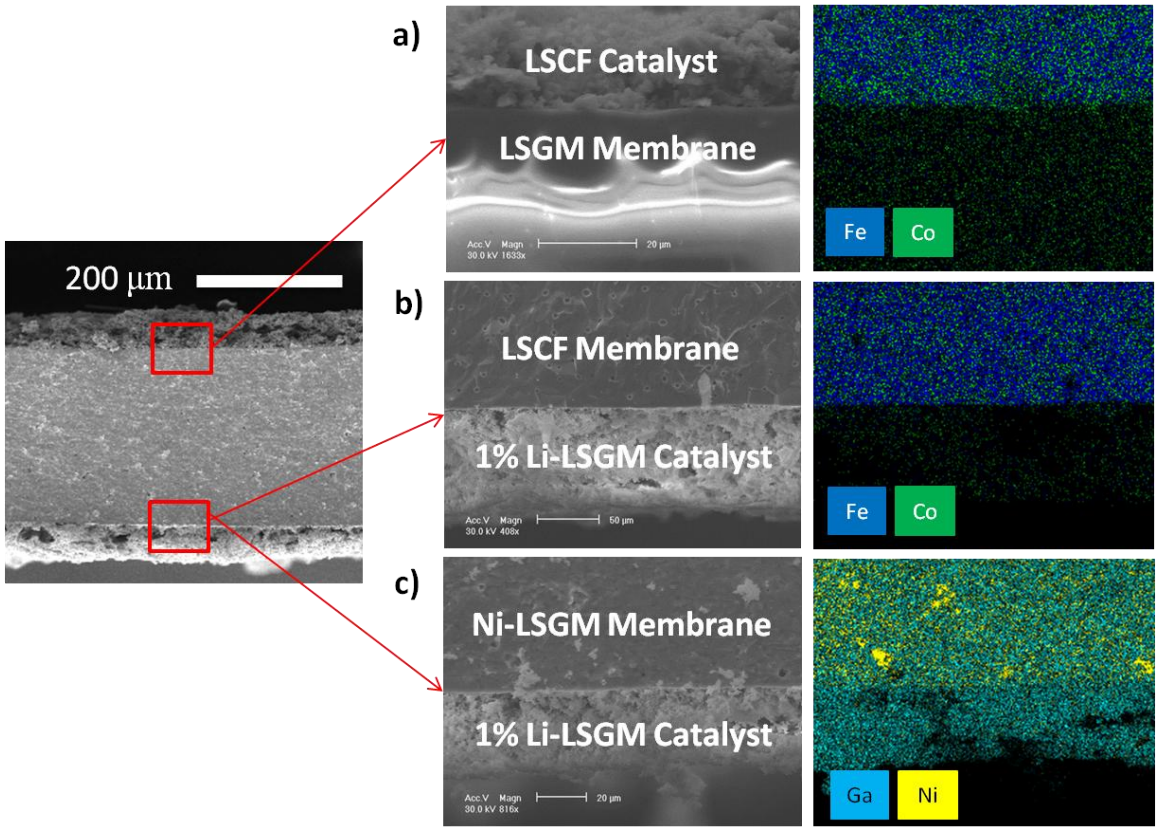

Figure 6.3: Scanning electron microscopy images and energy dispersive spectroscopy maps for membrane/catalyst interfaces. a) LSCF catalyst and LSGM membrane, b) LSCF membrane and 1% Li-LSGM catalyst and c) Ni-LSGM membrane and 1% Li-LSGM catalyst

In the opposite case of the LSCF membrane and LSGM based catalyst (Figure 6.3b), the addition of Co to the catalyst could have a detrimental effect on the selectivity of the catalyst because in previous tests of catalyst selectivity, catalysts containing transition metals (Fe, Co, Mn) showed poor selectivity to C_{2+} products [13]. In addition, the depletion of Co in the membrane may decrease the conductivity of the membrane, decreasing the flux of oxygen in the reactor. In Figure 6.3c, the gallium (Ga) and nickel (Ni) signals have been mapped. In this case, significant quantities of Ni are not detected in the catalyst. However, there are clusters of Ni within the membrane indicating that the Ni has not been completely incorporated into the lattice of the perovskite.

6.4.2 Reactor Testing

The membrane reactors were tested for oxygen flux, conversion of methane, and selectivity and yield of C_{2+} products. The methane conversion, C_{2+} selectivity and yield were calculated using the following equations:

$$X_{CH4} = \frac{CO_2 + CO + 2C_2H_6 + 2C_2H_4 + 3C_3H_8 + 3C_3H_6}{CH_4 + CO_2 + CO + 2C_2H_6 + 2C_2H_4 + 3C_3H_8 + 3C_3H_6} \quad 5.1$$

$$S_{C2+} = \frac{2C_2H_6 + 2C_2H_4 + 3C_3H_8 + 3C_3H_6}{CO_2 + CO + 2C_2H_6 + 2C_2H_4 + 3C_3H_8 + 3C_3H_6} \quad 5.2$$

$$Y_{C2+} = X_{CH4} * S_{C2+} \quad 5.3$$

The oxygen flux was calculated using an oxygen balance. Figure 6.4 shows data for the CH_4 conversion and C_{2+} yield and selectivity over time after switching the flow through the reactor from Ar to the methane mixture at 5 sccm and 1073 K for reactors with Ni-LSGM (Figure 6.4a) and LSCF (Figure 6.4b) membranes. In both reactors the data

shows that there is an initial decrease in the conversion of methane and the yield of C_{2+} products. The decrease in the conversion is rapid at first, but after a time period of about 40 hours, the conversion stabilizes at ~10% of the original value. The change in the conversion will be discussed further in Section 6.4.3.

In contrast to the conversion, there is very little change in the overall selectivity to C_{2+} products, which remains above 90% for both reactors over the entire testing period. As a comparison, 1% Li-LSGM was tested in a packed bed reactor at 1073 K with a CH_4/O_2 ratio of 145. In this packed bed reactor test, the methane conversion was 1.3% and the selectivity to C_{2+} products was 87%. Therefore, the selectivity in the membrane reactor was slightly higher than the packed bed reactor at very low conversion, indicating that the presence of transition metals in the membrane portion of the reactor is likely not detrimental to the C_{2+} selectivity of the membrane reactor.

After allowing the activity to stabilize for 40 hours, the temperature in the reactor was varied between 1023 and 1173 K to determine the effect of temperature on the methane conversion, C_{2+} yield and selectivity, and oxygen flux. The results of these tests are shown in Figure 6.5. Figure 6.5a shows the oxygen flux into the reactor, which is estimated based on a mole balance of the products and reactants. The flux of oxygen increases with the temperature, and the points lie on roughly a straight line when plotted on a log scale against 1000/T. This is typical for this type of membrane reactor and the coefficient of the flux can be modeled using the Arrhenius equation.

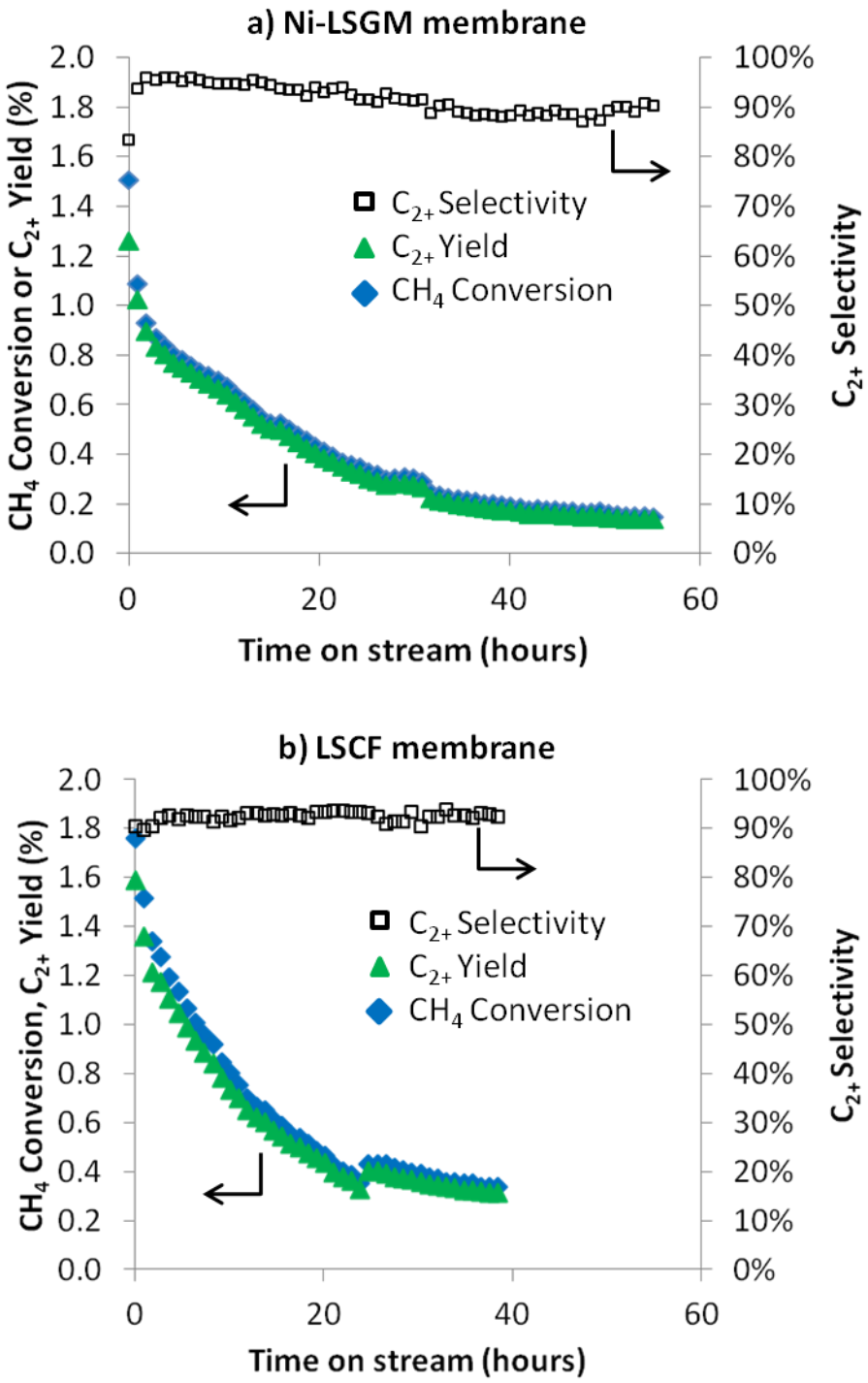

Figure 6.4: Membrane reactor methane conversion and C_{2+} yield and selectivity over time for a) Ni-LSGM membrane reactor, b) LSCF membrane reactor

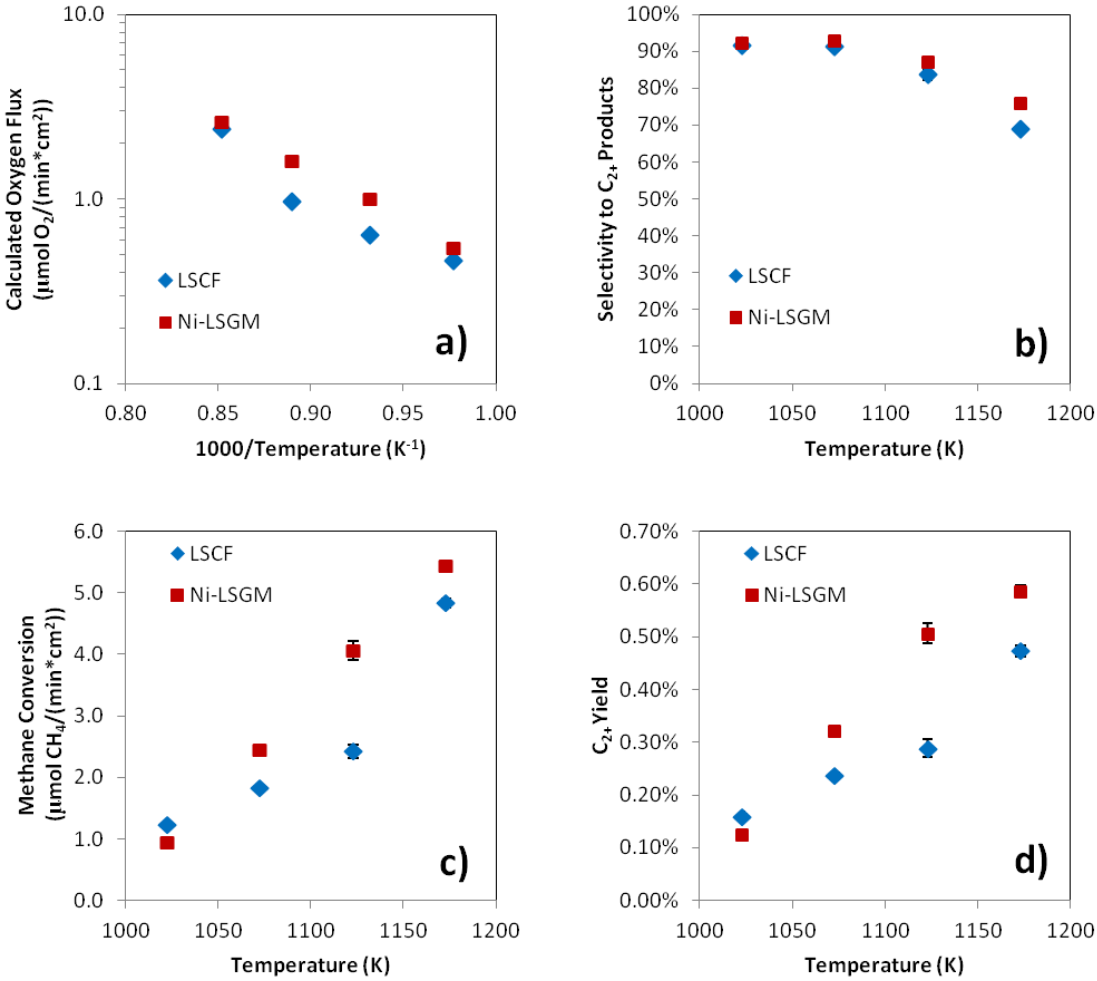

Figure 6.5: Steady state reactor results for LSCF and Ni-LSGM membrane reactors: a) oxygen flux, b) selectivity to C_{2+} products, c) methane conversion, d) C_{2+} yield

Figure 6.5b shows the C_{2+} selectivity data as a function of the temperature. The selectivity at 1023 K is high at above 90%, and as the temperature increases, the selectivity remains high until 1123 K when it begins to decrease. This decrease may be due to unselective gas phase reactions which become increasingly significant as the temperature increases. Figure 6.5c and Figure 6.5d show methane conversion and C_{2+} yield data as a function of the reactor temperature. The conversion and yield increase as the temperature in the reactor is increased, and because the C_{2+} selectivity remains relatively high, the methane conversion and C_{2+} yield follow very similar trends with temperature.

Figure 6.6 shows the selectivity to each carbon product at steady state as a function of the reactor temperature for both membrane reactors tested. At the lowest temperature tested (1023 K), ethane made up the largest fraction of the products. As the temperature increased, selectivity to ethane decreased, and selectivity to ethylene increased up to a temperature of 1123 K. Above 1123 K, the total selectivity to C_2 products decreased. Selectivity to CO, CO_2, and C_3 products increased with temperature over the entire range tested. These results are consistent with the results from the packed bed reactor tests, where ethane is the first product formed, and ethylene and C_3 products are formed through subsequent reactions as conversion increases.

6.4.3 Activity Degradation

Although the reactor conversion reaches a steady state, it is important to understand the mechanism responsible for the initial decline in the conversion because if it could be prevented, the yield of C_{2+} products would increase by approximately an order of magnitude. In this type of membrane reactor, the most likely factors limiting the

conversion are either the activation of methane by the catalyst or the flux of oxygen through membrane. At the reaction conditions used in this study, it is very likely that carbon deposition is responsible for the decline in the conversion over time. At temperatures of 1073 K with high concentrations of methane and low concentrations of oxygen, solid carbon is thermodynamically favorable [18]. XRD was used to test for carbon in the used catalyst. Figure 6.7 shows XRD patterns for catalysts supported on membrane disks. Figure 6.7a shows the diffraction pattern for a 1% Li-LSGM catalyst that was heated under Ar to 1073 K and held for 2 hours before cooling back down to room temperature. The diffraction pattern for this catalyst is very similar to the 1% Li-LSGM catalyst heated in Ar in the packed bed reactor study [13]. Figure 6.7b shows the diffraction pattern for the used catalyst which was held at the reaction conditions for more than 40 hours and then cooled in methane. This diffraction pattern shows the characteristic perovskite peaks with the addition of a sharp peak corresponding to graphitic carbon at 2θ of 26.4. This result shows that although the catalyst retains its perovskite structure under the operating conditions, there is also carbon present in the catalyst. The presence of carbon could explain the decline in conversion over time because carbon can bind to the surface of the catalyst, blocking active sites.

More testing is necessary to determine if carbon deposition is the only factor in the decline of the catalyst activity, but it is certainly a problem that needs to be addressed. To inhibit carbon in this type of reactor it may be useful to add water to the methane feed, which is a common practice to decrease carbon deposition in solid oxide fuel cells [18]. However, it is likely that the best way to decrease carbon deposition is to increase the oxygen flux across the membrane using techniques described in Chapter 4.

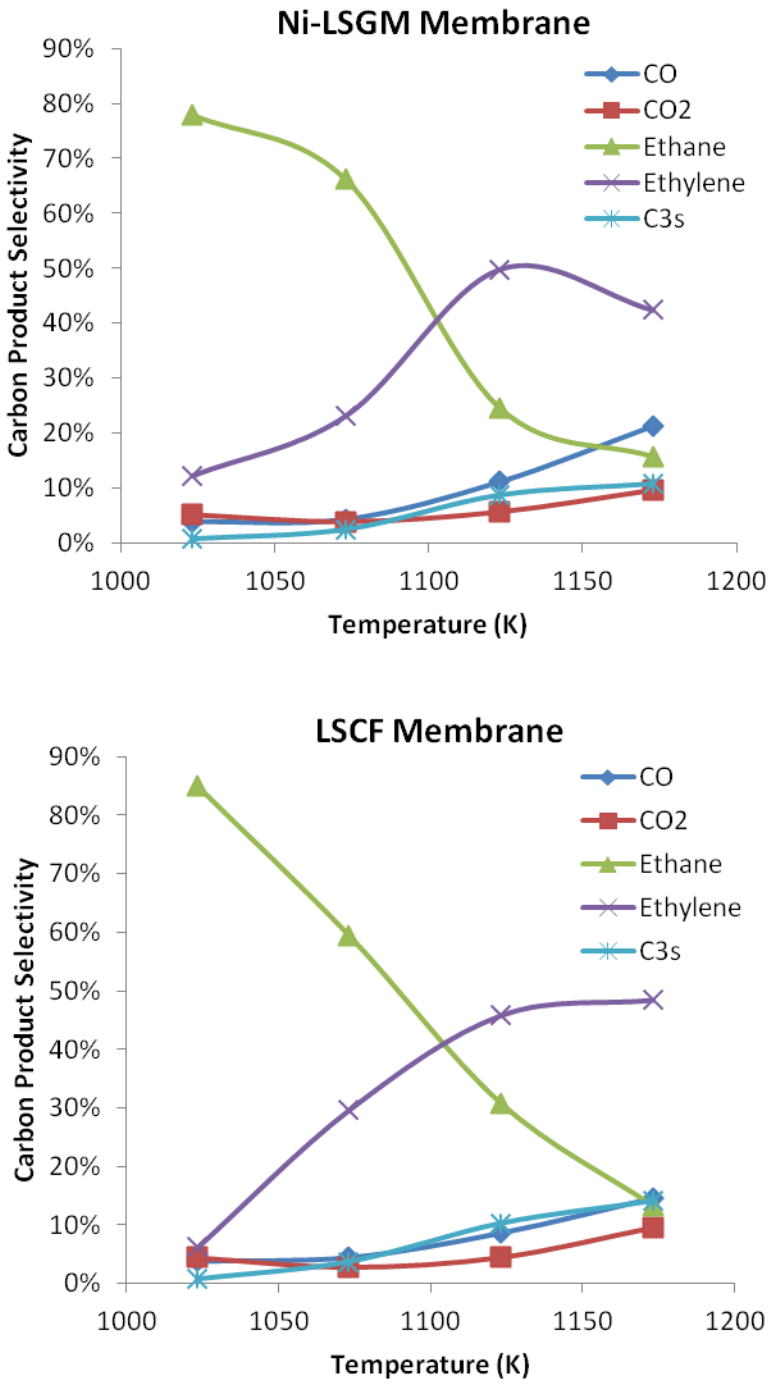

Figure 6.6: Selectivity of carbon products formed at steady state reaction conditions a) Ni-LSGM membrane reactor, b) LSCF membrane reactor

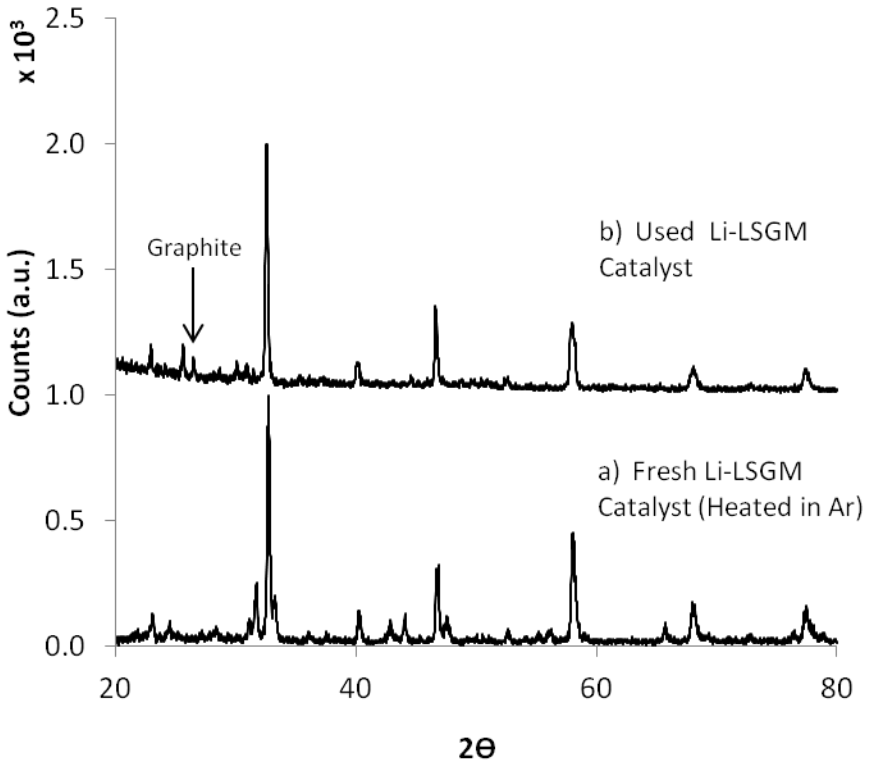

Figure 6.7: X-ray diffraction of catalysts supported on membrane disks. a) 1% Li-LSGM catalyst heated in Ar, b) 1% Li-LSGM catalyst after reaction

6.5 Conclusions

In this work, 1% Li-LSGM was tested as a catalyst material for the oxidative coupling of methane in membrane reactors. Small disk shaped membrane supported reactors were successfully fabricated from LSCF and Ni-LSGM, with porous air and methane side catalysts on either side. In both types of membrane reactor, the selectivity to C_{2+} products was above 90% at 1073 K despite the presence of transition metals in the membranes. The highest methane conversion achieved in the reactors at 1073 K was 1.8% with a C_{2+} yield of 1.6%, however the conversion declined over time. The decline in conversion was likely due to carbon deposition on the surface of the methane catalyst, and the presence of carbon was confirmed by XRD.

6.6 References

[1] W. Hinsen, M. Baerns, Oxidative coupling of methane to C_2 hydrocarbons in the presence of different catalysts, Chem. Zeitung. 107 (1983) 223–226.

[2] G. Keller, M.M. Bhasin, Synthesis of ethylene via oxidative coupling of methane I. Determination of active catalysts, J. Catal. 73 (1982) 9–19. doi:10.1016/0021-9517(82)90075-6.

[3] D. Eng, M. Stoukides, Catalytic and Electrocatalytic Methane Oxidation with Solid Oxide Membranes, Catal. Rev. 33 (1991) 375–412. doi:10.1080/01614949108020304.

[4] X. Tan, K. Li, Oxidative coupling of methane in a Perovskite Hollow-Fiber Membrane Reactor, Ind. Eng. Chem. Res. 45 (2006) 142–149. doi:10.1016/0926-860X(95)00098-4.

[5] F.T. Akin, J.Y.S. Lin, Oxygen permeation through oxygen ionic or mixed-conducting ceramic membranes with chemical reactions, J. Memb. Sci. 231 (2004) 133–146. doi:10.1016/j.memsci.2003.11.012.

[6] Y. Lu, A.G. Dixon, W.R. Moser, Y.H. Ma, U. Balachandran, Oxygen-permeable dense membrane reactor for the oxidative coupling of methane, J. Memb. Sci. 170 (2000) 27–34. doi:10.1016/S0376-7388(99)00354-3.

[7] X. Tan, Z. Pang, Z. Gu, S. Liu, Catalytic perovskite hollow fibre membrane reactors for methane oxidative coupling, J. Memb. Sci. 302 (2007) 109–114. doi:10.1016/j.memsci.2007.06.033.

[8] N.H. Othman, Z. Wu, K. Li, An oxygen permeable membrane microreactor with an in-situ deposited $Bi_{1.5}Y_{0.3}Sm_{0.2}O_{3-\delta}$ catalyst for oxidative coupling of methane, J. Memb. Sci. 488 (2015) 182–193. doi:10.1016/j.memsci.2015.04.027.

[9] Y. Lu, A.G. Dixon, W.R. Moser, Y.H. Ma, Oxidative coupling of methane in a modified gamma-alumina membrane reactor, Chem. Eng. Sci. 55 (2000) 4901–4912.

[10] O. Czuprat, T. Schiestel, H. Voss, J. Caro, Oxidative Coupling of Methane in a BCFZ Perovskite Hollow Fiber Membrane Reactor, Ind. Eng. Chem. Res. 49 (2010) 10230–10236. doi:10.1021/ie100282g.

[11] L. Olivier, S. Haag, C. Mirodatos, A.C. van Veen, Oxidative coupling of methane using catalyst modified dense perovskite membrane reactors, Catal. Today. 142 (2009) 34–41. doi:10.1016/j.cattod.2009.01.009.

[12] F.T. Akin, Y.S. Lin, Oxidative coupling of methane in dense ceramic membrane reactor with high yields, AIChE J. 48 (2002) 2298–2306. doi:10.1002/aic.690481019.

[13] B. Farrell, S. Linic, Oxidative coupling of methane over mixed oxide catalysts designed for solid oxide membrane reactors, Submitted. (n.d.).

[14] S.P.S. Badwal, S. Giddey, C. Munnings, a. Kulkarni, Review of progress in high temperature solid oxide fuel cells, J. Aust. Ceram. Soc. 50 (2014) 23–37.

[15] T. Ishihara, T. Yamada, H. Arikawa, H. Nishiguchi, Y. Takita, Mixed electronic – oxide ionic conductivity and oxygen permeating property of Fe- , Co- or Ni-doped $LaGaO_3$ perovskite oxide, Solid State Ionics. 135 (2000) 631–636. doi:10.1246/cl.1999.1257.

[16] E. Djurado, M. Labeau, Second phases in doped lanthanum gallate perovskites, J. Eur. Ceram. Soc. 18 (1998) 1397–1404. doi:10.1016/S0955-2219(98)00016-8.

[17] Z. Bi, Y. Dong, M. Cheng, B. Yi, Behavior of lanthanum-doped ceria and Sr-, Mg-doped $LaGaO_3$ electrolytes in an anode-supported solid oxide fuel cell with a $La_{0.6}Sr_{0.4}CoO_3$ cathode, J. Power Sources. 161 (2006) 34–39. doi:10.1016/j.jpowsour.2006.03.065.

[18] K. Sasaki, Y. Teraoka, Equilibria in Fuel Cell Gases I, J. Electrochem. Soc. 150 (2003) A878–A884. doi:10.1149/1.1577338.

Chapter 7

Conclusions and future outlook

7.1 Conclusions

7.1.1 Solid oxide fuel cells [1]

The solid oxide fuel cell portion of this study demonstrated that carbon deposition catalyzed on monometallic Ni in the process of electrochemical oxidation of ethanol can be decreased by alloying the Ni catalyst with small amounts of Sn. In SOFCs fabricated using monometallic Ni, carbon deposition resulted in physical and electrochemical changes to the Ni anode. In contrast, Sn/Ni alloy anodes inhibited the formation of carbon-induced degradation catalyzed by Ni, resulting in smaller electrochemical changes over time and less carbon deposition. Additionally, we showed that the C/O ratio on the surface of the anode electrocatalyst affects the carbon deposition, with less carbon detected near the electrolyte and at lower operating voltages where the C/O ratio is lower. Overall the results of this study indicate that the catalyst surface chemistry and local C/O ratios are both important factors that must be considered in the design of fuel cell anode catalysts operating on oxygenated hydrocarbon fuels.

7.1.2 Oxidative coupling of methane

The analysis from the membrane and packed bed reactor models showed that the use of membrane reactors for OCM can theoretically result in higher yields of ethane and ethylene products compared to packed bed reactors. The optimal design of a membrane

OCM reactor system would include a catalyst that is integrated with the membrane and is active and selective under the relevant operating conditions. Therefore, we identified and tested several catalysts for OCM activity and selectivity which could be integrated into a solid oxide membrane reactor, and found that lanthanum gallate doped with strontium and magnesium ($La_{0.8}Sr_{0.2}Ga_{0.8}Mg_{0.2}O_{3-x}$, LSGM) was a promising candidate [2]. The results of the packed bed and membrane reactor studies at 1073 K included in this dissertation are shown in Figure 7.1 (in red) along with published data from many other studies (in black). Figure 7 shows that when used in a packed bed reactor, the Li doped LSGM used in this study has high selectivity to C_2 products at low conversions of methane, with decreasing C_2 selectivity as conversion increases. Figure 7.1 also shows that when Li-LSGM is used in a membrane reactor, the selectivity to C_2 products is higher than when used in a packed bed reactor at similar methane conversion, indicating that there is an increase in selectivity due to the membrane reactor design. Overall, when integrated into a membrane reactor, this catalyst showed high selectivity to ethane and ethylene, however, due to low membrane surface area the methane conversion was very small and decreased over time which was likely due to carbon poisoning of the catalyst surface.

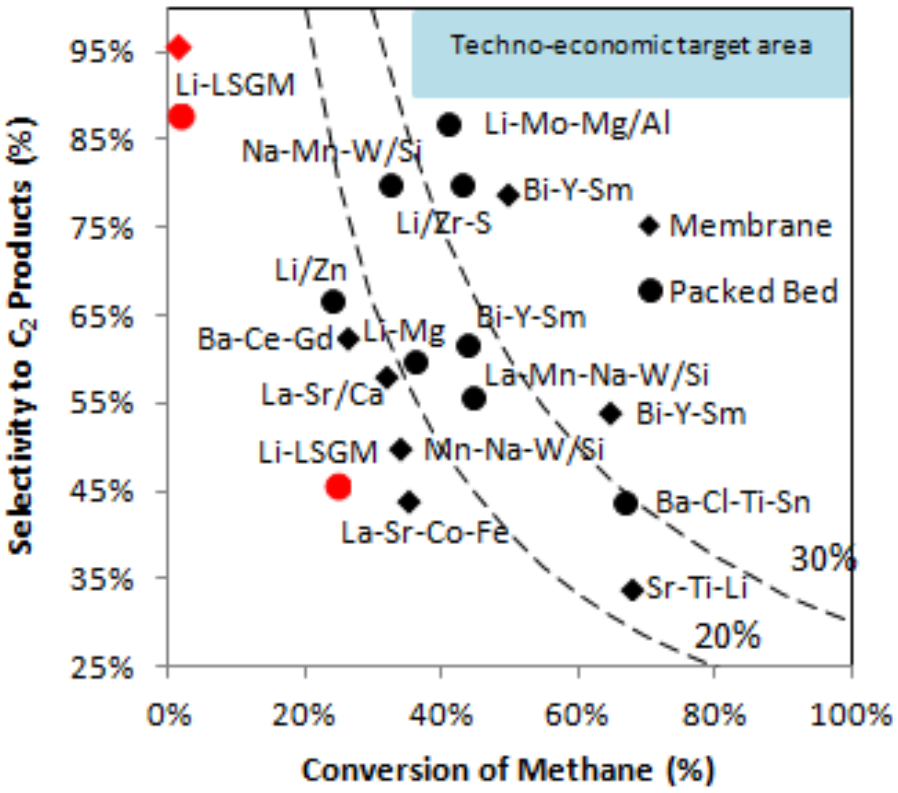

Figure 7.1: C_2 selectivity and methane conversion diagram for results presented in this dissertation (red data points) as well as from several other publications (black data points) References for data points in black are included in Chapter 4.

7.2 Future directions

7.2.1 Solid oxide fuel cells

To further understand the effects of oxygenated fuels on Ni and Sn/Ni alloy electrocatalysts, testing should be done at a wider range of temperatures and fuel compositions. In this study, Ni and Sn/Ni anode electrocatalysts were compared at a few representative conditions to show the effect of the addition of Sn. An extension of this work would be to test Sn/Ni alloy electrocatalyts at a wider range of temperatures and fuel concentrations to better understand the conditions and C/O ratios where carbon deposition is inhibited by this type of catalyst.

Another extension of this work would be to test Sn/Ni alloy electrocatalysts with butanol as a fuel. Like ethanol, butanol can be produced from biomass via fermentation and provides reductions in greenhouse gas emissions compared to petroleum gasoline [3]. Butanol is an interesting oxygenated fuel because although it is produced in significantly smaller quantities than ethanol, production is projected to grow because it offers benefits over ethanol. These benefits include 1) energy density comparable to gasoline (can be blended with gasoline at higher fractions than ethanol), 2) low miscibility with water, and 3) ability use current gasoline infrastructure [4].

7.2.2 Oxidative coupling of methane

In this study we have only just begun to understand how oxidative coupling of methane might be incorporated into solid oxide membrane reactors and there are many future directions that could be pursued. First, a larger number of catalysts should be tested for OCM activity and selectivity. In this dissertation, the materials tested were limited to those commonly used in solid oxide fuel cells. Although this was a good place

to start, there are many other materials that are used as solid oxide membranes and may be interesting as OCM catalysts. A large number of solid oxide membrane materials has been compiled by Sunarso et al. in a review [5]. Two of these materials that are particularly interesting are $Bi_{1.5}Y_{0.3}Sm_{0.2}O_{3-\delta}$ (BYS) [6,7] and $BaCe_{0.8}Gd_{0.2}O_3$ (BCG) [8] which have ionic and electronic conductivity and have shown high selectivity to ethane and ethylene in previous tests.

Once catalysts are identified, they should be tested using high methane and ethylene concentrations to determine their carbon tolerance. This is important because catalyst activity can quickly degrade under the very low oxygen operating conditions of a membrane reactor. To inhibit carbon in this type of reactor it may be useful to add water to the methane feed. This technique is commonly used to decrease carbon deposition in solid oxide fuel cells [9]. However, it is likely that the best way to decrease carbon deposition is to increase the oxygen flux into the reactor.

In addition to decreasing carbon formation on the catalyst surface, increasing the oxygen flux into the reactor would have several benefits for solid oxide membrane reactors. Using the current state of the art membrane materials and fabrication techniques, oxygen flux through the membrane is still relatively slow. This results in membrane reactors that either have low conversion, have large membrane surface areas (and large volumes), or use low flow rates of methane. Increasing the rate of oxygen flux through the membrane should be possible using similar techniques that are used for solid oxide fuel cells. One technique commonly used in solid oxide fuel cells is to support the membrane on a porous structure because supported solid oxide membranes can be much thinner. Membrane thicknesses of 10-50 μm can be relatively easily fabricated, and it has

been found that thinner membranes decrease the resistance across the membrane, increasing oxygen flux [10].

Another strategy to increase the oxygen flux in solid oxide membrane reactors is to use a membrane that does not have electronic conductivity, and control the flux electrochemically. Although there have been studies which employed this technique for OCM, there have been many advances in solid oxide membrane reactor technology since their publication [11]. One advantage to this type of system is that membrane materials could be used that have higher ionic conductivity than mixed ionic and electronically conductive materials, such as lanthanum gallate doped with strontium and magnesium ($La_{0.8}Sr_{0.2}Ga_{0.8}Mg_{0.2}O_{3-\delta}$ or LSGM) [12] or lanthanum germanates (such as $La_{9.33}Ge_6O_{26}$) [13]. Use of these materials could lead to increased flux of O^{2-} across the membrane. Additionally, the external circuit in these systems can be used to change the potential difference across the membrane and therefore control the O^{2-} flux. The circuit can also be used to add additional electrons to the system, using the system as an oxygen pump to increase the flux electrochemically [11].

Overall, there are many opportunities for the improvement of solid oxide membrane reactors for OCM. However, in order to advance this technology it will be necessary to understand both the catalytic requirements of OCM and the materials challenges presented by solid oxide membrane reactors. Over the last few decades, materials and fabrication advances have been made in solid oxide membrane reactors for use in solid oxide fuel cells and oxygen separation technologies. Incorporating these advances into membrane reactors designed for OCM will be necessary to increase the flux of oxygen across the membrane and increase the yield of C_2 products.

7.3 References

[1] B. Farrell, S. Linic, Direct electrochemical oxidation of ethanol on SOFCs: improved carbon tolerance of Ni anode by alloying, Submitted. (2015).

[2] B. Farrell, S. Linic, Oxidative coupling of methane over mixed oxide catalysts designed for solid oxide membrane reactors, Submitted. (2015).

[3] M. Wu, M. Wang, J. Liu, H. Huo, REVIEW : BIOSEPARATIONS AND Assessment of Potential Life-Cycle Energy and Greenhouse Gas Emission Effects, Biotechnol. Prog. (2008) 1204–1214. doi:10.1021/bp.71.

[4] H. Wu, M., Wang, M., Liu, J., Huo, Life-Cycle Assessment of Corn-Based Butanol as a Potential Transportation Fuel, 2007.

[5] J. Sunarso, S. Baumann, J.M. Serra, W. A. Meulenberg, S. Liu, Y.S. Lin, et al., Mixed ionic-electronic conducting (MIEC) ceramic-based membranes for oxygen separation, J. Memb. Sci. 320 (2008) 13–41. doi:10.1016/j.memsci.2008.03.074.

[6] F.T. Akin, J.Y.S. Lin, Oxygen permeation through oxygen ionic or mixed-conducting ceramic membranes with chemical reactions, J. Memb. Sci. 231 (2004) 133–146. doi:10.1016/j.memsci.2003.11.012.

[7] N.H. Othman, Z. Wu, K. Li, An oxygen permeable membrane microreactor with an in-situ deposited $Bi_{1.5}Y_{0.3}Sm_{0.2}O_{3-\delta}$ catalyst for oxidative coupling of methane, J. Memb. Sci. 488 (2015) 182–193. doi:10.1016/j.memsci.2015.04.027.

[8] Y. Lu, A.G. Dixon, W.R. Moser, Y.H. Ma, U. Balachandran, Oxygen-permeable dense membrane reactor for the oxidative coupling of methane, J. Memb. Sci. 170 (2000) 27–34. doi:10.1016/S0376-7388(99)00354-3.

[9] K. Sasaki, Y. Teraoka, Equilibria in Fuel Cell Gases I, J. Electrochem. Soc. 150 (2003) A878–A884. doi:10.1149/1.1577338.

[10] R.M. Ormerod, Solid oxide fuel cells, Chem. Soc. Rev. 32 (2003) 17–28. doi:10.1039/b105764m.

[11] D. Eng, M. Stoukides, Catalytic and Electrocatalytic Methane Oxidation with Solid Oxide Membranes, Catal. Rev. 33 (1991) 375–412. doi:10.1080/01614949108020304.

[12] T. Ishihara, Novel electrolytes operating at 400-600 C, in: Handb. Fuel Cells Fundam. Technol. Appl. Part 2, 2003: pp. 1109–1122.

[13] G. Yin, H. Yin, M. Sun, L. Zhong, J. Zhang, R. Cong, et al., New approach to improve the conductivity of apatite-type lanthanum germanate $La_{9.33}Ge_6O_{26}$ as electrolyte for IT-SOFCs, RSC Adv. 4 (2014) 15968. doi:10.1039/C4RA00713A.